Development of Silicon-rich poly-Silicon Carbide passivating contacts for solar cells

In partial fulfillment of the requirements for the degree of

Master of Science

Sustainable Energy Technology

Antonios Mandrampazakis

June 2019

PVMD group, Sustainable Energy Technology, EEMCS Faculty,
Delft University of Technology

Graduate
Mandrampazakis Antonios
MSc Sustainable Energy Technology
Faculty of Electrical Engineering,Mathematics and Computer Science (EEMCS)
antonismdr@gmail.com

Supervisors
Assoc. Prof. Dr. Olindo Isabella
Dr. Luana Mazzarella

Msc Thesis Committee
Assoc. Prof. Dr. Olindo Isabella, TU Delft (ESE-PVMD)
Prof. Dr. Miro Zeman, TU Delft (ESE-PVMD)
Dr. Henk van Zeijl, TU Delft (ECTM)
Dr. Luana Mazzarella, TU Delft (ESE-PVMD)

Delft University of Technology
Department of Electrical Sustainable Energy
Photovoltaic Materials and Devices

Contents

Abstract

Carrier-selective passivating contacts (CSPC) are one of the most promising silicon solar cell contact structures. These contacts enable the passivation of the silicon surface as well as a high carrier selectivity. So far excellent results have been demonstrated with the use of poly-Si in stack with SiO_2. In this work, we optimize an alternative stack, based on carbon alloyed poly-Si (poly-SiC_x). Alloying with carbon provides wet-chemical stability, the material becomes resilient to blistering and the bandgap can be tuned depending on the carbon content. This optimized poly-SiC_x is implemented as the rear contact of a solar cell.

We investigate doped poly-Si alloyed layers with different carbon contents. Structure characterization reveals that carbon incorporation hinders the crystallization of the material. In addition, alloying with carbon decreases the absorption coefficient of the material in the as-deposited state (amorphous), but following the thermal treatment higher carbon contents lead to a higher absorption coefficient. Finally, we observe that higher carbon alloying reduces the conductivity of the poly-SiC_x by several orders of magnitude, but the optimized material demonstrates a dark conductivity of 0.006 S/cm, which is 3 orders of magnitude higher than the amorphous one.

We optimize the passivation quality of (p)poly-SiC_x in symmetrical samples by inserting an (i)a-Si interlayer between the SiO_2 and the doped layer using different deposition methods (PECVD/LPCVD). With the optimization of the gas flow ratio, high-temperature annealing and hydrogenation, we obtain a high passivation quality (iV_{oc} of 709 mV and J_o of 10.5 fA/cm^2) for the optimum LPCVD deposited interlayer, while the optimum PECVD deposited interlayer demonstrates a significantly lower passivation quality (iV_{oc} of 684 mV and J_o of 34.7 fA/cm^2). The hydrogenation is performed with the deposition of a SiN_x capping layer followed by Forming Gas Annealing at 400°C for 30 minutes.

The potential of the (p)poly-SiC_x passivating contact is investigated by the application on the rear side of a solar cell. We fabricate initially double-side polished cells with the champion cell achieving an active area efficiency (η_{act}) of 15.68%, featuring a V_{oc} of 692 mV, FF of 74.7% and EQE current ($J_{sc,EQE}$) of 30.35 mA/cm^2. Finally, we also investigate the potential on front side textured cells, obtaining the champion cell with an η_{act} of 16.80%, maintaining the FF at 74.7%, a lower V_{oc} of 677 mV and a $J_{sc,EQE}$ at 33.22 mA/cm^2. For all cells the parasitic absorption at the front (n)poly-SiC_x contact remains high, due to the non-optimized thickness of the aforementioned contact.

Nomenclature

τ_{eff}	Effective Lifetime
ALD	Atomic Layer Deposition
CSPC	Carrier-Selective Passivating Contact
DSP	Double Side Polished
$\mathbf{E_c}$	Conduction Band
$\mathbf{E_v}$	Valence Band
EQE	External Quantum Efficiency
FBC	Front and Back Contacted
FF	Fill Factor
FGA	Forming Gas Annealing
FST	Front Side Textured
FTIR	Fourrier-Transform Infrared Spectroscopy
FZ	Float Zone
$\mathbf{HNO_3}$	Nitric Acid
ITO	Indium-Tin Oxide
$\mathbf{iV_{oc}}$	Implied Open-Circuit Voltage
$\mathbf{J_o}$	Saturation Current density
$\mathbf{J_{sc}}$	Short-Circuit Current density
LPCVD	Low Pressure Chemical Vapor Deposition
NAOS	Nitric Acid Oxidation of Silicon
PECVD	Plasma Enchanced Chemical Vapor Deposition
poly-SiC$_x$	Polycrystalline Silicon-Carbide

poly-Si	Polycrystalline Silicon
SiO_x	Silicon Oxide
SP	Screen-printing
TCO	Transparent Conductive Oxide
TOPCon	Tunnel Oxide Passivating Contact
V_{oc}	Open-Circuit Voltage

Chapter 1

Fundamentals

In this chapter an introduction alongside the basic theoretical background is provided in order to have a better understanding of the work done during this thesis. Firstly, an introduction on the solar energy fundamentals is given followed by the basic working principle of a solar cell and the main recombination mehcanisms occurring. Thereafter, the most promising carrier-selective passivating contacts are introduced with an extended focus on poly-silicon based passivating contacts, which are also treated in this work. Finally, the motivation behind using poly-silicon carbide is given alongside the research questions of this thesis work.

One of the major challenges humanity is facing nowadays is the growing demand for energy. Although the worldwide energy consumption is estimated at approximately 16 TW-yr annually, it is expected to follow an upward trend in the coming years [1]. This expected growth in the worldwide energy consumption is going to originate from both the increase in the global population as well as the industrialization of the developing countries. It is estimated that 1.2 billion people do not have access to electricity, while 3 billion cook and heat their homes by burning wood or coal and in the forthcoming years all of this population will require access to a reliable electricity network, leading to an increased energy demand [2].

Up until now the majority of humanity's energy needs were covered through fossil fuels. By burning carbon based fossil fuels the chemical energy stored within is released as heat in order to drive the traditional combustion engines. This behaviour has been linked to a soaring concentration of greenhouse gasses in Earth's atmosphere. It is estimated that in 2015 there were over 33 Gt of CO_2 emissions [3]. Humanity's excess burning of those carbon based fossil fuels has led to serious environmental concerns, such as the greenhouse effect. As a consequence of the devastating environmental effects on the planet, the COP21 Paris Agreement, which is a global agreement between 196 nations, was signed in order to reduce the amounts of carbon dioxide released into the atmosphere [4]. Even though such an agreement has been signed between so many nations how will the continuously growing demand for energy be actually met?

The combination of various renewable energy sources such as solar, wind, hydropower,

biomass and geothermal are already being incorporated in the traditional energy system in order to provide energy in a green way. Renewable energy sources will have the fastest growth in the electricity sector in the coming years and are expected to provide 30% of the power demand in 2023 while providing 12.4% of the global energy demand in the same year [5].

1.1 Solar Energy

Solar energy could contribute into providing the answer to the globally increasing demand of energy in an environmental friendly way, since it is the most abundant renewable energy source. As depicted in Figure 1.1 the solar potential is 23.000 TW-yr, and even though this does not take into account conversion efficiency, but it is rather the incident power from the sun to Earth's surface, it can be easily understood that it is orders of magnitude greater than the potential of any other energy source or the world energy consumption of 16 TW-yr [6]. Due to its enormous potential solar energy could become the next main source of energy, if incorporated in a complete energy system with storage capabilities.

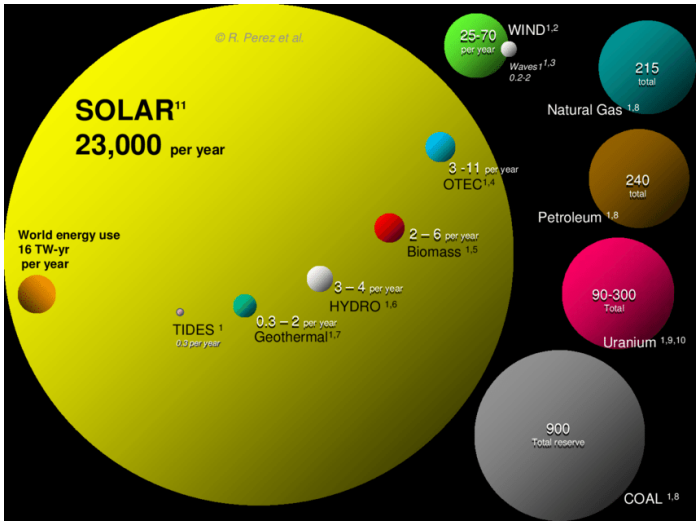

Figure 1.1: Comparing finite and renewable planetary energy reserves (Terawattyears) [6].

All objects with a temperature above the absolute zero emit electromagnetic radiation. Sun being an object with a high temperature (5778 K) emits solar radiation, which can be described both as a wave or a particle, namely the photon [7]-[8]. The photons can be described by energy while the waves can be described by their wavelength and frequency. The equation which describes this relationship is the following:

$$\nu = \frac{c}{\lambda} \tag{1.1}$$

Where ν is the frequency in Hz, c is the speed of light in vacuum (299.792.458 $\frac{m}{s}$) and λ is the wavelength.

Furthermore, the energy of a photon is inversely proportional to its wavelength as shown in Equation 1.2.

$$E = h\nu = \frac{hc}{\lambda} \tag{1.2}$$

Where h is Planck's constant.

Almost all the energy of the solar radiation is emitted in the wavelengths between 150 nm and 4000 nm. In more details, approximately 40% of the solar radiation originates from the visible spectrum (400-700 nm), approximately 51% from the infrared region (700-4000 nm) and the remaining in the ultraviolet region (150- 400 nm) [9]. The spectral irradiance is a function of a photon's energy or wavelength and it describes the power density of the particular photon. The spectral irradiance can be described through Equation 1.3.

$$I = \Phi(\lambda) \cdot \frac{hc}{\lambda} \tag{1.3}$$

Where $\Phi(\lambda)$ is the photon flux and is defined as the photon flow per area.

In Figure 1.2 the spectral irradiance is depicted for various conditions. Air Mass (AM) determines how far through the Earth's atmosphere light has travelled. Thus, AM0 represents the irradiance just outside Earth's atmosphere. On the other hand, AM1.5 represents the irradiance when the angle between Sun's postion and the zenith is 48.2 °. By integrating the irradiance over the entire solar spectrum it can be found that the total radiation is 1353 W/m^2.

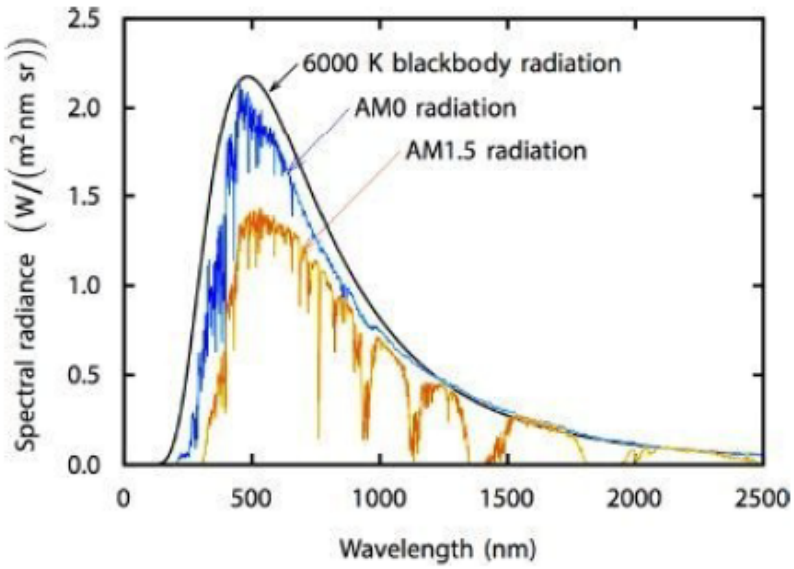

Figure 1.2: Different solar spectra [10].

1.2 PV Technology

As already mentioned previously renewable energy sources are on the rise gaining a bigger share of the energy production each year. In more details the growth of photovoltaics (PV) has followed an exponential trend in the last 25 years. The cumulative installed solar PV capacity in 2017 was near 398 GW, generating over 460 TWh [11], corresponding to approximately 2% of the global output. In Figure 1.3 the installed PV capacity in 2017 is shown alongside the projections for the coming years till 2023, which shows the great interest in this energy generating technology.

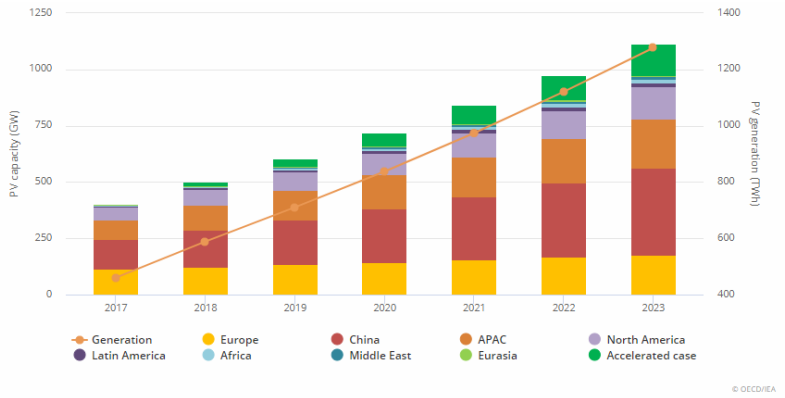

Figure 1.3: Solar PV cumulative capacity and generation, 2017-2023 [11].

Solar PV can be categorized in three main generations depending on the materials used in the fabrication process. The first generation of solar PV consists of a wafer based on crystalline silicon (c-Si) and this technology is dominating the market with a share of around 95% in production [12]. The theoretical efficiency limit for such solar cells is the Shockley-Queisser limit [13], which was recently reassessed at 29.4% for a material with a bandgap of 1.1 eV and taking into consideration Auger recombination [14]. These first generation of solar cells consist of high purity c-Si cells and a single PN-junction. Such solar cells are able to perform exceptionally, reaching a record efficiency of up to 26.7% for an n-type interdigitated back contact solar cell by Kaneka [15].

The second generation of solar cells consists of the thin-film solar cells. As the name indicates such solar cells are made very thin, by using as the main material hydrogenated amorphous silicon (a:Si:H). It has to be noted that except amorphous silicon other materials can be used for manufacturing second-generation solar cells such as cadmium-telluride (CdTe) or CI(G)S. Another advantage of such solar cells is their flexibility, meaning that they can be installed even on rough surfaces. Despite their advantages, thin-film solar cells suffer from a lower efficiency which reaches 21.7% for CIGS (Solar Frontier), 21% for CdTe (First Solar) and 10.2% for a:Si (AIST) [15].

The third generation solar cells aim to produce either very high efficiency solar cells which will overcome the Schockley-Queisser limit or very cheap solar cells from abundant mate-

rials. So far multi-junction solar cells are being researched in order to achieve a very high efficiency. These solar cells consist of multiple cells stacked on top of each other, with a progressively lower bandgap. Such novel concepts have already achieved an efficiency up to 46% (Soitec) [15]. On the other hand, organic materials and dye sensitized solar cells suffer from a relatively lower efficiency of 11.2% (Toshiba) and 11.9% (Sharp), respectively [15].

1.2.1 The Photovoltaic Cell Working Principle

The solar cell's operation is based on the photovoltaic effect. The photovoltaic effect describes the potential difference between the junction of two different materials due to incident radiation. When these two materials are also connected through an external circuit there will be a flow of current, able to deliver power. A simple solar cell based on a PN junction is depicted in Figure 1.4, where p-type indicates the positive and n-type the negative type material respectively. There are three main processes taking place behind the photovoltaic effect namely generation of charge carriers, separation of charge carriers and collection of the carriers at the electrode.

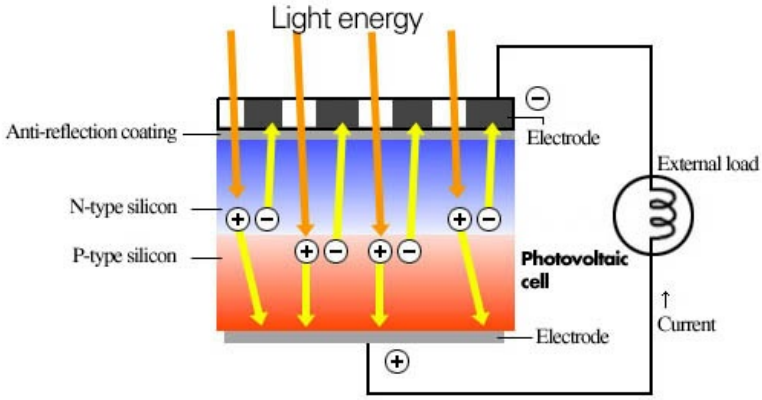

Figure 1.4: Basic Solar Cell Operation [16].

Generation of charge carriers

In order to understand the basic working principle of a solar cell the band diagram of the material is examined. Electrons in the valence band E_V are tight to an atom, while electrons in the conduction band E_C are free to move through the material, meaning they are able to conduct electric current. Generally, for a semiconductor the bandgap E_G is the energy difference between the top of the valence band and the bottom of the conduction band and it is considered that those energy levels within the bandgap are forbidden energy states for the electrons. When the semiconductor is under illumination it means that photons with different energy levels, as explained in Section 1.1, are incident on the material. If the incident photon has an energy equal to E_G it will be absorbed and in turn excite an electron from the valence to the conduction band. Since the electron is excited to the conduction band it leaves behind a void which is called a hole and considered to have a positive charge.

Furthermore, if the energy of the the photon is larger than E_G the electron will be excited to a higher energy state in the conduction band and it will then return to the edge of the conduction band by dissipating heat, which is known as thermalization losses. On the other hand, if the incident photon has a lower energy than E_G it will not be absorbed, but rather propagate through the material without exciting any electron and as a consequence it will not contribute to the generation of electric current. The aforementioned processes, in the order of explanation, can be visualized in Figure 1.5.

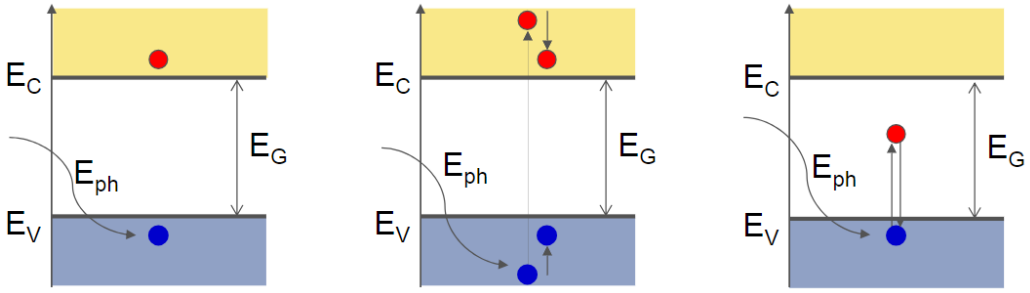

Figure 1.5: Generation of Charge Carriers [17].

The generation processes described earlier apply for a direct bandgap material, meaning that the maximum of the valence band occurs at the same wavevector as the minimum of the conduction band [18]. Such materials are able to absorb more light leading to a high absorption coefficient. Silicon, which is the main material used for most solar cells as demonstrated in Section 1.2, is an indirect bandgap material, meaning that the maximum of E_V and the minimum of E_C occur at different wavevectors. In such a material momentum is also required for an electron to be excited to the conduction band. This momentum needed can be realized by the vibrations of the crystal lattice and is considered to be supplied by phonons [10].

Separation of charge carriers

Since the electron-holes pairs have been created as described above, the next step is their separation. The electron and holes are of opposite charge, meaning that they are attracted by each other, tending to recombine. When electrons from the conduction band recombine with the holes it means that there are less free electrons leading to a lower electric current. The separation of charge carriers occurs at the PN junction of the semiconductor and can be imagined as a membrane which allows only one type of carrier to pass through, hindering recombination. A schematic representation of the PN junction under equilibrium is illustrated in Figure 1.6 .

Collection of charge carriers at the electrode

In the final step the carriers which have been created earlier are extracted from the solar cell through electrical contacts, providing power to the load. At this point an electric field

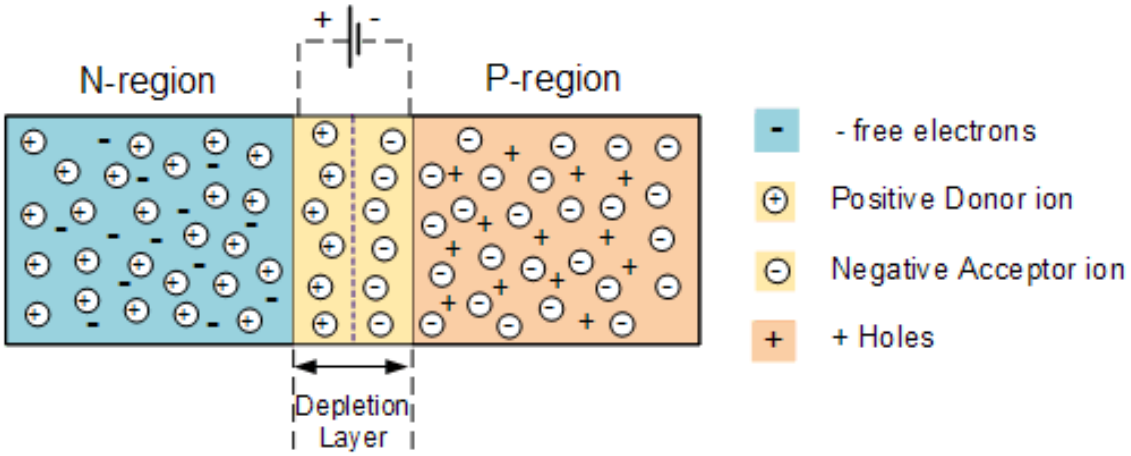

Figure 1.6: P-N junction in equilibrium [19].

at the junction causes a drift current which is equal to the diffusion current of the carriers. Thus when an external circuit is applied and the solar cell is illuminated the accumulated electrons at the n-type region will flow through it reaching the p-type region eventually recombining with the holes.

1.2.2 Recombination Mechanisms

Recombination is a loss mechanism of major importance encountered in solar cells. When recombination occurs the number of available charge carriers declines and as consequence the electric output of the solar cell is reduced. There are four different recombination mechanisms, namely Radiative, Auger, Schockley-Read-Hall (SRH) and Surface recombination. For each recombination process a recombination rate R and a minority carrier lifetime τ, which is the average time a charge carrier can travel within the material before recombining, can be realized. The carrier lifetime τ can be described by Equation 1.4.

$$\tau = \frac{\Delta n}{R} \quad or \quad \tau = \frac{\Delta p}{R} \tag{1.4}$$

Where Δn and Δp represent the excess carrier concentration for electrons and holes respectively.

Radiative recombination

Radiative recombination can be thought as the inverse process of absorbing a photon. In this recombination mechanism an electron falls from the valence band to the conduction band and recombines with a hole. During this process energy is emitted as a photon with

an energy equal to the bandgap energy E_G. This recombination mechanism is mainly encountered in direct bandgap materials, thus it is not of great importance in silicon solar cells, as a phonon is required to conserve energy and momentum simultaneously. For usual doping concentrations radiative recombination can be neglected [20]-[21].

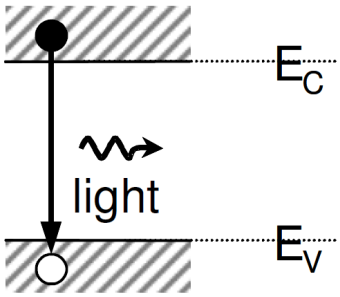

Figure 1.7: Radiative recombination mechanism [22].

Auger recombination

In silicon the dominant intrinsic recombination mechanism is Auger recombination [23]. Auger recombination is a three particle process in which energy and momentum are transferred to a third charge carrier, which in turn is excited deeper into the conduction or valence band. The excited charge carrier is then thermally relaxed to the most stable state and the energy is lost as heat known as *thermallization* losses. Since Auger recombination is a three particle process it can be understood that the more charge carriers are available (higher doping levels) the more important this recombination mechanism becomes [10]. The theoretical efficiency limit of a solar cell, taking into account Auger recombination, is 29.4% [13].

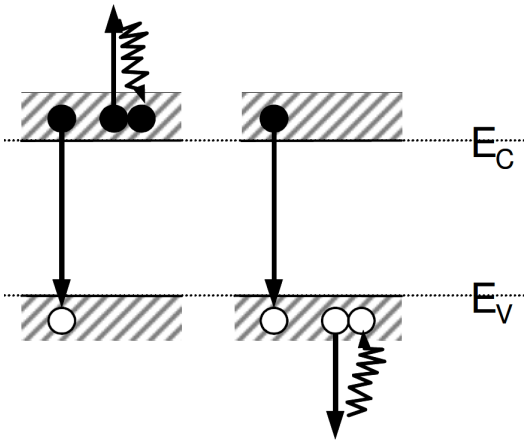

Figure 1.8: Auger recombination mechanism [22].

Shockley-Read-Hall recombination

Schokley-Read-Hall recombination is facilitated by impurities (such as Fe or Cu) or lattice defects. In this recombination mechanism the impurities and defects allow for energy levels in the forbidden gap, which are known as *trap states*. SRH recombination is a two step process where first the charge carrier is trapped in such a trap state and consequently recombines by dissipating heat. SRH recombination is considered to be one of the dominant recombination mechanism under operating semi-conductors. The more the trap states E_T present in the material the higher the SRH recombination.

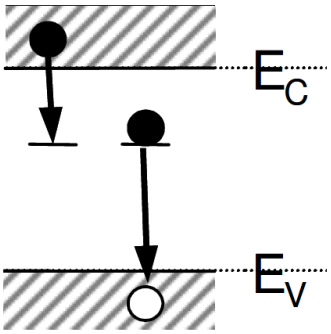

Figure 1.9: SRH recombination mechanism [22].

Surface recombination

The final recombination mechanism, as its name suggests, is not present in the bulk of the material but on its surface. In the surface of the material electrons cannot always create covalent bonds, leading to *dangling bonds*. As a consequence, these dangling bonds, which are actually defects, facilitate SRH recombination. The surface recombination rate (for an n-type semiconductor) can be described by Equation 1.5.

$$R = v_{th}\sigma_p N_{sT}(p_s - p_0) \tag{1.5}$$

Where v_{th} is the thermal velocity, N_{sT} is the surface trap density and σ_p is the capture cross-section for holes.

As it is obvious from Equation 1.5, the surface recombination can be reduced by either reducing the trap density N_{sT} or by reducing the excess minority carrier concentration p_s at the surface. Since nowadays high quality silicon wafers are used, the bulk of the silicon wafer has a very low defect density which results in an excellent bulk electronic quality. The dangling bonds at the surface of the silicon wafer are the main recombination centers, thus research is aimed towards reducing such defects present on the material's surface.

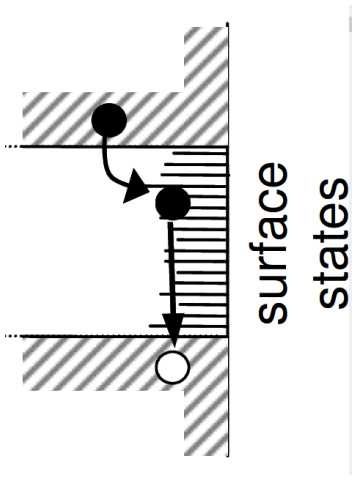

Figure 1.10: Surface recombination mechanism [22].

1.3 Passivating and Carrier Selective Contacts

In silicon wafers which are used nowadays, the bulk electronic quality has been improved at a point that further advantages in the performance of the device can be realized by interface passivation and carrier selective contacts. In reality the recombination at a silicon solar cell is dominated by the presence of lattice defects (dangling bonds) at the silicon surface as well as the recombination at the heavily doped regions, which in turn reduce the open-circuit voltage V_{oc} and efficiency of the solar cell [24]. Carrier selective passivating contacts (CSPC) allow the displacement of the metal contact from the silicon surface leading to high efficiency solar cells. In order to realize solar cells of high performance passivation is essential. Passivation can be realized by two different mechanisms, namely *chemical passivation* and *field-effect passivation.*

Chemical Passivation, as the name implies, refers to the chemical passivation of the silicon surface. When this passivation mechanism is considered, the number of the existing defects on the silicon surface is reduced by passivating the dangling bonds. Dangling bonds are passivated through the deposition of a thin layer, such as hydrogenated amorphous silicon (a:Si:H) or silicon oxide (SiO_x), on the semiconductor surface [25].

Field effect passivation is realized when an internal electric field is present allowing only one type of charge carrier to path, while blocking the other type of charge carrier. This means that different conductivities need to be established for each type of carrier. As an example, for a hole contact, the conductivity of the holes should be high and vice versa for an electron contact the conductivity of holes should be low [26]. The most simple way of achieving field effect passivation is by heavily doping. Such a heavily doped region allows for a low resistivity, leading to a high FF but on the other hand a low V_{oc} value is expected due to the high saturation current J_o at the contact.

1.3.1 Silicon Heterojunction Solar Cells

Silicon Heterojunction solar cells are part of the emerging technology of passivating contacts. An outstanding efficiency of 26.7% was achieved for such a SHJ solar cell by Kaneka Corp. featuring a FF of 84.9% [27]. Such a high FF can be achieved only under the conditions that both transport losses as well as recombination in low level injections have to be very low [28].

In this type of technology two different semiconductor materials are used, each with a different bandgap E_G. SHJ contacts are usually formed through the deposition of an intrinsic hydrogenated amorphous silicon (a-Si:H) layer and a doped a-Si:H layer at both sides of the silicon wafer. The a-Si:H layer acts as a chemical passivation layer by reducing the defect density at the surface, enabling very high V_{co} values for this type of structure. A high hydrogen content has been shown to boost the passivation quality of such contacts [29–31]. On top of the intrinsic layer a doped layer is deposited in order to achieve field effect passivation, meaning the the minority carriers are repelled and not accumulated over the surface, ensuring a low recombination. Finally, a transparent conductive oxide (TCO) is deposited in order to enhance the lateral conductivity for the carriers, since the doped layers are not highly conductive. This TCO acts additionally as an anti-reflection coating at the front side in order to ensure a higher optical performance.

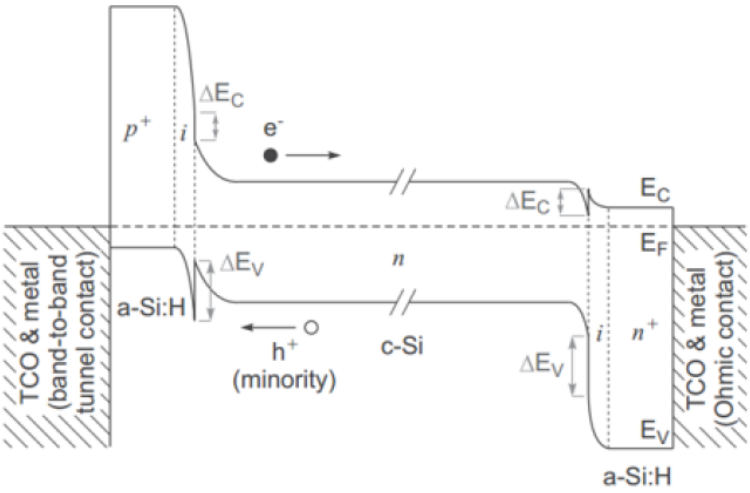

Figure 1.11: Band diagram of a SHJ solar cell [32].

In Figure 1.11 the band diagram of a SHJ solar cell is illustrated. The a-Si:H has a higher bandgap in the range of 1.7-1.8 eV, depending on the hydrogen content of the material, compared to c-Si which has a bandgap of 1.12 eV. When these two materials are connected the so-called heterojunction is formed. The band offsets are depicted as ΔE_C and ΔE_V for the conduction and valence band respectively, inducing field-effect passivation. In the hole contact, holes accumulate at the interface between c-Si and a-Si:H due to the band offset ΔE_V and then through tunnelling they are able to overcome the energy barrier and pass to the p-type a-Si layer and consequently be collected at the electrode. On the other

hand, electrons are repelled due to the large energy barrier induced by the p-type a-Si layer. Under the same principle, in the electron contact holes are repelled due to the large energy barrier induced by the n-type a-Si:H layer while electrons are able to pass through the junction and be collected at the electrode.

Parasitic absorption can substantially decrease the performance of a SHJ cell. The doped and intrinsic amorphous layers have a bandgap of in the range of 1.7-1.8 eV, leading to a high absorption in the short wavelength region of the spectrum and consequently losses in the current [33]. As a consequence optimization is needed in order for the a-Si:H to be as thin as possible but still provide a sufficient passivation quality. In the infrared part of the spectrum current losses are mainly encountered due to free-carrier absorption (FCA) [23].

1.3.2 Poly-Silicon Passivating Contact Solar Cells

Passivating Contacts based on poly-silicon originate already from 1985 when a semi-insulating polycrystalline silicon achieved an open-circuit voltage of 720 mV [34]. Thereafter, this poly-silicon passivating contact has also been incorporated in solar cells with the use of an interlayer of a silicon-oxide (SiO_x), resulting in a poly-Si/SiO_x interface. The combination of a diffused front emitter and a passivating rear contact is known as *Tunnel Oxide Passivating Contact (TOPCon)* and developed by Fraunhofer ISE. Fraunhoger ISE is also the holder of the record efficiency of 25.7% on a TOPCon solar cell, with a V_{OC} of 725 mV, a FF of 83.3% and a short-circuit current J_{sc} of 42.5 mA/cm^2 demonstrating the great potential of such passivating contacts [35].

In the recent years, research has been aimed towards further increasing the performance of the poly-silicon passivating contacts in various ways. IBC, Top/Rear poly-silicon and hybrid solar cells have been researched in order to obtain high efficiency and the results of the progress on the solar cell efficiency are illustrated in Figure 1.12.

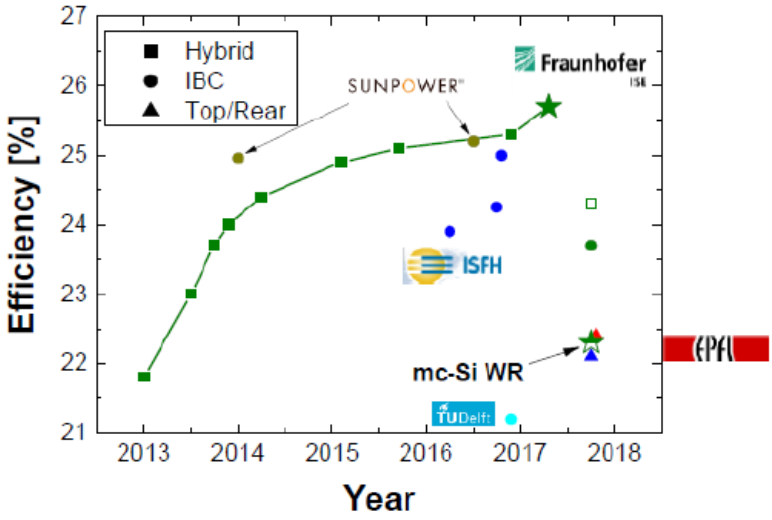

Figure 1.12: Lab scale efficiency achievement of Poly Si Contacts [36].

Two different structures based on poly-silicon are depicted in Figure 1.13. The first one is the TOPCon structure, which was already mentioned earlier, and the second one is the *poly-silicon on oxide (POLO)*. Their main difference is the fact that TOPCon structure has a diffused front emitter while the POLO structure has a poly-silicon front passivating contact.

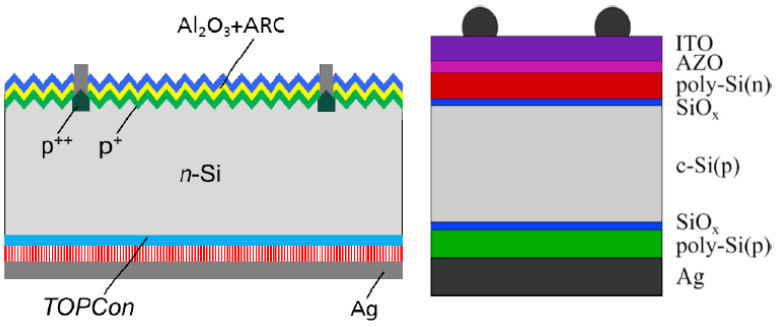

Figure 1.13: TOPCon solar cell structure [37] and POLO solar cell structure [38].

Regarding the fabrication of such cells, firstly the ultra-thin tunnel oxide layer is deposited on the silicon wafer. This tunnel-oxide can be grown by means of wet chemical oxidation, using boiling nitric acid [35, 39–41], thermally [42] or by the use of UV light in order to create ozone [43]. Following, an a-Si:H layer is deposited on the oxide. The Si layer doping can be introduced in-situ (during deposition) or ex-situ (by ion implantation) . The Si layer deposition can be performed by low pressure vapour deposition (LPCVD) [44–46] or by plasma enhanced chemical vapour deposition (PECVD) [45, 47, 48]. In the final step, the structure is annealed at a high temperature, usually between 800-950 °C, which crystallizes the Si layer, leading to the poly-Si contant, and activates the dopants.

In Figure 1.14 the band diagram of an electron poly-silicon passivating contact is illustrated. Due to the difference in the work function of the heavily doped n^+ poly-Si and Si bulk band bending can be induced, meaning that electrons will accumulate towards the n^+ poly-Si layer and tunnel through the oxide while the holes will be repelled. This translates to a large electron conductivity and a small hole conductivity in that region, which ensures carrier selectivity. The tunnel oxide provides an energy barrier for charge carriers but if thin enough tunneling can occur. This tunnel oxide has a barrier of 3.1 eV for electrons and 4.5 eV for holes [39]. Furthermore, the tunnel oxide layer is responsible for the chemical passivation of the Si surface, since it passivates the dangling bonds reducing that way the number of trap states.

The ultra-thin oxide plays a crucial role in the chemical passivation of the Si, since it is passivating the dangling bonds present [49]. Furthermore, the silicon oxide layer acts as a barrier to the diffusion of dopants to the c-Si during the high temperature annealing process. A diffusion of dopants to the c-Si hinders the field effect passivation of the contact, thus a thick enough oxide layer is needed. On the other hand, a very thick silicon oxide layer will not allow the tunneling of the carriers leading to low FF values [35]. The optimal

oxide thickness is considered in the range of 1.2-1.8 nm [48, 50–52].

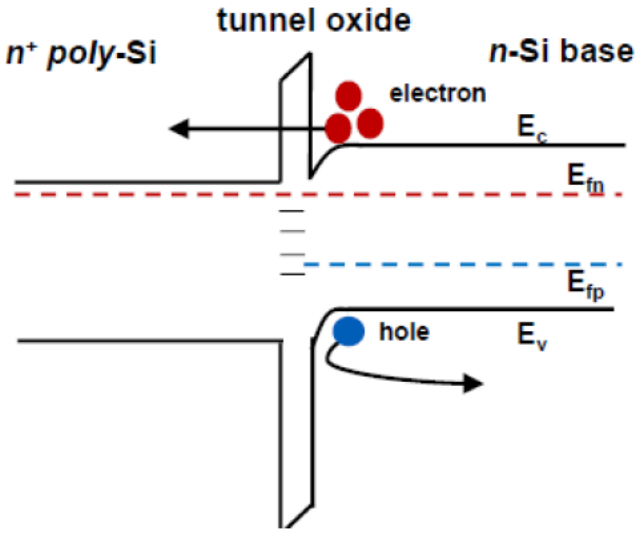

Figure 1.14: Band diagram of an electron poly silicon passivating contact [39].

As already explained the silicon oxide is of vast importance for the passivation of the c-Si, thus it needs to be maintained for the optimal performance of the solar cell. However, during the annealing process the silicon oxide layer could be disrupted. It has been found that for annealing temperatures in the range of 900 °C local disruptions in the silicon oxide can be observed according to the chemical reaction $SiO_2(s) + Si(s) \rightarrow 2SiO(g)$ [39, 40, 52]. This causes the thickness of silicon oxide layer to decrease and pinholes could be formed at such high temperatures, introducing a deteriorated passivation quality [52, 53].

Furthermore, the doping profile is of great significance in the field effect passivation. A low doping level will result in an increased interfacial recombination due to weaker band bending, while a very high doping level can cause diffusion of dopants into the c-Si bulk decreasing the carrier selectivity [42, 44] or even cause parasitic absorption due to FCA [45]. In general for an effective field effect passivation a steep drop in dopant concentration needs to be realized in the oxide interface [44].

Despite the excellent passivation quality introduced by the poly-Si passivating contacts important drawbacks are also present. The poly-Si layer can induce parasitic absorption in the short wavelengths, due to its higher E_G, making its use tricky when incorporated at the front contact of the solar cell. In order to tackle this disadvantage the poly-Si layer thickness should be in the range of 10-40 nm [38]. Furthermore, poly-Si is more resistive compared to Si, leading to a lower carrier mobility affecting the FF.

1.3.3 Other Passivating Contacts

In the aforementioned passivating contacts heavy doping of the layers is required in order to induce band bending and an efficient filed effect passivation. However, one drawback of a heavily doped region is the presence of more carriers, leading to higher Auger recombination as explained in Section 1.2.2. This increased doping level has negative effects on the both the short-circuit current as well as the open-circuit voltage of the device [23]. Furthermore, the a-Si:H layer in SHJ cells and the poly-Si layer in TOPCon/POLO cells have a high bandgap compared to Si, which induces parasitic absorption of the light, especially in the blue and ultra-violet part of the spectrum, further reducing the short-ciruit current. In order to tackle these drawbacks transition metal oxides are being researched, which can either replace the doped silicon layer or can be inserted between the TCO and the doped silicon layer [54].

Substoichiometric molybdenum oxide (MoO_x) is being researched as a hole selective contact [23, 55, 56]. It has a high work-function of 6.6 eV and it can act as an effective hole contact without any doping. Additionally, it is a high band-gap material of approximately 3 eV, which can be used at the front contact in order to reduce parasitic absorption at the blue and ultra-violet part of the spectrum. In addition, such contacts have demonstrated high V_{OC} values up to 711 mV [56] and an efficiency of 18.8%. Furthermore, other research has been made with lower V_{oc} values of 630 mV [54]. Another transition metal oxide being researched is the WO_x which has achieved open-circuit values of 660 mV [54].

Apart from their excellent blue and ultra-violet response these materials also benefit from the low thermal budget needed for their fabrication. Both MoO_x and WO_x require a thermal budget of less than 200 °C, which is considerably less than the thermal budgets needed during the annealing process of the poly-Si passivating contacts. However, depsite their advantages further research is needed in this field in order to realize better operating devices and higher efficiencies.

1.4 Motivation

As already mentioned the installed capacity of PV is growing every year. In order for PV to become one of the main sources of energy the Levelized Cost of Energy (LCOE) of PV should be decreased further and become competitive with the traditional energy sources. Non-module costs such as inverters, Maximum power point trackers, mounting etc , which are called Balance of System make up a large part of the total cost of a PV system. By increasing the module efficiency the energy produced over the lifetime of the module is increased and consequently the LCOE drops. Thus, increasing the solar cell's efficiency is of major importance.

Since the base material used nowadays is already of excellent quality, there are very few defects present in the wafer, thus the bulk recombination is considerably low leading to consistent open-circuit voltage (V_{oc}). However, in the interface between the c-Si bulk and the metal contact surface recombination occurs hindering the cell's efficiency. Several strategies

have been proposed so far for the reduction of the surface recombination such as Passivated Emitter and Rear Cell (PERC)[57], which deploys a thermal oxide passivation layer and local contacts. The next strategy, to cope with V_{OC} limitations is the use of carrier selective passivating contacts (CSPC). CSPC, as their name suggest, offer a high carrier selectivity through the band offsets and also passivate the surface from dangling bonds. One excellent example of CSPC is the silicon-heterojunction (SHJ) device which has reached an impressive efficiency of 26.7% [27]. Another example of CSPC is the Tunnel Oxide Passivated Contact (TOPCon), which makes use of a diffused emitter and a passivated, through a dielectric, full-area rear contact reaching an efficiency of 25.7% [35]. Furthermore, in recent research poly-silicon on oxide (POLO) solar cells are investigated, which use poly-silicon passivating contacts both at the front and rear of the solar cell.

In this project a poly-Si passivating contact alloyed with carbon (poly-SiC_x) is developed in order to further improve the performance of the POLO structure. It has to be noted that poly-SiC passivating contacts are still under investigation due to advantages such as a tunable bandgap which can be achieved through the carbon content. Additionally, poly-SiC_x passivating contacts demonstarate a high thermal and mechanical stability.

By the incorporation of carbon in silicon the resulting material becomes more resilient to blistering when deposited on the silicon-oxide layer. Blistering can occur through hydrogen effusion and ruptured blisters provide a diffusion path for the metals during the metallization process, which in turn hinder the passivation qualtiy [47]. Following the carbon alloying, the diffusion coefficient of hydrogen is reduced while the temperatures of hydrogen effusion peaks increase [58]. Furthermore, the hydrogen-carbon bonds are more stable compared to the hydrogen-silicon bonds [59, 60]. The combination of the two aforementioned characteristics tend to hinder the formation of blisters due to hydrogen effusion during the thermal treatment required in the fabrication process of the solar cell.

Alloying the a-Si:H layer with carbon results in widening of the bandgap, obtaining advantageous optical properties depending on the carbon content [58]. Furthermore, poly-Si is able to provide a very strong doping enhancing carrier selectivity. Thus, alloying poly-Si with carbon could result in a material which can be highly doped and also its optical properties can be tuned depending on the carbon content.

Crystalline and stoichiometric SiC materials are well known for their chemical inertness, thus such layers are considered stable in many chemical etching solutions which are used during the solar cell's fabrication process [61, 62]. Due to its stability in such chemical solutions, the SiC_x layer can be used as a side protective layer through the fabrication process, which can offer great flexibility. Finally, poly-Si and poly-SiC have a higher thermal stability compared to other passivating contacts such as SHJ offering greater flexibility and compatibility with solar cell's industry.

To sum up, the optimization of a solar cell's structure with an alloyed material such as SiC_x could be of great interest since the blistering effect can be hindered, the optical properties as well as the band bending can be tuned depending on the carbon content, the SiC_x

layer can also provide wet-chemical stability during the fabrication process and such CSPC demonstrate a high thermal stability.

1.5 Research Objective

The objective of this thesis is the fabrication of a high-efficiency solar cell implementing poly-SiC_x passivating contacts. For such a solar cell to be realized, various experiments have to be carried out in order to understand the effect of the material's properties on the cell's performance. Furthermore, different fabrication parameters have to be examined (annealing temperature and time, deposition methods) as well as the effect of different hydrogenation techniques. By finding an optimum balance between all those steps solar cells with SiC_x passivating contacts were fabricated.

The main research questions of this thesis are :

- What is the effect of carbon content on the material composition and optical properties?
- What is the influence of PECVD deposition parameters on the passivation quality of the poly-SiC_x?
- How does the deposition of an a-Si:H interlayer affect the passivation quality of poly-SiC_x passivating contacts?
- What is the optimal hydrogenation temperature, duration and capping material for poly-SiC_x passivating contacts?

1.6 Thesis Outline

This thesis work consists of 6 chapters, aiming on the optimization of poly-SiC_x passivating contacts and thus realizing a solar cell implementing the aforementioned contacts at the front and the rear.

In Chapter 2, the experimental methods followed are provided. Firstly, the processing techniques are provided in detail with additional information regarding the equipment which was used. Furthermore, the characterization techniques are introduced, where all the equipment used for determining the electrical, optical and material properties is presented alongside a brief introduction on the fundamental physics behind those measurements.

Chapter 3 focuses on the material properties of the poly-SiC_x layers fabricated. Different characterization techniques are used in order to gain an insight in the material properties as well as the electro-optical properties of the deposited poly-SiC_x layers.

In Chapters 4 and 5 the experimental results are presented and discussed. In Chapter 4 the poly-SiC_x passivating contacts are examined in symmetrical structures. As a result,

different deposition parameters are examined in order to optimize the passivation properties. Furthermore, a hydrogenation optimization is presented in the same chapter in order to further enhance the passivation of the aforementioned contacts. In Chapter 5, poly-SiC_x passivating contacts are implemented on a solar cell. Solar cells with a front and back contacted scheme are fabricated and different configurations are tested in order to increase the solar cell's efficiency.

In the final Chapter 6, the conclusions of this thesis work are presented. A summary of the most important aspects investigated and of the results is provided in order to briefly understand the progress made through this thesis work. Furthermore, an outlook of the possible ways to further improve the performance of the so far fabricated solar cells is given, which could be a starting point for future research.

Chapter 2

Experimental Methods

In this chapter the experimental methods for the fabrication and characterization of symmetrical samples/solar cells is provided. A brief introduction of the working principle behind each process is given, alongside the parameters used during the fabrication procedure. The sequence of the processes treated is in the same order as followed during the fabrication of the samples. Furthermore, the working principle behind the characterization methods used will be addressed.

2.1 Samples and Cells Preperation

2.1.1 Wafer Cleaning

In this project high quality (n-type) Float-Zone (FZ) c-Si wafers, manufactured by *TOPSIL*, were used. The specifications of these wafers are provided in the Table 2.1. The reason behind using n-type wafers as the bulk material is that p-type wafers suffer by boron-oxygen light induced degradation[63]. Furthermore, n-type wafers are expected to demonstrate a higher minority carrier lifetime due to a lower sensitivity to recombination caused by various transition metals [63].

Table 2.1: Wafer specifications.

Characteristic	**Value**
Diameter	100± 2
Thickness [μm]	280 ± 2
Doping	n-type
Orientation	100
Resistivity [ohm-cm]	1-5
Finish	Polished

Before any processing can be realized the wafers need to be properly cleaned in order to remove any particles and organic/inorganic residues from its surface. Firstly, the wafer is immersed in a 99% HNO_3 solution for 10 mins and then it is rinsed in deionized water (DI water) for 5 mins. Following the wafer is immersed in 68% HNO_3 solution at 110°C again

for 10 mins and subsequently rinsed in DI water for 5 mins. This step ensures the removal of organic and inorganic contamination [64].

During this cleaning process and storage a native oxide layer is formed on the surface of the wafer. The native oxide formed is then etched by a dip in 0.55% hydrofluoric acid (HF) for 4 mins. Finally, the wafer is rinsed for 4 mins in DI water and in the end isopropyl alcohol (IPA) vapor is added for 1min in order to dry the wafer. This last step is referred as *Marangoni* and it is done right before the subsequent procesing step to offer a bare surface for the growth of the silicon oxide (SiO_x).

2.1.2 Chemical Oxide Growth

The next step in the fabrication process is the growth of the silicon oxide (SiO_x). In this project the silicon oxide was grown wet-chemically with the method of Nitric Acid Oxidation of Silicon (NAOS). In order for the ultra-thin oxide layer to be grown the wafer is immersed in a 69.5% HNO_3 solution for 1 hour, straight after the Marangoni step, and then followed by a 4 mins rinse in DI water.

During this process an ultra-thin oxide layer is formed in the range of 1.3-1.5 nm [65]. This oxide layer is homogeneous in thickness, thus it also has a low leakage current density [66, 67]. One advantage of this method is its simplicity and the low thermal budget it needs compared to other oxide growth methods such as thermal, which requires temperatures in the range of 600-700 °C. However, the chemical grown oxide demonstrates a lower thermal stability which could lead to its breaking during the annealing process as described in Section 1.3.

2.1.3 Low Pressure Chemical Vapour Deposition (LPCVD)

Low Pressure Chemical Vapour Deposition (LPCVD) process is used in the field of semiconductors in order to deposit thin-films with thicknesses ranging from a few nanometers to many micrometers. LPCVD depositions are usually performed in temperatures in the range of 600-660 °C when SiH_4 is used and the process gas is added in pressures between 10-1000Pa [68]. One advantage of using an LPCVD process is the considerably lower reactant diffusion, which results in excellent purity and homogeneity. Furthermore, the layers deposited through an LPCVD process are uniform and free of pin-holes, which ensure the protection of the tunnel oxide layer in the subsequent deposition steps and chemical treatments [42]. The schematic of an LPCVD reactor is illustrated in 2.1.

In this project an LPCVD furnace by *TEMPRESS SYSTEMS* located in EKL CR100 was used in order to deposit an a-Si layer on both sides of the wafer. The temperature used during this LPCVD deposition was 580 °C, the pressure set at 150 mTorr and the SiH_4 gas flow at 45 sccm. With these parameters a deposition rate of approximately 1.56 nm/min was obtained. Finally, an annealing step at 600 °C for one hour is performed in order to

release the stress.

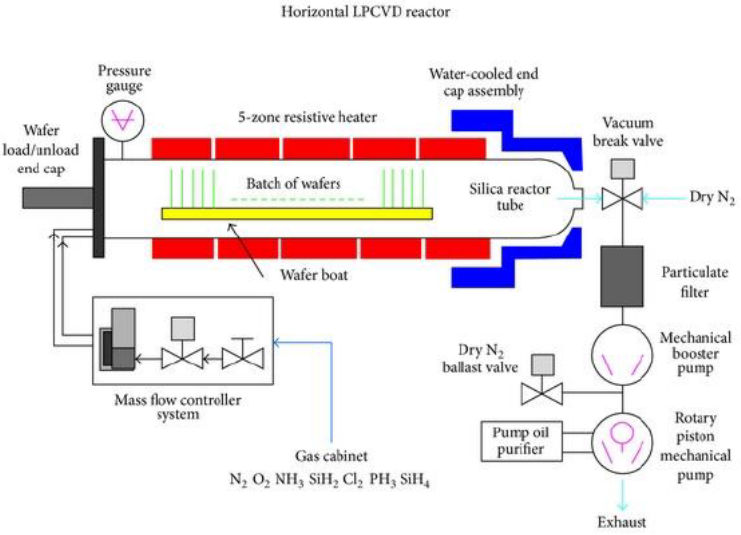

Figure 2.1: LPCVD reaction chamber [69].

2.1.4 Plasma Enhanced Chemical Vapour Deposition (PECVD)

Plasma Enhanced Chemical Vapour Deposition (PECVD) is a widely used technique for depositing thin films on a substrate. PECVD depositions are low-temperature depositions (200-400 °C) and they can ensure that the resulting layer is of high quality as well as homogeneous. The schematic of the PECVD machine used is depicted in Figure 2.2. The RF generator creates the plasma between the electrodes and as consequence electrons are accelerated and collide with the gas precursors, forming radicals. Those radicals are then deposited on the surface of the substrate to form the thin-film layer. PECVD is a rather sensitive process where various parameters such as RF power, gas flow, gas pressure and temperature all contribute to the quality of the final product.

In this work the PECVD machine *AMOR* manufactured by *Elettrorava* was used. The main components consist of an RF power generator, a gas supply, a heater, pumping system, 4 deposition chambers and a flipping chamber. For this project, chamber 1 was mainly used which is intended for p-type doped layers, with a substrate temperature of 180 °C. Since p-type a-SiC:H layers were deposited, the gasses used were silane (SiH_4), methane (CH_4) and diborane (B_2H_6) in different flow ratios. Furthermore, the pressure was set at 0.7 mbar and the RF generator power at 3 W.

Additionally, the a-Si layer mentioned in the previous section, can also be deposited by PECVD. Regarding the a-Si layer deposited by PECVD, chamber 3 was used which has a pre-set temperature of 292°C. For the a-Si layers deposited in this work only silane (SiH_4) gas was used at a flow rate of 40 sccm. The pressure was set at 0.7 mbar and the RF

generator power at 2.7 W.

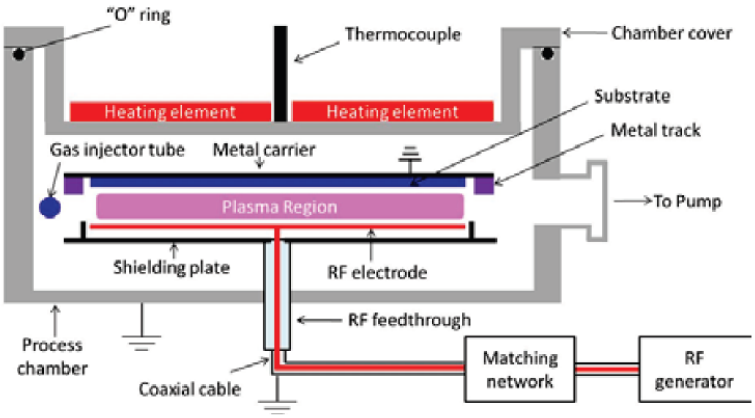

Figure 2.2: PECVD reaction chamber [70].

2.1.5 High-Temperature Annealing

After the thin dopant rich layers have been deposited, according to the previously mentioned procedures, the samples are annealed in a *TEMPRESS SYSTEMS* furnace. The annealing process takes place under a N_2 atmosphere at variable temperatures (825 °C - 875 °C) and durations (0/5 minutes). It has to be noted at this point, that the furnace heating was performed at a rate of 10°C/min, consequently durations given here indicate the set temperature, not including the heating and cooling down steps as shown in Figure 2.3.

The annealing step is responsible for the crystallization of the a-SiC_x layers deposited, leading to a poly-SiC_x layer, which has superior electrical and optical properties compared to the amorphous one. The crystallized layers have a reduced series resistance due to the high doping efficiency and mobility of such layers compared to the amorphous ones [40, 41, 62]. Furthermore, this high-temperature annealing step activates the dopants which are saturated by H and have have been earlier deposited through the PECVD process. However, during this procedure it is possible that some boron atoms in the poly-SiC_x layer will diffuse too far into the c-Si bulk, hindering the field effect passivation as stated in section 1.3.2. Thus, the annealing temperature and duration needs to be optimized in order to obtain the desirable dopant profile in the interface of the c-Si and the poly-SiC_x layer.

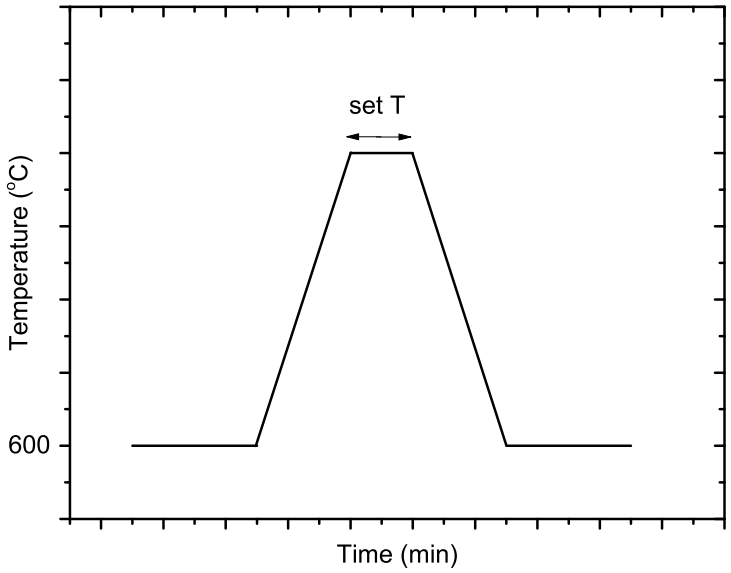

Figure 2.3: Temperature ramping during the thermal annealing.

2.1.6 Hydrogenation

Hydrogenation is a process of great significance when coming to the fabrication of high efficiency solar cells. In Section 1.2.2, the various recombination mechanisms occurring during the operation of a solar cell were addressed. It was mentioned that dangling bonds present in the material, can act as recombination centers hindering the performance of the solar cell. The tunneling oxide alone is not able of providing sufficient surface passivation after the thermal treatment, thus hydrogenation is performed in order to improve the electronic quality of the material and as a consequence improve the passivation quality by further minimizing the interfacial defect density[63]. During the hydrogenation process H atoms are provided which are able to passivate the aforementioned dangling bonds, thus ensuring an improved chemical passivation [71]. In this work, we perform hydrogenation using a sacrificial layer, SiN_x [72] or AlO_x [73], rich in hydrogent content. Furthermore, an annealing in Forming Gas atmosphere (FGA) is also used to help the H diffuse in the stack and further enhance passivation [71, 73]. SiN_x layers are deposited by PECVD, while AlO_x layers via Atomic Layer Deposition (ALD).

Regarding the ALD of Al_2O_3, the *Flexal ALD* manufactured by Oxford Instruments was used. The temperature of the chamber during the deposition was kept at 250°C, while the pressure was set at 15 mTorr. The precursor gasses used were Trimethylaluminium (TMA) and H_2O. In this process each cycle is able to deposit roughly 1Åof AlO_x. Alternatively, the PECVD deposition of SiN_x, was perfromed on *Plasmalab80Plus* manufactured by Oxford Instruments where both LF and RF generators were used. The precursor gasses were Silane (SiH_4) and Ammonia (NH_3) at a temperature of 400°C and a pressure of 650 mTorr. During this process hydrogen radicals are generated from SiH_4 and NH_3 which can passivate the

dangling bonds of the material. Finally, a FGA was performed in order to both provide additional H during the annealing but also in order to release the incorporated H atoms of the deposited AlO_x and SiN_x layers. FGA was performed at a *TEMPRESS SYSTEMS* furnace at variable temperatures (400-500°C) and durations (30/60 minutes). The FGA was performed in a H_2 atmosphere, where the H_2 flow was kept at 400 sccm.

2.1.7 Transparent Conductive Oxide (TCO) Deposition

Transparent Conductive Oxides (TCO) are thin films which are optically transparent and at the same time electrically conductive. The deposition of such films ensures a high lateral conductivity for electrons to the metal electrodes and also with an appropriate thickness they can additionally serve as an anti-reflection coating ensuring efficient light trapping. In this work, Indium Tin Oxide (ITO), developed by other members of the PVMD group, was used which consists of 90% indium oxide (In_2O_3) and 10% tin oxide (SnO_2). The ITO was deposited through physical vapor deposition method known as sputtering. The deposition took place in a chamber with a temperature of 196 °C, the pressure was kept at $2.20 \cdot 10^{-2}$ mbar and the power equal to 135 W. The aforementioned conditions had been previously tested by other PVMD group members, to ensure that no sputtering damage occurs during the deposition process. In order for the ITO to serve also as an anti-reflection coating, its thickness at the front side was 75 nm while at the rear 120 nm, ensuring a sufficient charge carrier transport and also a sufficient light trapping.

2.1.8 Metallization

The final step in the fabrication process of solar cells is the metallization. Through, this step the contacts are formed in order for the current to flow. In this thesis work, front and back contacted (FBC) cells were fabricated. The rear of the cell received a full-area contact while the front metallization was patterned. A trade-off between J_{sc} and FF exists with the finger spacing, for the front patterned contact. A small finger spacing results in higher FF due to the lower resistance for lateral transport. On the other hand, a smaller finger spacing means that more fingers are present on the front side of the cell causing shading, thus lowering the J_{sc}.

For the metallization different techniques and materials are investigated in this work (Chapter 5). For the front, a patterned contact by means of silver(Ag) Screen-Printing (SP) is applied. Regarding the rear full-area contact, either Ag SP or Ag and Al evaporation is used in the Provac machine. In Provac, the Al or Ag is heated in order to reach a higher temperature than its melting point, causing the evaporation. The evaporated material fills the chamber and accumulates over the cell's surface realizing the contact. This process is performed under vacuum ensuring a high quality of deposition.

In Figure 2.4, the front patterned contact and the full-area rear contact are illustrated. The mask used for the front contact during the SP results in 4 cells in the area of the wafer. The cell which is used in this thesis work is the cell inside the red box. This metallization

pattern results in a shading of 12%.

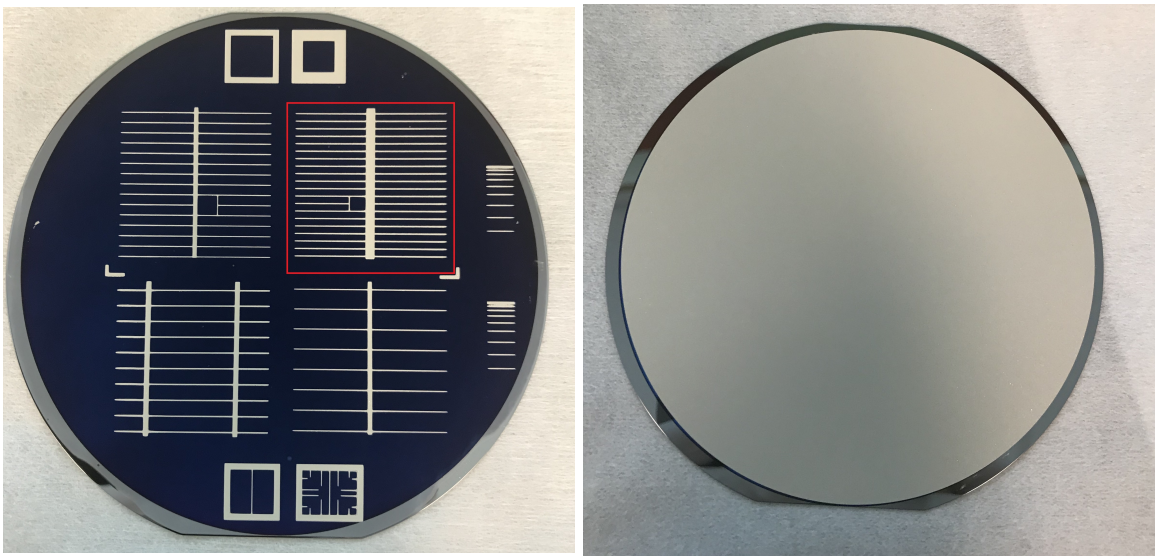

Figure 2.4: Front patterned contact and rear full-area contact. The cell in the red box represents the metallization pattern examined in this work.

2.2 Characterization Methods

2.2.1 Material Characterization

In this section the material characterizations performed are presented. These characterization techniques are performed in order to gain an insight into the material composition and the bonds present in the deposited layers.

Raman Spectroscopy

Raman Spectroscopy is a technique used in order to observe vibrational, rotational and other low-frequency modes of a system. When a photon interacts with a molecule it can be absorbed, scattered or go through the molecule depending on the photon's energy. When the light is scattered the photon can have the same, lower or even higher energy than the incident light.

When the energy of the scattered photon is the same as the incident light *Rayleigh* scattering occurs. On the other hand when the energy of the scattered photon is of a different energy level *Raman* scattering occurs. If the energy of the scattered photon is lower than its initial energy it means that part of the energy has been transfered to a molecule in the lattice of the material and caused it to vibrate [74]. The Raman shift (ΔW) is the energy difference of the incident and scattered photon. The amount of light which undergoes

Raman scattering is very low, approximately one every 10^6-10^8 photons undergoes Raman scattering, meaning that such measurements are very sensitive [75].

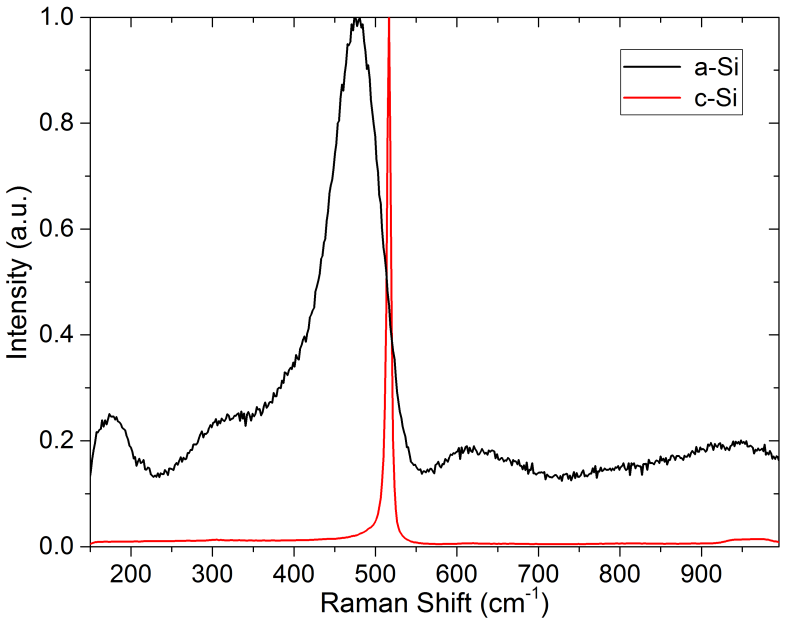

Figure 2.5: Raman spectrum of c-Si and a-Si.

For this project the Renishaw inVia Raman microscope was used with a green laser (514nm) at 5% power, 100 seconds scan time and 1 accumulation. During the Raman measurement the number of Raman shift occurances are registered in a certain spectrum and timeframe. When a certain peak is observed in the Raman shift, it can be attributed to a certain bond. For example the Raman measurement for a-Si and c-Si is depicted in Figure 2.5, where a sharp peak is observed at 520 cm^{-1} corresponding to c-Si which has highly uniform bond angles and lengths while a wider peak at 480 cm^{-1} corresponds to a-Si, due to its disordered form.

Furthermore, the shape and the intensity of the peaks observed in the Raman measurements can provide information related to the concentration of bonds in the material. In such a way, the crystallinity fraction (X_C) of the examined material can be estimated through Equation 2.1, given below:

$$X_C = \frac{I_{c-Si}}{I_{c-Si} + \gamma \cdot I_{a-Si}} \tag{2.1}$$

Where $I_{c\text{-}Si}$ represents the area beneath the c-Si peak at 520 cm^{-1}, $I_{a\text{-}Si}$ represents the area beneath the a-Si peak at 480 cm^{-1} and γ is a correction factor used for the difference in the cross section between c-Si and a-Si for phonon excitation. This correction factor is set at 0.8 according to [76].

Fourier-Transform Infrared Spectroscopy (FTIR)

In order to get an insight on the microstructure of the deposited layers Fourier-Transform Infrared Spectroscopy (FTIR) was used. The goal of this measurement is to determine the vibration modes of various bonds in the deposited layers. The equipment used during those measurements was Nicolet 5700 manufactured by *Thermo Fisher*.

In such measurements, a beam in the infrared region is emitted by the source which then hits a beamsplitter. The beamsplitter allows part of the light beam to be transmitted towards a movable mirror and part of the light beam is reflected towards a stationary mirror. Following, the beams reflected by the two mirrors recombine at the beamsplitter. Depending on the position of the movable mirror, and as a consequence the distance the light beam travels, constructive or destructive interference can be realized. As a result, the reflection can be obtained and depending on the peaks information can be obtained regarding the bonds present in the material. Following, the peaks were fitted with a Gaussian profile.

2.2.2 Optical and Electrical Characterization

In this section the optical and electrical characterizations performed are discussed. These characterization techniques are performed on wafer or quartz glass samples, providing valuable information on the material composition as well as the electro-optical and characteristics of the deposited layers.

Spectroscopic Ellipsometry

Spectroscopic ellipsometry (SE) is a commonly used method for obtaining information regarding the optical properties and thickness of thin films, while also demonstrating a high accuracy. In such measurements, the shift in the polarization of the light is measured which originates from the interaction of the light source with the deposited film, and this change of polarization depends on the material's properties and thickness. Following, the reflectance ratio ρ is acquired by the amplitude ratio Ψ and the phase difference Δ through Equation 2.2.

$$\rho = \frac{r_p}{r_s} = tan\,\Psi e^{\Delta} \tag{2.2}$$

The reflectance ratio ρ is the ratio between the Fresnel reflection coefficient for P-polarized light r_p and S-polarized light r_s. After, measured data are fitted into a model in order to obtain the information regarding the thin film's thickness and optical properties. The measurement setup is depicted in Figure 2.6.

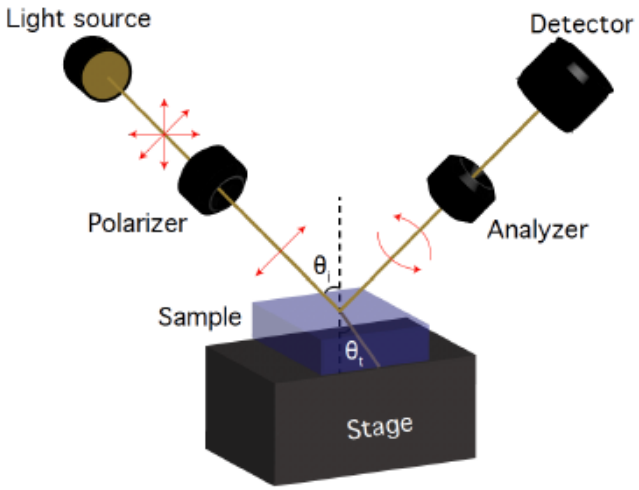

Figure 2.6: Spectroscopic Ellipsometry measurement setup [77].

In this work, SE was used for measurements on quartz glass and wafers in order to obtain the thickness of the deposited layers and calculate the deposition rate for different gas flows. It has to be noted that the measurements were performed in angles close to the *Brewster's angle*, where the difference between S- and P-polarized light is at its maximum, and the reflectance of the P-polarized light is zero. For this thesis, angles between 65° and 75° were measured for wafer samples and between 50° and 70° for quartz glass, all with a step of 5°.

Ultraviolet-Visible Spectroscopy UV/VIS

In order to gain an insight in the optical properties of the material Reflectance (R) and Transmittance (T) measurements were performed. The equipment used for such measurements was the PerkinElmer Lambda 950 spectrophotometer, which consists of a deuterium and a tungsten-halogen lamp able to provide light in the range of 175-3300 nm [78].

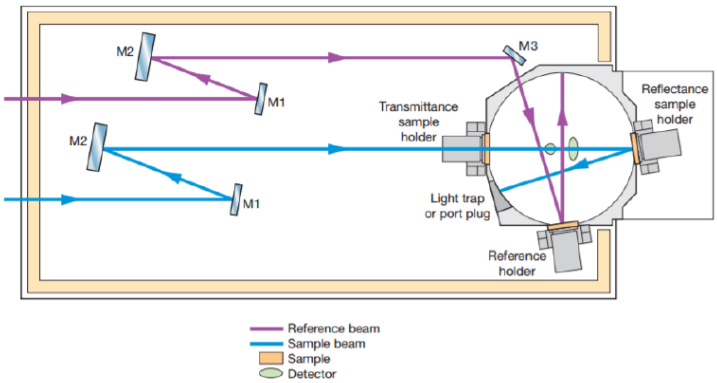

Figure 2.7: View of the intergrating sphere (IS) and optical design of the LAMBDA 950 [79].

The integrating sphere, which is the most important component of the setup, has a diameter of 150 nm and it is coated with a highly reflective material named Spectralon. The sample is placed on the transmittance sample holder, when measuring the intensity of the transmitted light through the sample, or on the reflectance sample holder, when measuring the intensity of the reflected light from the sample. Two optical detectors are used in order to measure the intensity of the reflected light in the integrating sphere and compare it to the reference beam in order to obtain the Reflectance and Transmittance. It has to be noted that there could exist some noise in the measurement in the 860 nm wavelength due to the change from the lead sulfide detector, which measures light intensity above 860nm, to the photomultiplier tube which measures the light intensity below 860 nm.

Finally, the absorption coefficient α can also be obtained indirectly through the equation:

$$\alpha = \frac{-1}{t} \cdot \ln\left(\frac{T}{100 - R}\right) \tag{2.3}$$

Where t is the thickness of the deposited layer and T,R are measured in percentage values.

Dark Conductivity

Dark conductivity measurements were performed in order to obtain the conductivity of the deposited layers as well as the activation energy E_A. For this characterization method, 100 nm (p) poly-SiC_x layers with different R were deposited on quartz glass. Regarding the contacts evaporation of Aluminum was used with a thickness of 400 μm.

The resistance R of the deposited layers determines how easy charge carrier can move through the layer. High values of R lead to a low conductivity of the layer, which could undermine the FF of the final device. The conductivity of the layer can be obtained through the following Equation:

$$\sigma = \frac{1}{R}\frac{d}{t \cdot l} \tag{2.4}$$

Where t is the layer thickness, l is the contact length and d is the gap between the contacts.

The activation energy E_A is a measurement of the energy required for an electron to be excited to a state where it can conduct. Considering that the average energy level of an electron is the Fermi level, the E_A will then be the energy difference between the conduction band E_C and the Fermi level. The conductivity of a material can be obtained through the Arrhenius equation :

$$\sigma = \sigma_o exp\left(\frac{-E_A}{k_B T}\right) \tag{2.5}$$

Where, σ_o represents the material dependent conductivity constant, k_B represents Boltzmann's constant and T the temperature in Kelvin. A higher E_A will lead to a lower conductivity, since a higher amount of energy is required to excite an electron.

For the dark conductivity measurements the applied voltage at the sample was kept at 10 V, while a dark I-V curve was obtained for each temperature between 130 °C and 45 °C with a step of 5°C. Thus, the conductivity and activation energy could be obtained using the aforementioned equations for different temperatures as depicted in Figure 2.8.

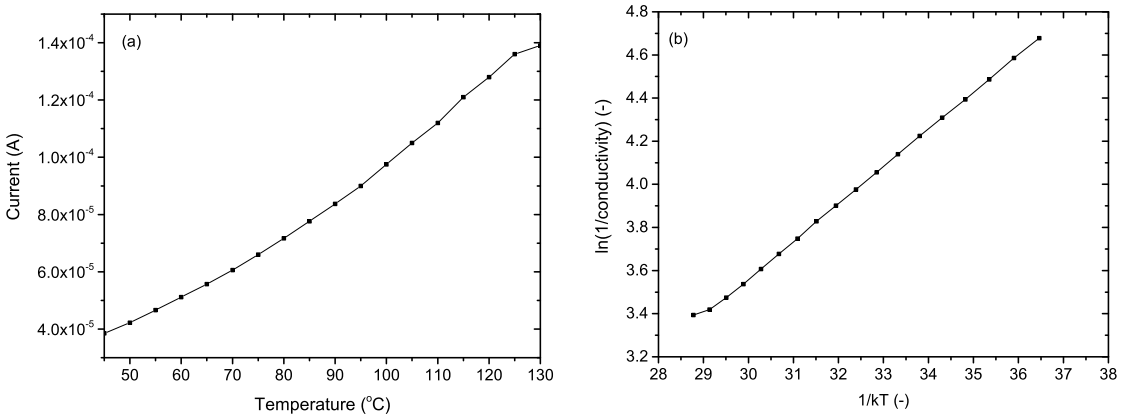

Figure 2.8: Dark I-V curve at 10 V for different T (a) and conductivity for different T (b).

2.2.3 Device Characterization

In this section, the device characterization methods performed on symmetrical samples and solar cells are discussed. When these characterization techniques are performed on symmetrical samples, valuable information can be obtained regarding what is to be expected on a device level. Furthermore, such characterization techniques are also used in order to evaluate the performance of the solar cells' fabricated during this work.

Photoconductance Lifetime Measurement

The effective minority lifetime (τ_{eff}) can provide important information regarding the passivation quality of the wafer. In order to obtain the minority carrier lifetime a photoconductance measurement can be performed using the *Sinton WCT-120 Lifetime Tester*. The Sinton WCT-120 Lifetime Tester setup consists of an eddy-current conductance sensor and a filtered xenon flash lamp [80]. The lamp provides an infrared flash leading to an excess carrier generation of electrons and holes in the wafer, which in turn recombine until an equilibrium is reached. The eddy-current conductance sensor is able to measure the photoconductance as well as a light sensor measures the light intensity provided by the lamp. Since the c-Si wafers used in this work are of excellent quality made through the Float Zone (FZ) process, we ensure that the recombination occurs at the wafer surface and not in the bulk of the material.

Considering an equal carrier generation for holes and electrons the increase in the conductance σ_L can be calculated following Equation 2.6.

$$\sigma_L = q(\Delta n\mu_n + \Delta p\mu_p)W = q\Delta p(\mu_n + \mu_p)W \tag{2.6}$$

Where q represents the elementary charge, Δ_n and Δ_p represent the excess electron and hole carrier density, μ_n and μ_p represent the electron and hole mobility and W represents the wafer thickness [81].

Considering a uniform distribution in the excess carrier and since there is no external electrical field present the continuity equation for an n-type wafer can be obtained :

$$G - \frac{\Delta p}{\tau_{eff}} = \frac{d\Delta p}{dt} \tag{2.7}$$

Where G represents the generation rate of charge carriers.

The effective minority lifetime can then be obtained through Equation 2.8.

$$\tau_{eff} = \frac{\Delta p}{G - \frac{d\Delta p}{dt}} \tag{2.8}$$

The Sinton WTC-120 offers different modes for calculating the minority carrier lifetime. The *quasi-steady-state (QSS)* for minority lifetimes lower than 100 μs and the *transient* mode for minority lifetimes over 100 μs. Conventionally, the representative value for τ_{eff} is extracted at an injection level of 10^{15} cm^{-3}, when the recombination through defects is dominant. For the QSS mode it can be assumed that $\frac{\partial \Delta p}{\partial t} = 0$, while for transient mode it can be assumed that G=0, leading to :

$$\tau_{eff} = \frac{\Delta p}{G} \ (QSS) \qquad \tau_{eff} = -\frac{\Delta p}{\frac{d\Delta p}{dt}} \ (transient) \tag{2.9}$$

In addition to the minority carrier lifetime, the implied open-circuit voltage (iV_{oc}) at an injection level of approximately 1 sun (10^{16} cm^{-3}), resulting from the quasi-Fermi level splitting can be obtained, as well as the dark saturation current J_o. The iV_{oc} can be obtained through Equation 2.10 [81].

$$iV_{oc} = \frac{k_B T}{q} ln(\Delta p) \left(\frac{N_D + \Delta p}{n_i^2} \right) \tag{2.10}$$

Where k_B is the Boltzmann constant, T is the temperature, N_D the donor concentration and n_i the intrinsic carrier concentration. The iV_{oc} measurement does not take into account the metal-silicon recombination losses which are encounter in the subsequent solar cell's fabrication steps, thus it provides an indication of the upper limit for the final solar cell's voltage.

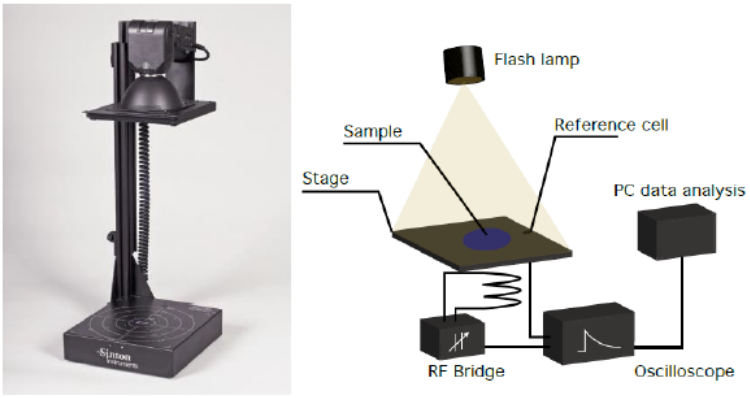

Figure 2.9: Sinton WCT-120 Lifetime tester [82] and Measurement Mechanism of Sinton WCT-120 [77].

Illuminated J-V curve

The most fundamental characterization method to obtain the solar cell's performance is to test the device under standard illumination of 1000 W/m^2 at 25°C. A typical current-voltage (J-V) curve is represented in Figure 2.10. Through this measurement the open-circuit voltage V_{oc}, short-circuit current density J_{sc} and Fill Factor (FF) are obtained, thus the final efficiency of the cell can be measured. These measurements were performed by an AAA class Wacom WXS-156S solar simulator, which emits light with the same characteristics as the light emitted by the sun.

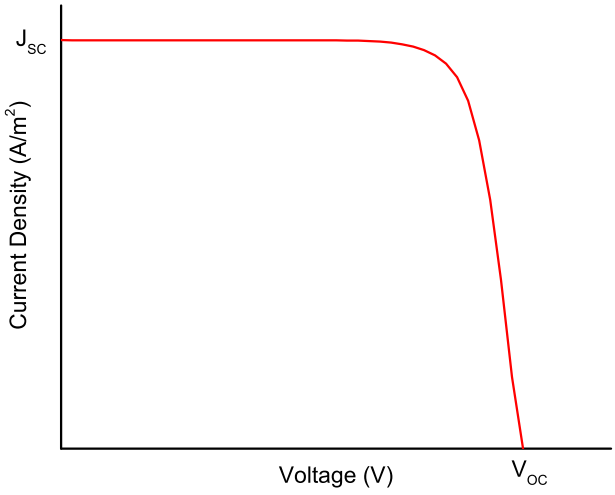

Figure 2.10: Typical current-voltage (J-V) curve of a solar cell.

It has to be noted that two reference solar cells calibrated by Fraunhofer Institute were used as an initial calibration step. Following, the solar cell is measured and the V_{OC}, which can be described by the following equation, is obtained :

$$V_{oc} = \frac{k_B T}{q} ln\left(\frac{J_{ph}}{J_o} + 1\right) \tag{2.11}$$

Where J_{ph} represents the photo-generated current density and J_o represents the saturation current density. As it can be realized from the equation above, a high passivation quality, which in turn means a low saturation current density, will enable high V_{oc} in the final device. Furthermore, the conversion efficiency of the solar cell is extracted through this measurement according to the following equation:

$$\eta = \frac{V_{oc} J_{sc} FF}{P_{in}} \tag{2.12}$$

Where P_{in} is the incident power from the sun simulator and is equal to 1000 W/m^2.

External Quantum Efficiency (EQE)

The External Quantum Efficiency (EQE) is a measurement performed in order to obtain the response of the solar cell at different wavelengths. EQE is defined as the ratio of the number of charge carriers successfully collected to the number of incident photons on the solar cell, and is measured in order to obtain and optical characteristics.

The EQE measurements were performed with an in-house setup which uses a xenon lamp, a Newport illuminator and monochromator, a lock-in amplifier, a chopper and metallic probes. The xenon lamp is able to emit light in a wide range of wavelengths (200-2500 nm), which is then passed through the chopper in order to modulate the intensity and subsequently through the monochromator which ensures a monochromatic light output. The light coming from the monochromator is then focused by lenses on the solar cell surface which is connected to metallic probes in order to obtain the photo-generated current. Finally, the lock-in amplifier is used in order to receive the periodic signal from the chopper and filter out the background noise. Thus, the resulting EQE is also wavelength dependent. The wavelength dependent EQE is defined as :

$$EQE(\lambda) = \frac{I_{ph}(\lambda)}{q\,\Phi_{ph}(\lambda)} \tag{2.13}$$

Where I_{ph} is the photocurrent, q the elementary charge and $\Phi_{ph}(\lambda)$ is the photon flux.

The short-circuit current can then be obtained by integrating over the entire spectrum as shown in Equation 2.14.

$$J_{sc} = q \int_{\lambda_1}^{\lambda_2} EQE(\lambda)\Phi(\lambda) d\lambda \tag{2.14}$$

Another important characterization measurement is the Internal Quantum Efficiency (IQE). The main difference between EQE and IQE is that IQE does not include the optical losses.

Thus, in order to obtain the IQE the number of the absorbed photons rather than the number of the incident photons is taken into account leading to Equation 2.15.

$$IQE(\lambda) = \frac{EQE(\lambda)}{1 - R(\lambda)} \tag{2.15}$$

Where $R(\lambda)$ and $T(\lambda)$ represent the reflectance and transmittance. The reflectance and transmittance can be obtained by other measurements as the one described in Section 2.2.2.

Chapter 3

Material Development of poly-SiC_x layers

In this chapter an investigation on the material properties of the deposited poly-SiC_x layers is performed. In the first part, the experimental details for the deposition of the layers are presented. In the next part, the effect of the carbon content on the material composition is investigated through Raman and Fourier-Transform Infrared Spectroscopy (FTIR) measurements. Following, an investigation is performed on the optical properties of the layers with different carbon contents. Finally, the electrical properties of the poly-SiC_x layers are examined through dark-conductivity measurements, which provide information on the conductivity and activation energy.

3.1 Experimental Details

In this Section the experimental details regarding the deposition of the (p)poly-SiC_x layers are presented. Regarding the substrate material quartz glass is used with a thickness of 500 μm. Firstly, the glass is cleaned in two baths, namely an acetone and an isopropanol bath, for 10 minutes respectively. The next step, is the deposition of the (p)a-SiC_x layer via PECVD, with the gasses used during this deposition being silane (SiH_4), methane (CH_4) and diborane (B_2H_6) diluted 2% in hydrogen. It has to be noted that the total gas flow is kept constant at 68 sccm. At this stage, the gas flow ratio R is defined by the Equation 3.1.

$$R = \frac{CH_4}{CH_4 + SiH_4} \tag{3.1}$$

The carbon incorporated in the deposited layer is related to R. Low gas flow ratios lead to Si-rich layers, while high gas flow ratios lead to more C-rich layers. In this work various gas flows ratios were examined, while the thickness of the deposited layers is kept at approximately 100 nm. The PECVD deposition parameters are summarized in Table 3.1.

Table 3.1: PECVD depostion parameters.

Sample	SiH_4 [sccm]	CH_4 [sccm]	B_2H_6 [sccm]	R [%]	Pressure [mbar]	Power [W]
1	30	35	3	53.8	0.7	3
2	25	40	3	61.5	0.7	3
3	20	45	3	69.2	0.7	3
4	15	50	3	76.9	0.7	3
5	10	55	3	84.6	0.7	3

Following, the samples receive a thermal budget of 850 °C for 5 minutes in order for the layers to crystallize and obtain the final (p)poly-SiC_x layer. Depending on the measurements performed, a hydrogenation step is applied by deposition of SiN_x and a Forming Gas Annealing (FGA) at 400°C for 30 minutes. Finally, depending again on the measurements performed, Al evaporation is used in order to receive metal contacts with a thickness of 400 nm. The flowchart of the fabrication process is illustrated in Figure 3.1.

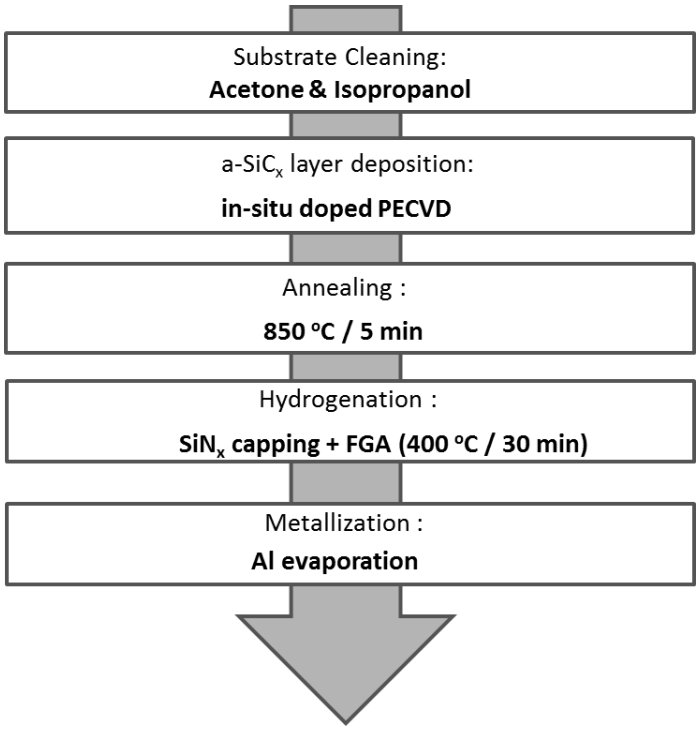

Figure 3.1: Flowchart of the fabrication process on quartz substrate.

3.2 Effect of Carbon Content on the Material Composition

3.2.1 RAMAN Analysis

A microstructural analysis on the deposited layers was performed by means of Raman spectroscopy. The crystallinity fraction of the deposited material was calculated according to the method described earlier in Section 2.2.1. It is to be noted, that the crystallinity fraction is calculated only after the samples have received the thermal treatment and exhibit a crystallization and not in the as-deposited state, where the material remains completely amorphous. The results are illustrated in Figure 3.2, where the intensity has been normalized.

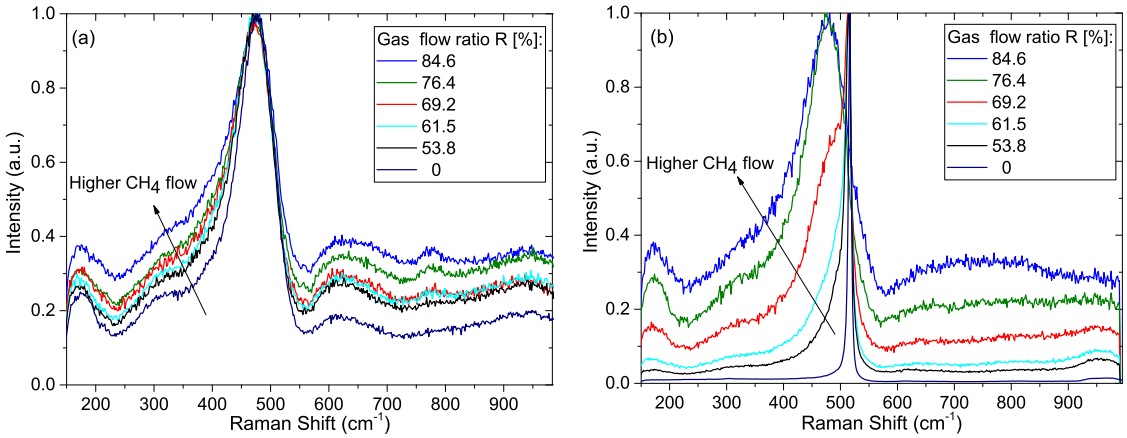

Figure 3.2: Raman spectra of layers with different gas flow ratios (R) deposited on quartz glass measured in the as deposited state (a) and after annealing at 850°C for 5 minutes (b).

As it is expected and clearly visible from Figure 3.2a, the material is in the amorphous state after the PECVD deposition. All of the samples present the characteristic broad peak at 480 cm^{-1}, which corresponds to the transverse optic phonon mode (TO) for a-Si [83]. Furthermore, a peak is observed at 160 cm^{-1}, which also corresponds to a-Si for the transverse acoustic phonon mode (TA)[58]. Furthermore, there can be observed a peak between 770-800cm^{-1} (for $R > 0\%$) which corresponds to TO mode of SiC, although this peak is slight indicating a low overall carbon content in the material, even for the high gas flow ratios [84, 85]. Overall, by incorporating low concentrations of carbon in the material, the characteristic of the silicon network is not changing much, but rather it is only slightly disturbed as it can be seen by a broader TO peak for higher carbon contents.

In Figure 3.2b, the Raman spectra after the thermal treatment are depicted. As it can be observed the CH_4 flow, and consequently the carbon content in the material, can significantly influence the crystallinity of the material. For the samples with R equal to 0%, 53.8% and 61.5% a peak can be observed at 520 cm^{-1} which corresponds to c-Si, indicating a high crystallinity in the material. Following, the sample with R equal to 69.2% exhibits a much broader peak, meaning that this sample only partially crystallizes. Finally, for the

highest CH_4 flows, a broad peak around 480 cm^{-1} is observed, indicating that these samples remain highly amorphous even after the thermal treatment. Overall, it can be said the C incorporation in the deposited layer hinders crystallization. In addition, there cannot be observed any Raman bands between 750 cm^{-1} and 900 cm^{-1}, which bands are linked to the formation of crystalline silicon carbide (c-SiC) [72, 84]. This might indicate the formation of nanocrystalline silicon (nc-Si) grains surrounded by an a-SiC_x tissue [72].

Finally, the crystallinity fraction was calculated only for the samples which exhibit a peak around 520 cm^{-1}, namely the samples with R equal to 0%, 53.8%, 61.5% and 69.2%. The crystallinity fraction was calculated according to the method described in Section 2.2.1 and the results are illustrated in Table 3.2. As expected, the highest crystallinity fraction is observed for the sample with R=0% at 95.7%, while the higher the carbon incorporation in the layer the lower the crystallinity fraction. It has to be noted, that the crystallinity fraction calculated through Equation 2.1, represents the crystallinity of the silicon tissue in the material and not the overall crystallinity of the material, which also incorporates carbon in this work.

Table 3.2: Crystallinity fraction of samples with different gas flow ratios R.

Gas flow ratio (R) [%]	**Crystallinity Fraction** [%]
0	95.7
53.8	71.6
61.5	65.6
69.2	49.2

3.2.2 FTIR Analysis

In order to further investigate the material properties and the bonds present in the deposited layers FTIR measurements were performed. For this characterization n-type CZ silicon wafers were used as the substrate with a thickness of 525 μm, a resistivity of 15 $\Omega - cm$ and $< 100 >$ orientation. Following, a wet-chemically tunnel oxide was grown according to the procedure described in Section 2.1.2 and a PECVD 5 nm (i) a-Si:H interlayer was deposited on top of the chemical oxide. The last deposition consisted of a PECVD 100 nm SiC_x layer. The aforementioned layers were deposited in this order to mimic as close as possible the symmetrical samples which were examined during this work and discussed further in Chapter 4. FTIR measurements were taken at three stages, namely in the as-deposited state, after a thermal treatment at 850 °C for 5 minutes and finally after the hydrogenation process had been applied.

In Figure 3.3, the results are illustrated for the sample with a gas flow ratio R equal to 69.2%. In the as deposited state a peak can be observed around 640-650 cm^{-1}, which corresponds in the Si-H wagging vibration, as well as around 2080-2200 cm^{-1} which corresponds to the Si-H stretching vibration as also observed in other studies [86–88]. Following the

thermal treatment of the sample, Si and nanocrystals of SiC start to crystallize which lead to hydrogen effusion, thus the aforementioned peaks cannot be observed in the annealed state. Furthermore, the absorption band around 780-830 cm^{-1} corresponds to Si-C stretching vibration and as it can be observed it is considerably weaker for the sample in the as deposited state, indicating a lower amount of SiC. This band shifts from 780 cm^{-1} in the as deposited state to 830 cm^{-1} after the thermal treatment has been applied, and such shifts in the SiC band during annealing have also been observed in other studies [87–89]. Finally, a weak signal around 1000 cm^{-1} is observed for the as-deposited sample due to C-H wagging vibrations, indicating that carbon within the SiC film is bonded to H. This peak also disappears during the annealing step due to H effusion.

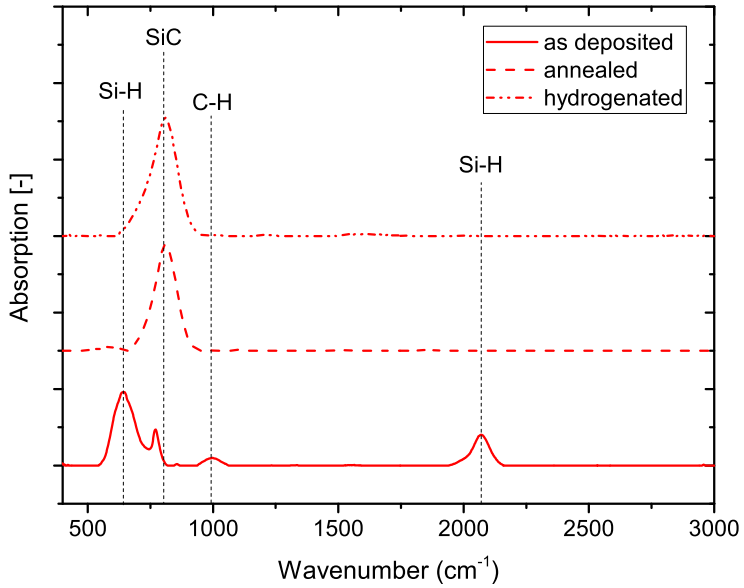

Figure 3.3: FTIR spectra for the sample with R=69.2% in the as-deposited, annealed and hydrogenated state.

In Figure 3.4, the FTIR measurements for samples containing different carbon contents (R=53.8%, 69.2% and 84.6%) are illustrated. As it can be observed in Figure 3.4a, demonstrating the samples in the as-deposited state, a sharper peak for Si-H is present at 640 cm^{-1} and 2100 cm^{-1} for a lower carbon content, indicating that more hydrogen is incorporated in the layer. On the other hand, the peak around 800 cm^{-1}, corresponding to SiC, is sharper for a higher gas flow ratio as expected. Finally, the C-H wagging vibration at 1000 cm^{-1} is not observed for the sample with R=53.8% while the C-H stretching vibration at 2800 and 2900 cm^{-1} is observed only for the sample incorporating the highest carbon content (R=84.6%). regarding the annealed samples depicted in Figure 3.4b, only the SiC peak can be observed at 800 cm^{-1}, with a higher intensity for a higher the gas flow ratio. In addition, the sample with the highest gas flow ratio demonstrates this peak slightly earlier than 800 cm^{-1}, which can be linked to its higher amorphous fraction. As already mentioned, in Figure 3.3 the SiC peak shifts from approximately 780 cm^{-1} in the as deposited state to 830 cm^{-1}

after annealing, thus the sample with the highest carbon content, being highly amorphous, is expected to also demonstrate this peak slightly earlier.

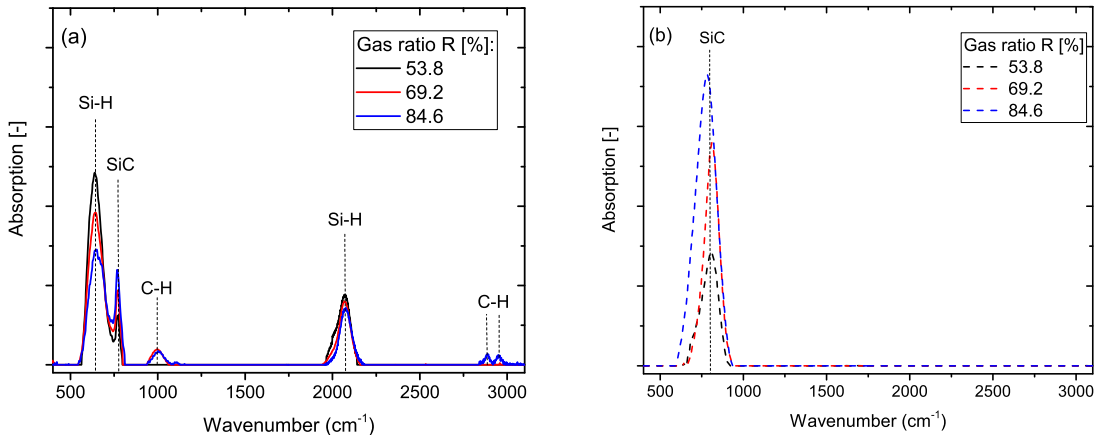

Figure 3.4: FTIR spectra for samples with different R in the as-deposited state (a) and in the annealed state (b).

3.3 Optical Properties of poly-SiC_x layers

The deposited layers were further characterized through reflection and transmission in order to extract the absorption coefficient. Figure 3.5 reports the absorption spectra in the as-deposited and annealed state.

As it can be observed from Figure 3.5a, which represents the samples in the as-deposited state, the absorption coefficient is decreasing by alloying the material with carbon. This can be explained by the fact that incorporating carbon in the deposited layer the bandgap of the material is widened. Interestingly, an inversion of this trend is observed for the annealed samples as illustrated in Figure 3.5b since layers with a higher carbon content demonstrate a higher absorption coefficient. In more detail, as explained in section 3.2.1, the layer is formed by nanocrystalline silicon grains surrounded by an a-SiC_x matrix. Thus, a higher carbon content in the layer leads to a more amorphous layer. It is known that amorphous Si has a higher absorption coefficient compared to crystalline Si and this could explain this inversion.

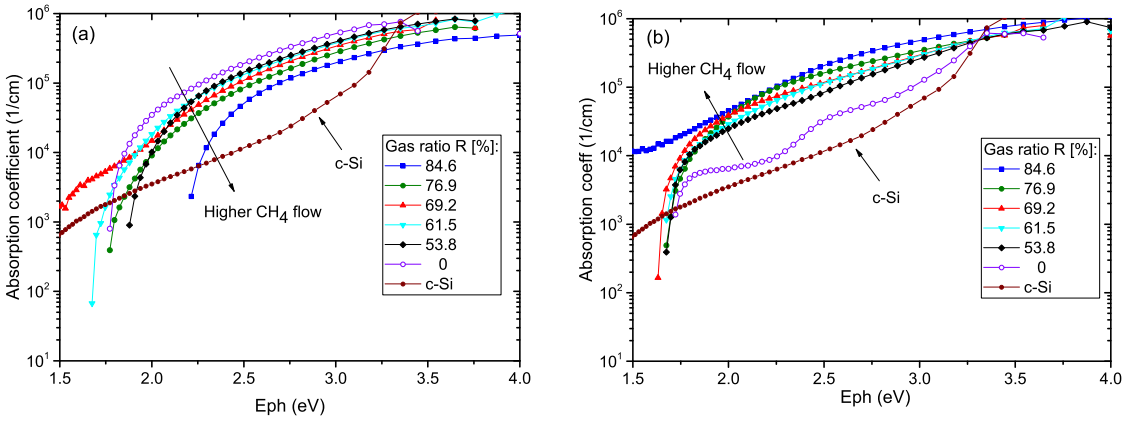

Figure 3.5: Absorption coefficient for samples with different R in the as-deposited (a) and in the annealed state (b).

In addition, the optical bandgap (E_{04}), was extracted for the investigated layers and the results are depicted in Figure 3.6. As it can be seen in the as-deposited state, incorporating carbon in the layer increases the optical bandgap, thus the layer becomes more transparent for higher gas flows ratios. On the other hand, in the annealed state the incorporation of carbon leads to a reduction in the E_{04}, indicating that higher gas flow ratios lead to less transparent layers. Overall, going from the as-deposited state to the annealed state, a reduction in E_{04}, is observed for all gas flow ratios, nevertheless this reduction is more visible for the layer incorporating the highest amount of carbon.

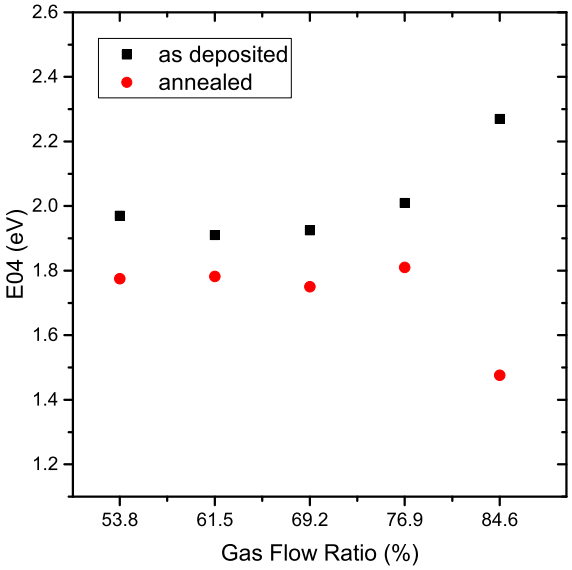

Figure 3.6: E_{04} bandgap of (p)SiC_x layers in the as-deposited and annealed state for various gas flow ratios.

Lastly, in order to further investigate the optical properties of the deposited layers through all the stages of the fabrication process an additional sample with an a-Si:H interlayer of 5 nm and a 100 nm SiC layer (gas flow ratio R equal to 69.2%) was deposited on quartz glass. The layer stack was chosen in order to mimic as close as possible the layer structure implemented on device level in Chapter 5. Reflection and transmission measurements were taken in the as-deposited, annealed and hydrogenated state of the sample. Figure 3.7 shows that the hydrogenation step has no effect on the absorption coefficient since the curves for the annealed and hydrogenated sample are overlapping. In addition, it can be seen that for a photon energy higher than 2.75 eV the sample in the as deposited state has a slightly higher absorption coefficient, while when moving to lower energies than 2.75 eV the annealed/hydrogenated sample absorbs significantly more. This effect can be related to a higher parasitic absorption, which has been similarly observed for poly-Si in other studies [45].

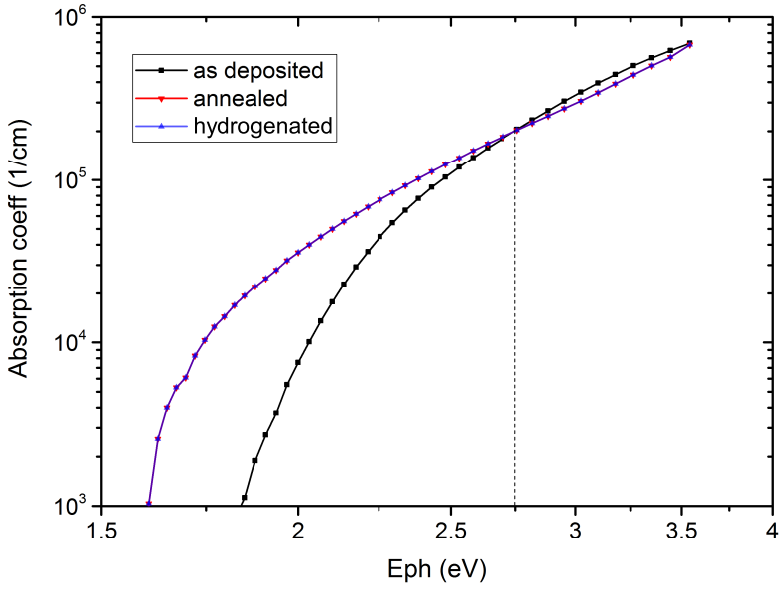

Figure 3.7: Absorption coefficient for the sample with R=69.2% in the as-deposited, annealed and hydrogenated state.

3.4 Electrical Properties of poly-SiC_x layers

In order to evaluate the electrical properties of the deposited layers for different carbon contents dark conductivity measurements were taken according to the method described earlier in Section 2.2.2. The results are depicted in Figure 3.8a representing the samples annealed at 850°C for 5 minutes.

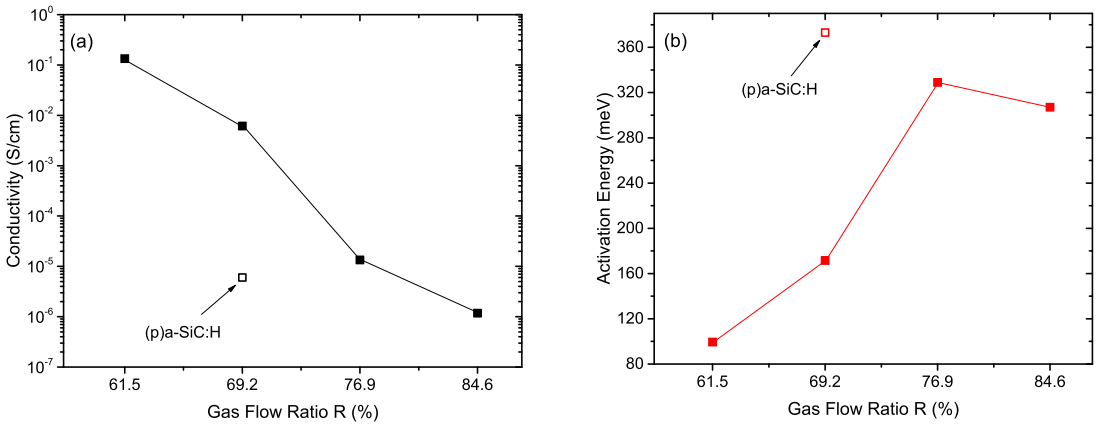

Figure 3.8: Conductivity (a) and activation energy (b) of (p)poly-SiC_x layers after annealing at 850°C for 5min. The open symbols represent the values measured on (p)a-SiC:H layers before annealing [90].

As expected, a higher carbon content hinders the electrical performance of the deposited layer. The sample with the highest carbon content (R=84.6%) exhibits a conductivity in the order of 10^{-6} S/cm, while reducing the carbon content the conductivity increases several orders of magnitude up to 10^{-1} S/cm (R=61.5%). This effect can also be explained by the fact that a higher carbon content leads to a highly amorphous layer, as shown in Section 3.2.1, while lower carbon contents lead to a higher crystallization. It is well-known that crystalline layers exhibit superior electrical properties compared to amorphous layers.

The activation energy, in Figure 3.8b follows an inversed trend compared to conductivity. Higher carbon contents exhibit a higher activation energy (with the only exception for the sample with R equal to 84.6%) with the highest activation energy observed at 329 meV for the sample with R equal to 76.9%. On the other hand, the sample with the lowest carbon content and R equal to 61.5% has the lowest activation energy of 99.5 meV.

Finally, the open symbols represent the conductivity and activation energy for a p-type a-SiC:H layer with a gas flow ratio R equal to 69.2% according to study [90]. As it can be observed the conductivity of the poly-SiC layer is approximately three orders of magnitude higher and accordingly the activation energy approximately 100 meV lower compared to the a-SiC:H layer for the layers with R=69.2%. Interestingly, even the sample incorporating a higher carbon content (R=78.9%) demonstrates a higher conductivity and lower activation energy. This conductivity increment can be attributed to the thermal treatment received. The annealing step transforms the amorphous layer to a polycrystalline one as well as it is responsible for the dopant activation leading to an electrical enhancement.

3.5 Conclusions

In this chapter, the material development was performed. It was shown, through Raman characterization, that incorporating carbon hinders crystallization after annealing and that the resulting layer, following the thermal treatment, is mainly formed by nanocrystalline silicon grains embedded in an a-SiC tissue. Through an FTIR analysis, it was observed that the annealing step leads to hydrogen out-effusion and the formation of SiC. Moreover, it was observed that the higher gas flow ratio, less hydrogen is present in the layer in the as-deposited state, as well as that a higher gas flow ratio leads to a stronger SiC peak. Furthermore, dark conductivity measurements were performed and it was found that the incorporation of higher amounts of carbon leads to lower conductivity (and higher activation energy) values, which can be linked to the amorphous fraction of the material. In addition, comparing a-SiC:H and poly-SiC, the later exhibits much higher conductivity values due to the higher crystallization and dopant activation achieved following the thermal treatment. Regarding the optical characterization it was found that alloying with carbon can decrease the absorption coefficient in the as-deposited state due to bandgap widening. On the other hand, following the thermal treatment it was found that higher carbon contents lead to a higher absorption coefficient, which can be linked to the higher amorphous fraction of the layer for a higher carbon content. Finally, it was also observed that hydrogenation has no effect on the absorption coefficient of the deposited layers.

Chapter 4

Passivation optimization of the SiO_x/poly-SiC_x passivating contact

In this chapter the experimental results regarding the optimization on the passivation qualty of SiO_x/(p)poly-SiC_x layers are presented and discussed. In the first part, the experimental details which were followed for the fabrication of the symmetrical samples are presented. Following, the experiments performed focus on optimizing both the gas flow ratio and high-temperature annealing parameters in order to maximize the passivation quality. Furthermore, two different deposition methods, namely PECVD and LPCVD, are investigated for the a-Si:H interlayer deposition. Finally, in order to further enhance the passivation quality, an optimization on the hydrogenation process is performed for both (p) and (n)poly-SiC_x symmetrical samples, by depositing different capping layers and performing FGA at various temperatures and durations.

4.1 Experimental details

In this Section the experimental details regarding the fabrication of (p)poly-SiC_x symmetrical samples are given. A schematic of the deposited layers is given in Figure 4.1, in order to better visualize the fabrication process of the symmetrical samples.

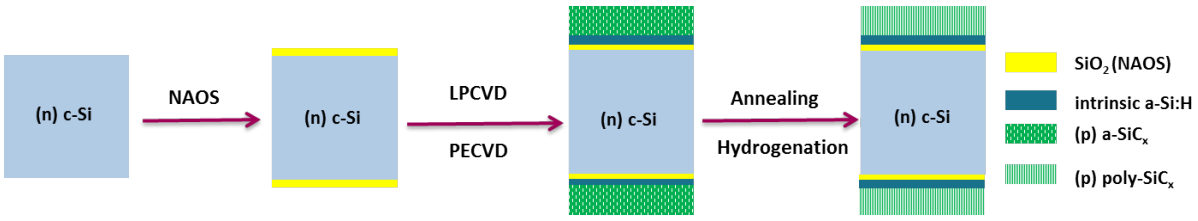

Figure 4.1: Schematic sketch of (p)poly-SiC_x symmetrical samples fabricated for passivation quality optimization.

Regarding the bulk material, n-type Float-Zone (FZ) wafers are used. These wafers are double side polished with a thickness of 280μm and an $< 100 >$ orientation. The wafers are cleaned using HNO_3 baths in order to remove organic and inorganic contaminants [64] and following the native oxide is removed by dipping the wafers in a 0.55% hydrofluoric acid solution for a few minutes. In the next step, the tunnel oxide layer is grown wet-chemically by immersing the wafer in an 69.5% nitric acid solution (NAOS) for 1 hour at room temperature. The next step is the deposition of the a-Si:H interlayer at different thicknesses, in either an RF-PECVD chamber or an LPCVD furnace. Furthermore, RF-PECVD is used for the deposition of the (p)a-SiC_x layer. Note that the doping gas used is diborane (B_2H_6), which is diluted 2% in hydrogen , while the CH_4 and SiH_4 gas flows are varied, realizing different carbon contents as mentioned in Table 3.1 (Section 3.1). Following, a high temperature annealing step is performed at different temperatures (825°C - 875°C) and durations (0 and 5 minutes) in order to activate and drive in the dopants as well as to crystallize the a-SiC_x and obtain the (p)poly-SiC_x layer. Next, a hydrogenation step is performed using different capping layers (AlO_x, SiN_x and (AlO_x/SiN_x) and followed by Forming Gas Annealing (FGA) at different temperatures (400°C and 500 °C) and durations (30 and 60 minutes), in order to further improve the chemical passivation of the samples. Finally, the capping layer mentioned for the hydrogenation process is etched in a BHF (Buffered Hydrofluoric Acid) solution, obtaining the final (p)poly-SiC_x symmetrical sample.

4.2 Passivation Results on Symmetrical Samples Fabricated by PECVD

In this section, the passivation optimization of symmetrical (p)poly-SiC_x samples is investigated. During this optimization procedure the effect of PECVD parameters is examined for both the intrinsic a-Si:H interlayer and the doped layers. Figure 4.1 illustrates the symmetrical samples fabricated, which include the silicon oxide and an (i)a-Si:H interlayer of variable thickness (the need for the a-Si:H interlayer is explained in Section 4.5) capped with a 30 nm thick (p)SiC_x layer, which after the thermal treatment crystallizes giving the (p) poly-SiC_x.

Various parameters during the fabrication process are investigated in order to achieve the best possible results. In the first step, the gas composition used during the PECVD process is varied (Section 4.2.1) followed by an investigation of the optimal annealing temperature and duration (Section 4.2.2) and finally a hydrogenation step is performed in order to further enhance the passivation properties of the samples (Section 4.2.3). After the layer growth and between each fabrication step lifetime measurements are taken to control the passivation quality.

4.2.1 Effect of Gas Flow Ratio

The first parameter examined is the gas composition during the PECVD deposition. It has to be noted that for these symmetrical samples the (i)a-Si:H interlayer is kept constant at

5 nm, while the a-SiC_x layer thickness is kept constant at 30 nm.

Going into more details regarding the PECVD deposition parameters, a total gas flow of 68 sccm is always used and the diborane (B_2H_6) flow which is used for the doping is kept constant at 3 sccm. Consequently, by changing only the gas flow ratio R, the carbon content of the deposited layer can be adjusted. Various gas flow ratios were examined in this part of the experiment from 0%, resulting into a-Si layer, up to 84.6%, resulting into a-SiC_x layer. The carbon content in the deposited layer can have a significant effect of both the electrical and optical properties of the SiC_x layer as discussed in Chapter 3, thus this optimization step is crucial.

The implied V_{oc} of the symmetrcical samples, with a structure as shown earlier in Figure 4.1, was evaluated by means of the QSS (Quasi-Steady-State) photoconductance technique. The results are depicted in Figure 4.2 in the *as-deposited* state, meaning that the deposited layers are amorphous.

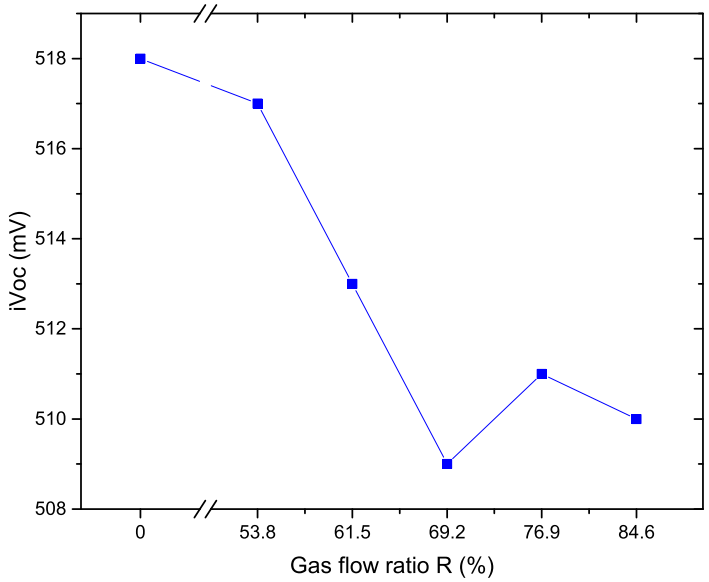

Figure 4.2: iVoc of symmetrical (p)SiC_x samples for various R in the as-deposited state.

As illustrated in Figure 4.2, it can be observed that the highest passivation quality is reached for the sample with a gas flow ratio of 0%, meaning that there is no carbon present in the layer. This symmetrical sample with a (p)a-Si:H layer achieves an iVoc of 518 mV. On the other hand, the lowest passivation quality is realized for the sample with the highest carbon content at 510 mV (if the sample with a gas flow ratio of 69.2% is excluded). There is a clear trend showing that increasing the CH_4 flow, which translates into adding more carbon to the deposited layer, the passivation properties deteriorate. The only exception from this trend is the sample with a gas flow ratio of 69.2%, which exhibits the lowest iV_{oc} compared to the other samples. This could be possibly explained by process related

inaccuracies during the PECVD deposition, which is a rather sensitive process.

As it has been demonstrated from the experiments carried out, increasing the gas flow ratio R leads to a degradation of the passivation quality. This could be attributed to the increased mid-gap defect density in the layers which incorporate higher amounts of carbon, resulting in a lower quality passivation [58, 72]. Furthermore, a higher incorporation of carbon leads to a lower conductivity which could also explain the lower passivation quality.

4.2.2 Effect of Annealing Temperature and Duration

The next step in the fabrication of symmetrical samples is the annealing process. As it has already been discussed in Chapter 2, the optimization of the annealing step is crucial for the passivation quality of the samples. In fact, the annealing step is responsible for the crystallization of the deposited amorphous layers leading to the final poly-SiC_x layer. Furthermore, during the thermal treatment the activation of dopants takes place as well as the dopants diffuse in the c-Si wafer. It has to be noted that a long annealing duration and high annealing temperature could cause an excessive diffusion of the dopants in c-Si leading to a degraded band-banding or even to local break-ups in the tunelling oxide affecting the chemical passivation [40, 62, 71].

Taking into account the importance of the annealing process, the annealing duration and temperature was varied in a series of experiments in order to obtain the optimum combination of temperature and duration for all the gas flow ratios R examined. In more detail, the symmetrical samples were annealed at the following combinations of temperature and duration, as shown in Table 4.1.

Table 4.1: Annealing Temperature and Duration combinations investigated.

Temperature [°C]	**Duration [minutes]**
825	5
850	0
850	5
875	5

The iV_{oc} measured after annealing is depicted in Figure 4.3. As it can be observed the samples with different gas flow ratios R behave differently for the different annealing temperatures and durations. Overall, a clear trend cannot be extracted looking at the results of the annealing experiment, although observations can be made.

The sample with a gas flow ratio R equal to zero, meaning that no carbon is present in the layer, exhibits the highest iV_{oc} and stability through the various annealing temperatures and durations. This sample achieves an iV_{oc} in the range of 633-653 mV, τ_{eff} lies in the range of 203-456 μs and J_o values in the range 106-188 fA/cm^2. Note that the best results

are realized for the annealing temperature of 850 °C and duration of 0 mins. Increasing the gas flow ratio R seems to undermine the passivation quality, as also observed in the as-deposited state (Section 4.2.1). Once again, the sample with the highest gas flow R of 84.6% shows deteriorated performance with an iV_{oc} as low as 536 mV and τ_{eff} of 10 μs (for the annealing temperature of 850°C and duration of 5mins). Interestingly, the aforementioned sample seems to gain an impressive boost of 88 mV in iVoc after being annealed at 875 °C for 5 mins, resulting in a minority carrier lifetime τ_{eff} of 151 μs and a J_o value of 250 fA/cm^2. This observation could be possibly attributed to the higher crystallization of this sample. As shown earlier in Section 2.5, the deposited SiC_x layer remains highly amorphous when annealed at 850 °C for 5min, thus annealing at a higher temperature such as 875 °C could lead to a higher crystallinity, offering superior electrical properties.

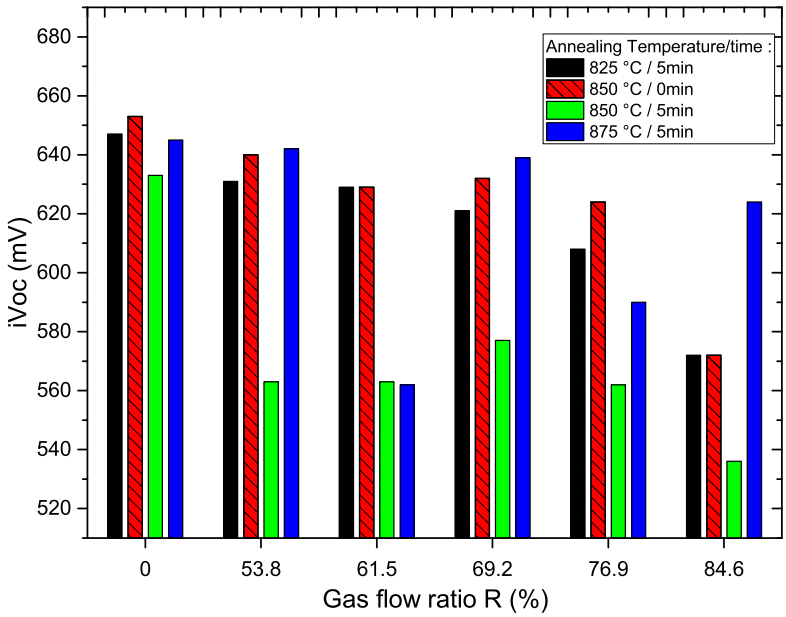

Figure 4.3: iV_{oc} of (p)poly-SiC_x symmetrical samples for various R and annealing temperature/duration combinations. Dashed bars refer to an annealing duration of 0 mins, filled bars refer to an annealing time of 5mins.

Looking at the results it can be said that generally the lower annealing temperature and time combination (825°C/5 min and 850°C/0 mins) seems to be yielding a better passsivation quality for most of the samples, with the exception of the sample with the highest carbon content in which the highest temperature examined of 875 °C seems to be the optimum. In general, increasing the carbon content in the deposited layer the passivation quality decreases. This can be due to the increased defect density as also mentioned in the previous section but also due to the lower crystallinity fraction, confirmed by the structural characterization. As shown in Section 3.2.1, the samples with higher carbon content exhibit a lower crystallinity fraction after the annealing step. For the samples with a higher crystallinity fraction, the grain boundaries can act as diffusivity chanels through which the dopants can reach the c-Si bulk [72]. As a consequence, deeper in-diffused regions in the

surface of c-Si bulk can be expected for the samples with higher crystallinity and minority carriers in the bulk benefit from this in-diffused region. It can also be clearly observed that for all samples the combination of annealing temperature at 850°C and 5 mins yields the worst performance, however an annealing step at 875°C for 5 mins can improve the iV_{oc} again.

4.2.3 Hydrogenation

Following the series of experiments, the hydrogenation step is applied. Hydrogenation is a crucial process for the fabrication of high-efficiency solar cells. This process is applied in order to passivate the electronic defects present in the material and as a consequence increase the minority lifetime. In this part of the experiment, hydrogenation was performed by depositing a 100 nm thich SiN_x capping layer through PECVD. This capping layer acts as an H donor layer. Following, a FGA is performed for 30 minutes at a temperature of 400°C. This FGA step is responsible for providing additional H during the annealing procedure as well as for the release of H which is already incorporated in the previously deposited SiN_x layer, enabling it to diffuse to the SiO_x/Si interface, passivating defects. Finally, the SiN_x layer is etched in a BHF solution. The removal of the SiN_x layer had almost no effect on the iV_{oc} of the samples, implying that the SiO_x/Si interface remains well passivated even after the etching.

In Figure 4.4, the passivation results after the hydrogenation step are depicted. It is clear that a significant boost in the iVoc of the samples is achieved after this process. This strong boost in iV_{oc} after the hydrogenation process could be explained by the fact that the overall surface passivation is strongly driven by the chemical passivation of the samples [72]. It was observed in Section 3.2.2 that hydrogen effuses out of the layer during the thermal treatment, thus the hydrogenation step can provide additional hydrogen in order to passivate the dangling bonds. Overall, the hydrogenation step seems to saturate any differences in iV_{oc} observed after the annealing step (Figure 4.3), making all samples more comparable. Furthermore, following the hydrogenation step the samples annealed at combinations of lower temperatures and durations exhibit the best results, which could be attributed to the further thermal treatment of these samples during FGA.

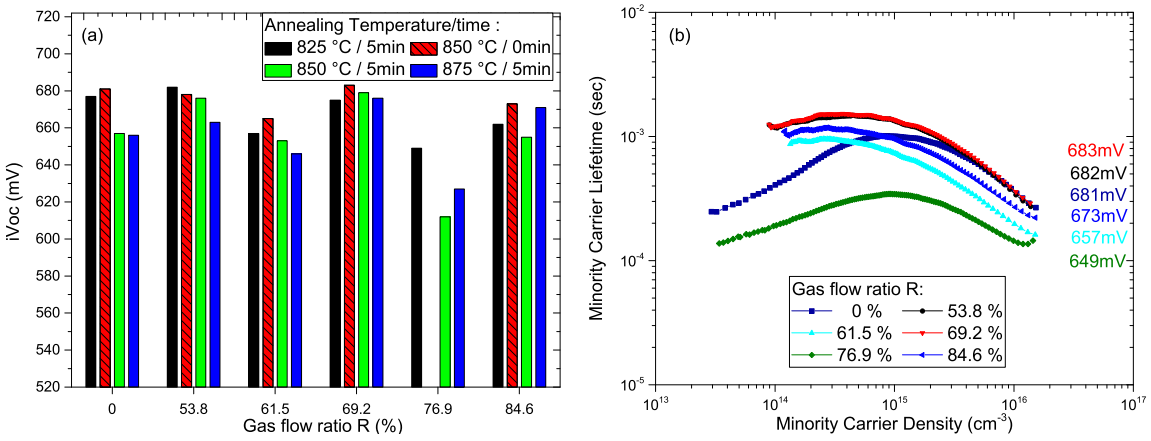

Figure 4.4: iV_{oc} of (p)poly-SiC_x symmetrical samples after hydrogenation for various annealing combinations (a) and lifetime after hydrogenation (in the best annealing condition from a) (b).

Since the hydrogenation step has been completed, the final iV_{oc} for the samples can be assesed and extract the optimal combination of gas flow ratio R and annealing combination. The samples with an R equal to 53.8% and 69.2% demonstrate the highest passivation quality. The sample with R=53.8% demonstrates an iV_{oc} of 682 mV, a τ_{eff} of 1.3 ms and a J_o of 37 fA/cm^2. The sample with R=69.2% exhibits a slightly higher iVoc of iV_{oc}, t_{eff} of 1.3 ms and J_o of 38 fA/cm^2. In the next Section the sample with R=69.2%, which demonstrated the best passivation quality, is chosen for further optimization.

4.2.4 Effect of a-Si:H interlayer thickness

In the final step of the experiment, a variation in the intrinsic a-Si:H interlayer thickness was performed. The thickness of the (i)a-Si:H interlayer thickness was varied in the range of 0-16 nm. In addition, a (p) doped a-Si:H interlayer with a thickness of 5 nm was examined in order to determine whether an already doped interlayer could possibly improve the field effect passivation. It has to be noted that at this stage the a-Si:H interlayer is deposited by means of PECVD and R is kept at 69.2%.

The need for the a-Si:H has been demonstrated by other groups [59, 60]. They demonstrate that C atoms react with the SiO_x, hindering the chemical passivation. Going deeper into this, carbon atoms are deposited as CH_3 groups, which are poorly connected to the a-Si network. The reason behind the poorly connection mentioned between C and the a-Si network, is the fact that only one bond exists between C atoms and a-Si. During the annealing process hydrogen can effuse, leading to dehydrogenated C atoms bonded only to one Si atom. Consequently, C atoms can possibly react with the SiO_x layer, leading to oxygen effusion in the forms of CO and CO_2 . In order to avoid the immediate contact of the carbon with the SiO_x layer and mitigate the aforementioned chemical reaction, the a-Si:H interlayer is incorporated between the SiC_x layer and the SiO_x.

In Figure 4.5a the iV_{oc} obtained in the annealed state for different interlayer thicknesses is depicted. As it can be observed, all samples are quite stable for the different annealing temperatures and durations. From the annealing step already the need for an interlayer can be realized. The sample without an interlayer demonstrates significantly lower passivation properties compared to all the other samples, something which can be explained as already mentioned by the chemical reaction of carbon atoms with the silicon oxide, hindering chemical passivation.

Looking at the different interlayer thicknesses after the hydrogenation step has been applied in Figure 4.5b, the sample without an a-Si:H interlayer demonstrates the lowest performance, with its highest iV_{oc} being 558 mV and τ_{eff} at 10.6 μs (875°C/5mins). This result validates the need of an a-Si:H interlayer, in order to mitigate the reaction between C atoms and the SiO_x. Following, by increasing the interlayer thickness to 5 nm a significant boost in iV_{oc} can be obtained with an iV_{oc} of 683 mV (850°C/0mins). On the other hand, the sample with the (p)a-Si:H interlayer of 5 nm demonstrates a significantly lower iV_{oc} of 587 mV, which could be attributed to the fact that dopants are deposited closer to the c-Si bulk and an higher diffusion into the c-Si bulk can be realized, hindering the field-effect passivation. Following, an even thickner layer of 8 nm demonstrates the best passivation quality boosting iV_{oc} to 684 mV realizing a τ_{eff} at 1456 μs (850°C/5mins). The thicker interlayers of 10 nm and 16 nm start to hinder the passivation quality leading to lower iV_{oc} of 670 mV and 666 mV respectively. This could be attributed to the fact that such thick layers do not allow the efficient diffusion of dopants leading to a deteriorated field effect passivation.

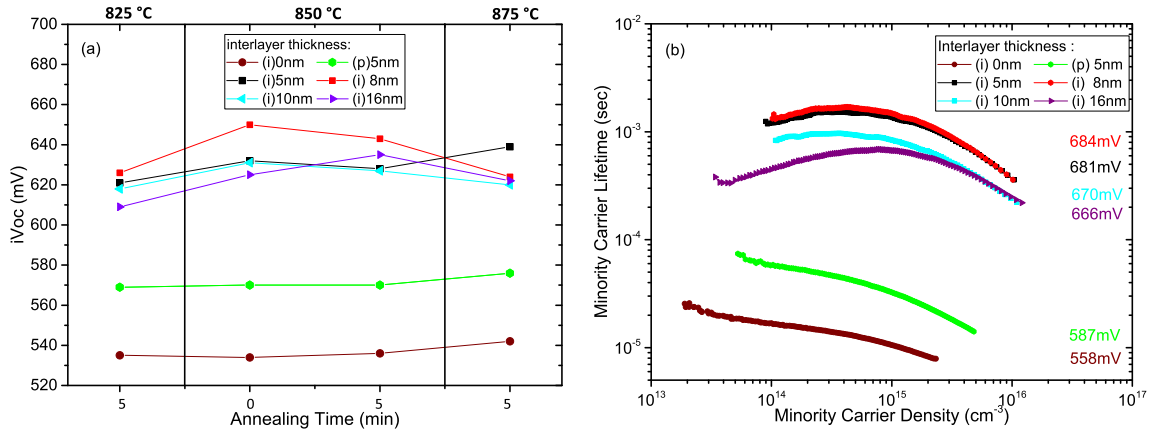

Figure 4.5: iV_{oc} of (p)poly-SiC_x symmetrical samples with variable a-Si:H interlayer thickness in the annealed state (a) and lifetime of (p)poly-SiC_x symmetrical samples with variable a-Si:H interlayer thickness in the hydrogenated state (b).

To sum up, it was shown that for (p)poly-SiC_x symmetrical samples fabricated through PECVD a great thermal stability can be achieved, offering a wide window of thermal budgets in which such layers can be fabricated for a later solar cell application. Furthermore, the

application of a SiN_x capping layer before the FGA step was shown to greatly improve the passivation quality for all samples, implying that the passivation is chemically driven. Overall, the sample which achieved the highest passivation quality is the sample which incorporates an intrinsic a-Si:H interlayer of 8 nm and was fabricated with a gas flow ratio R of 69.2%. This champion sample achieved an iV_{oc} of 684 mV, an τ_{eff} of 1.4 ms and a J_o of 34.7 fA/cm^2 at an annealing temperature of 850°C for 0 minutes.

4.3 Passivation Results on Symmetrical Samples Fabricated by LPCVD & PECVD

In this section, the passivation optimization of (p)poly-SiC_x symmetrical samples is further investigated. The same symmetrical samples, as examined in the previous Section 4.2, are examined with the only difference being the a-Si:H interlayer deposition method, which is performed by LPCVD. The motivation behind this, is the lower hydrogen content as well as the higher homogeneity and density of the layers deposited by LPCVD compared to PECVD [42], which in turn can affect the passivation quality. For this series of experiments three gas flow ratios R were chosen, namely 53.8%, 69.2% and 84.6%. The samples with R equal to 53.8% and 69.2% demonstrated the best passivation results in Section 4.2, thus they are chosen and the extreme case with the sample incorporating the highest carbon content and R=84.6% is also examined.

4.3.1 Effect of Annealing Temperature and Duration

In the first step of this series of experiments, a variation in the gas flow ratio R was performed, with the (i)a-Si:H layer thickness being equal to 7 nm and the same deposition parameters being used for the PECVD a-SiC_x deposition, as mentioned in Section 4.2.

The (p)a-SiC_x symmetrical samples were annealed at various combinations of temperature and duration, the same as mentioned earlier in Table 4.1, in order to activate and drive in the dopants as well as for the crystallization the deposited layer, leading to a (p)poly-SiC_x layer. The results after the annealing step are depicted in Figure 4.6. As it can be observed, for the LPCVD deposited (i)a-Si:H interlayer a higher annealing temperature and duration can be beneficial. This could be explained by the fact that the LPCVD interlayer is of high homogeneity and density, thus a longer annealing temperature and duration are needed for the dopants to diffuse effectively through the layer and achieve a sufficient band bending, leading to a high carrier selectivity. The samples, with a gas flow ratio R of 53.8% and 69.2% exhibit a considerably higher passivation quality compared to the sample with R equal to 84.6%, as also observed in Section 4.2, where it was mentioned that higher carbon contents can potentially increase the defect density and reduce the crystallinity fraction, thus resulting in a lower passivation quality. Furthermore, the aforementioned symmetrical samples showed a greater stability for different annealing conditions compared to the sample with R equal to 84.6%.

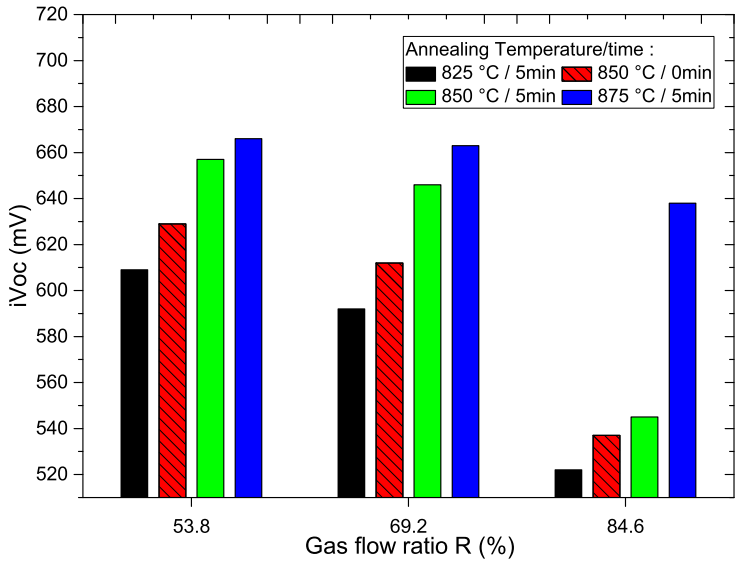

Figure 4.6: iVoc of (p) SiC_x symmetrical samples after annealing.

As it can be already observed from the annealing step, incorporating an LPCVD deposited a-Si:H interlayer seems to be beneficial. The highest iV_{oc} for the samples examined are 666 mV, 663 mV and 63 8mV for an R=53.8%, 69.2% and 84.6% respectively. These values are already considerably higher than the values obtained for an PECVD interlayer.

4.3.2 Hydrogenation

Next, hydrogenation is performed on the symmetrical samples in order to passivate the electronic defects. As mentioned in Section 4.2, a 100 nm thick SiN_x capping layer is deposited by means of PECVD followed by a FGA at 400°C for 30 minutes.

In Figure 4.7, the results after hydrogenation has been applied are illustrated. As it can be observed, the best performing sample is the one with R equal to 69.2%, which achieves an iVoc of 700 mV, τ_{eff} of 1.8 ms and J_o of 13.2 fA/cm^2, followed by the sample with R equal to 53.8% and last the sample with R equal to 84.6%. It can be observed that increasing the gas flow ratio R from 53.8% to 69.2% can boost the passivation properties of the sample, but on the other hand further increasing the gas flow ratio to 84.6% leads to a significant drop on the minority carrier lifetime.

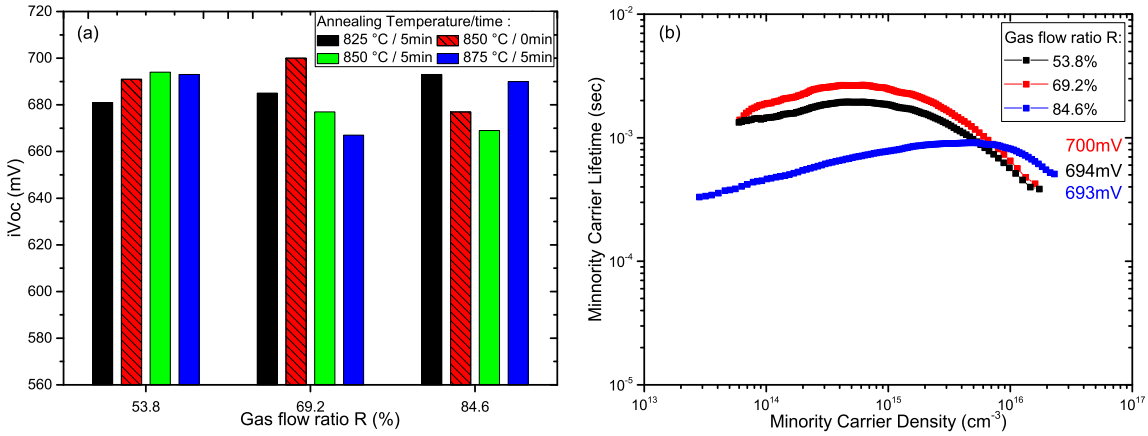

Figure 4.7: iV_{oc} of (p)poly-SiC_x in hydrogenated state at various annealing combinations (a) and lifetime in hydrogenated state (in the best annealing condition from a) (b).

Again, as in Section 4.2, the hydrogenation step significantly benefits the passivation quality, implying that chemical passivation drives the overall surface passivation of the samples. Furthermore, the lifetime curves can provide information regarding the sample's passivation mechanism, namely field effect or chemical. The region with a low carrier density (below 10^{15}) can be linked to field effect passivation while higher injection levels can be associated with chemical passivation [59]. As it can be seen in Figure 4.7b, all samples prepared demonstrate a tailing at low injection levels, implying that field effect passivation is not optimal.

4.3.3 Effect of a-Si:H interlayer thickness

As for the samples examined in Section 4.2.4, a variation step on the LPCVD deposited (i)a-Si:H interlayer thickness is applied. In this part of the experiment, three different thickness layers were tested, namely 3 nm, 7 nm and 12 nm. The iV_{oc} results are depicted in Figure 4.8a. As it can be observed, the thicker the interlayer the better passivation can be achieved. The best passivation result for the 3 nm interlayer is an iV_{oc} of 688 mV, τ_{eff} of 1.81 ms and Jo of 28.9 fA/cm^{-1} (875°C/5mins), while for the 7 nm interlayer an iV_{oc} of 700 mV and τ_{eff} of 1.8 ms and Jo of 13.2 fA/cm^{-1} (850°C/0 mins) is achieved. The best performing interlayer of 12 nm exhibits an iV_{oc} of 706 mV a τ_{eff} of 2.26 ms and Jo of 12.7 fA/cm^{-1}(850°C/0 mins). In Figure 4.8b the lifetime is depicted in the hydrogenated state and at the best annealing condition. It can be seen, that a thicker interlayer provides a higher minority lifetime, expecially in the region of the chemical passivation.

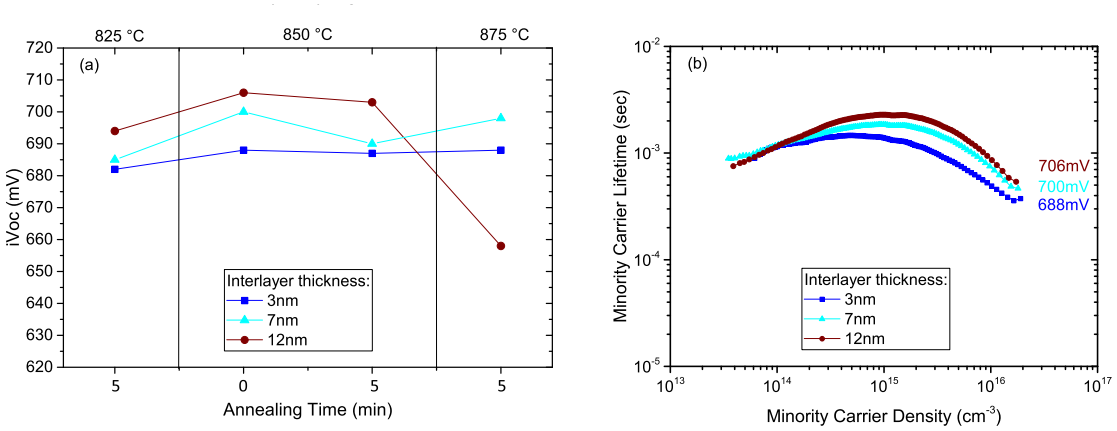

Figure 4.8: iV_{oc} of (p)poly-SiC_x symmetrical samples with variable a-Si:H interlayer thickness in the hydrogenated state at various annealing combinations (a) and lifetime of (p)poly-SiC_x symmetrical samples with variable a-Si:H interlayer thickness in the hydrogenated state (in the best annealing condition from a) (b).

4.4 Comparison of LPCVD and PECVD Deposition Methods

In order to better understand the difference between the LPCVD and PECVD deposited (i)a-Si:H interlayer, a comparison is reported in Figure 4.9. The highest iV_{oc} achieved for the different interlayer thicknesses and depositions methods examined is illustrated. As it can be observed, the sample with no interlayer demonstrates a significantly lower passivation quality validating the need for an interlayer in order to mitigate the reaction of carbon atoms with the SiO_x, as mentioned earlier. Regarding, the PECVD deposited interlayer the optimal interlayer thickness is at 8 nm with an iV_{OC} of 684 mV, while thicker layers lead to deteriorated passivation quality. On the other hand, regarding the LPCVD deposited interlayer the thickest layer of 12 nm demonstrates the optimal results with an iV_{OC} of 706 mV. As it is obvious, the LPCVD interlayer significnatly outperforms the PECVD interlayer and this could be attributed to the higher homogeneity and density of the LPCVD interlayer, which consequently leads to an enhanced passivation.

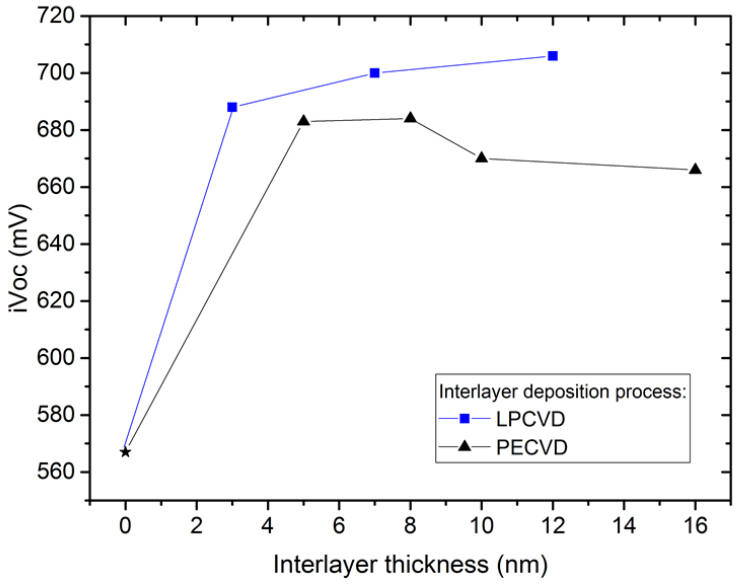

Figure 4.9: iV_{oc} of LPCVD and PECVD deposition methods for the a-Si:H interlayer.

4.5 Optimization of Hydrogenation Using Different Capping Layers

Since all other parameters, regarding the optimum deposition parameters for passivation have been defined in the previous sections, an optimization on the hydrogenation process is performed. Hydrogenation is crucial since through this process the electronic defects present in the material can be passivated with H atoms. As a consequence, the chemical passivation of the fabricated samples in enhanced leading to a higher iV_{oc} and minority carrier lifetime.

In previous sections, hydrogenation was performed using a PECVD deposited SiN_x capping layer of 100 nm, which acted as a hydrogen donor, passivating the dangling bonds present in the material. Following, a Forming Gas Annealing (FGA) at a temperature of 400°C for 30 minutes was performed in order to further enhance the passivation quality. In this section different capping layers are used, namely AlO_x (by ALD) and also combinations of AlO_x and SiN_x [73, 86, 91]. Furthermore, different FGA temperatures and durations are examined for the optimum capping layer.

Furthermore it has to be noted, that the hydrogenation optimization was not only performed on (p) but also on (n)poly-SiC_x symmetrical samples. The (n) doped symmetrical samples had the same deposited layers as the (p) ones discussed so far, with the only difference being on the doping gas used, namely PH_3, realizing an (n) poly-SiC_x layer after annealing. For the (n)poly-SiC_x layer, an optimization on deposition parameters had been performed by other members of the PVMD group [92]. Different FGA annealing temper-

atures and capping layers were tested for the aforementioned samples in order to optimize the hydrogenation process.

In Figure 4.10 a schematic sketch is given in order to better visualize the symmetrical samples fabricated for the hydrogenation optimization. It is to be noted, that this schematic sketch illustrates only (p)poly-SiC_x symmetrical samples fabricated but also similarly (n)poly-SiC_x samples were fabricated.

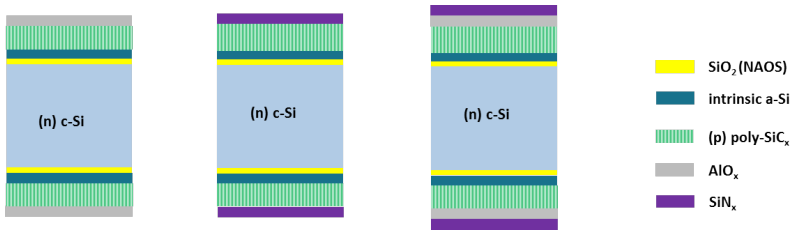

Figure 4.10: Schematic sketch of (p)poly-SiC_x symmetrical samples with different sacrificial capping layers investigated.

4.5.1 Aluminum Oxide as Capping Layer

The first capping layer to be examined is Aluminum Oxide (AlO_x) that is used for hydrogenation of poly-Si [73, 91] due to its high H content. Following, H atoms can migrate from the deposited AlO_x towards the interface which in turn passivate dangling bonds present in the layers, leading to an enhanced chemical passivation [91].

For this part of the experiment three different AlO_x thicknesses were examined, namely 3 nm, 7 nm and 10 nm all followed by a FGA at 400 °C for 30 minutes. The results are depicted in Figure 4.11. As expected, depositing an AlO_x layer, an increasing passivation quality can be realized when compared to the sample just after annealing, especially in minority carrier densities over 10^{15} cm^{-3}, enchancing chemical passivation. The thinnest AlO_x layer seems to only slightly outperform the thicker layers, implying that 3 nm of AlO_x is already sufficient for the passivation. Especially, in the chemical passivation region (minority carrier density over 10^{15} cm^{-3}) the iV_{oc} is independent of the AlO_x thickness. It has to be noted though, that the iV_{oc} of 676 mV observed is considerably lower compared to the results depicted in earlier Sections, when the passivation was performed with a SiN_x capping layer.

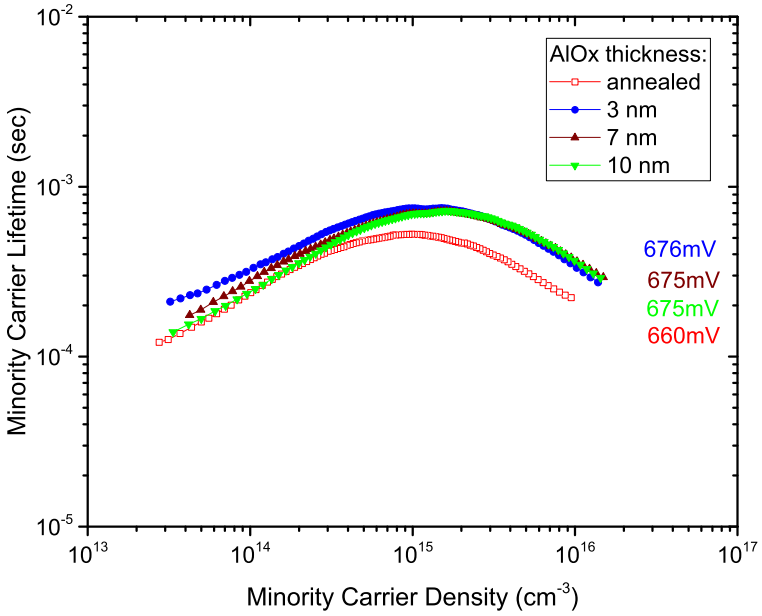

Figure 4.11: Lifetime of hydrogenated (p)poly-SiC_x symmetrical samples with different AlO_x capping layer thicknesses.

4.5.2 Aluminum Oxide & Silicon Nitride as Capping Layer

In the next step a double capping layer, namely AlO_x capped with SiN_x, is tested. The motivation behind this stack is the fact the H effusion from the AlO_x layer can occur during the FGA and an additional SiN_x layer can act as an effusion barrier for H atoms towards the atmosphere.

The results, are depicted in Figure 4.12, where different thicknesses are examined for the AlO_x layer, while the SiN_x layer thickness is kept constant at 100 nm. Additionally, the FGA is performed in the same conditions as examined in the previous sections, namely at 400 °C for 30 minutes. In the left part of the Figure 4.12 the results are illustrated for an AlO_x capping layer (same as Section 4.5.1), while in the right part different combinations of the AlO_x & SiN_x double capping layer are illustrated.

Depositing an additional SiN_x capping layer (red line) after the FGA of the AlO_x stack can benefit the passivation quality slightly, indicating that AlO_x is not providing sufficient passivation. This can be linked to the additional H atoms available after the SiN_x deposition. Again, the passivation seems to be independent of the AlO_x thickness implying that a 3 nm layer is already sufficient.

Performing a second FGA (blue line) after the SiN_x deposition has no effect (for the case of an 3 and 10 nm AlO_x layer) or can even deteriorate (in the case of 7 nm AlO_x layer) the passivation quality of the sample. This could be attributed to the too long annealing and thermal budget received by the sample.

Finally, a stack of AlO_x and SiN_x is deposited and the whole stack followed by FGA (brown line). As it can be seen from the graph, a significant passivation boost can be realized when the whole stack is followed by FGA compared to the other methods. In general, it was observed earlier that only a slight improvement can be realized when the SiN_x capping layer is deposited after a FGA has been performed on the AlO_x layer. This could be possibly attributed to the fact that following the FGA the AlO_x layer is depleted of H atoms and when the SiN_x is deposited some of the H atoms accumulate at the AlO_x layer providing no additional benefit on the poly-SiC_x layer. Interestingly, it seems that a thicker layer of AlO_x seems to be negatively influencing the passivation quality of the sample, since the best result of 708 mV is realized with an 3 nm AlO_x & 100 nm SiN_x stack. Thicker AlO_x layers demonstrate an iV_{oc} lower than 700 mV.

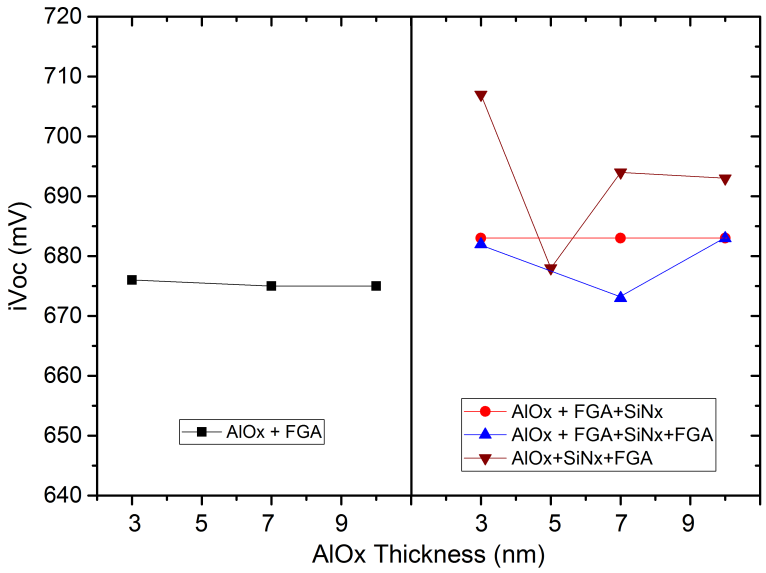

Figure 4.12: iV_{oc} of hydrogenated (p)poly-SiC_x symmetrical samples with different capping layers.

4.5.3 Silicon Nitride as Capping Layer

In this section the hydrogenation optimization using SiN_x as a capping layer is examined. This layer demonstrated in the earlier sections the best passivation properties and it is tested in this section for both (p)-doped and (n)-doped poly-SiC_x symmetrical samples. It has to be noted that (n)poly-SiC_x symmetrical samples are tested in the prospective of fabricating solar cells with poly-SiC_x passivating contacts at the front and the rear. Thus, an optimum condition for both doped layers needs to be found.

In this series of experiments, different thicknesses are examined, namely 80, 100 and 120 nm for p-type poly-SiC_x symmetrical samples and 100 and 120 nm for n-type poly-SiC_x symmetrical samples, all followed by a FGA at 400 °C for 30 minutes. A thickness of 100 nm represents the reference SiN_x capping layer used so far.

In Figure 4.13 the results are depicted. Regarding the p-doped poly-SiC_x symmetrical samples, a slight increase in iV_{oc} can be observed with increasing the SiN_x thickness. This could be attributed to the fact that more H atoms are contained within a thicker layer, which can then be supplied to passivate more dangling bonds in the sample. The best result obtain is for the 120 nm thick layer demonstrating an iV_{OC} of 709 mV, a minority carrier lifetime of 3.4 ms and a J_o of 10.5 fA/cm^2. It has to be noted that this is the best passivation achieved so far for p-type poly-SiC_x samples.

Looking at the n-type samples, a similar trend is observed, meaning that a thicker SiN_x can be beneficial on passivation quality. Even though the iV_{oc} remains 728 mV for both an 100 and 120 nm of SiN_x capping layer, an impressive gain in minority carrier lifetime is observed for the 120 nm layer. In more details, the 120 nm layer demonstrates a minority carrier lifetime of 8.6 ms compared to the 4.4 ms observed for the 100 nm layer.

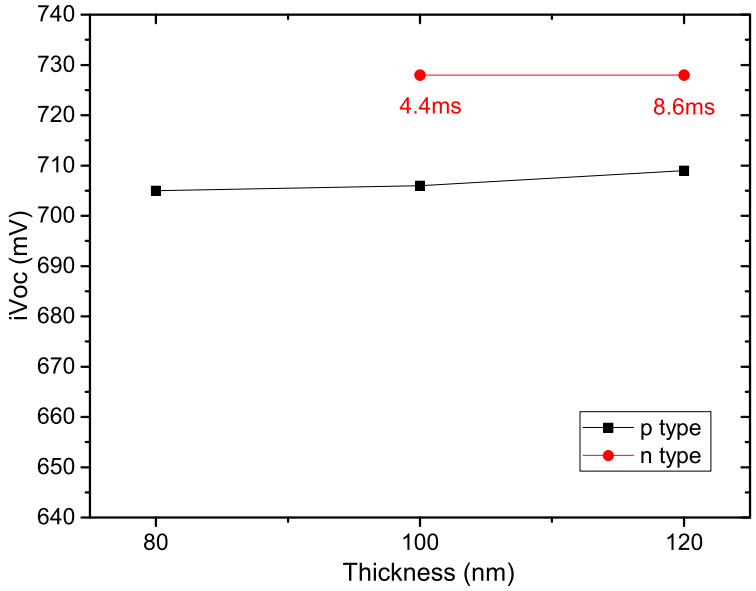

Figure 4.13: Passivation results for p-type and n-type samples with SiN_x capping layer.

4.5.4 Effect of Forming Gas Annealing Temperature and Duration

In the final part of the hydrogenation optimization, different FGA temperatures and durations were tested with the aim to further check the temperature stability of the optimized doped stacks. The results for this part of experiments are illustrated in Figure 4.14, where both p-type and n-type poly-SiC_x symmetrical samples were examined, using the best performing capping layer thickness found from the previous sections, namely 120 nm of SiN_x.

Regarding the p-type samples, it was found that the low thermal budget (400 °C for 30 minutes) performes the best. Increasing the annealing duration to 60 minutes for the 400

°C significantly deteriorates the passivation quality. Applying a higher FGA temperature seems perform worse than the initially tested condition of 400 °C /30 mins, but better compared to 400 °C /60 mins. Regarding the n-type samples, a great thermal stability can be observed. As it is illustrated from the results the best result of 728 mV is obtained for an FGA at 400 °C and 30 minutes with a τ_{eff} of 8.6 ms, while a slightly lower τ_{eff} of 7.8 ms is observed for the sample annealed for 60 minutes. FGA at a temperature of 500 °C yields an iV_{oc} of only 2 mV lower and a τ_{eff} of 4.9 ms and 4.6 ms for the sample annealed for 30 and 60 minutes respectively. This trend could be due to the fact that higher temperatures and longer durations can cause hydrogen to effuse out of the material instead of the poly-SiC_x leading to a lower passivation quality.

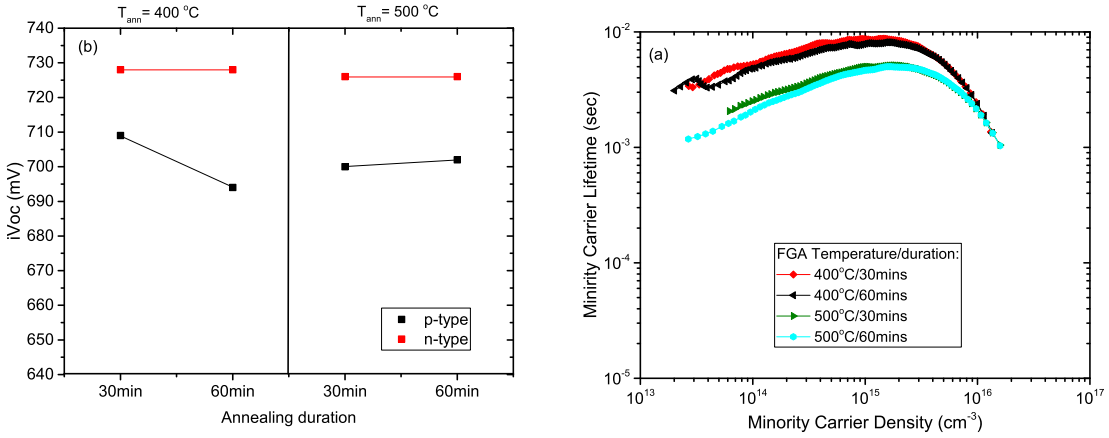

Figure 4.14: iV_{oc} of poly-SiC_x symmetrical samples for variable FGA temperatures and durations (a) and lifetime of (n)poly-SiC_x symmetrical samples for variable FGA temperatures and durations (b).

4.6 Conclusions

In this chapter, the passivation optimization was performed. Firstly, p-type poly-SiC_x symmetrical samples were fabricated entirely by PECVD (for both the a-Si:H interlayer and (p)poly-SiC_x layer) incorporating different carbon contents and annealed at various combinations of temperatures and durations. Through this analysis it was found that the best performing sample with a gas flow ratio of 69.2 %, demonstrated an iV_{oc} of 684 mV, τ_{eff} of 1.4 ms and J_o of 34.7 fA/cm^2 for an a-Si:H interlayer of 8 nm. Following, samples fabricated by LPCVD (for the a-Si:H interlayer) and PECVD (for the (p)poly-SiC_x layer) were examined and again the sample with a gas flow ratio of 69.2% achieved the best passivation quality. It was observed that this sample outperformed the sample fabricated entirely by PECVD, demonstrating a significantly higher iV_{oc} of 706 mV, τ_{eff} of 2.26 ms and J_o of 12.7 fA/cm^2 for an a-Si:H interlayer of 12 nm.

Finally, in order to further increase the passivation quality of the aforementioned sample different hydrogenation schemes were investigated using different capping layers and different FGA temperatures and durations. The best performing p-type sample was realized

with a SiN_x capping layer of 120 nm and FGA at 400 °C for 30 minutes, demonstrating an iV_{oc} of 709 mV, τ_{eff} of 3.4 ms and J_o of 10.5 fA/cm^2. Furthermore, n-type samples were examined in terms of hydrogenation optimization and the best performing sample was also realized for the same hydrogenation scheme demonstrating an iV_{oc} 728 mV, τ_{eff} of 8.6 ms and J_o of 2.9 fA/cm^2.

Chapter 5

Integration of (p)poly-SiC_x in Rear Emitter Solar Cells

In this chapter, the (p)poly-SiC_x passivating contact optimized in Chapter 4 is applied on a device level in rear emitter solar cells. Firstly, double side polished (DSP) solar cells are fabricated. For these solar cells, different a-Si:H interlayer thicknesses are investigated as well as the influence of different metallization schemes. In addition, the effect of a variation of the doping gas flow on cell's parameters is investigated. Furthermore, an variation is performed the gas flow ratio in order to examine the optical response for different carbon contents. Finally, front side textured (FST) solar cells are fabricated with different (p)poly-SiC_x thicknesses in order to investigate the optical benefit of a textured surface.

5.1 Experimental Details

In this Section the experimental details regarding the fabrication of FBC solar cells incorporating poly-SiC_x passivating contacts are presented. A schematic of the deposited layers is given in Figure 5.1, in order to better visualize the fabrication process of solar cells.

For the bulk material, n-type FZ wafers are used with $< 100 >$ orientation and a thickness of 280 μm. The processing steps are as follows:

1. This first step is not performed on DSP cells but only for FST cells, in order to receive the textured surface. Firstly, a 150 nm thick SiN layer is deposited on one side to act as a protection layer from the texturing solution. Following, the wafer is immersed in a solution of water, Alka-tex and Tetramethylammonium Hydroxide (TMAH) at 80 °C for approximately 10 minutes in order to uniformly texture the unprotected side of the c-Si wafer. In the next step, the wafer is immersed in BOE solution until the textured side is completely hydrophobic and subsequently in a poly-etch solution for 2 minutes in order to achieve a rounding of the pyramids [93]. Finally, an additional immersion in BOE is performed until the SiN protective layer is completely etched obtaining the final FST wafer.

2. The wafer is cleaned by immersion in two HNO_3 baths, for 10 minutes in each bath, in order to remove organic and inorganic contaminants.

3. The tunelling oxide is formed by immersing the wafer in an HNO_3 (69.5%) bath at room temperature for 1 hour.

4. Following, the a-Si:H interlayer is deposited by either LPCVD or PECVD and next the doped a-SiC_x:H layers are deposited by PECVD.

5. After, a high-temperature annealing is performed at a temperature of 850°C for 5 minutes to crystallize the a-SiC_x:H layers as well as to drive in and activate the dopants, obtaining the poly-Si_x layers.

6. For hydrogenation, a 120 nm thick SiN_x capping layer is deposited on each side followed by FGA at 400°C for 30 minutes. Afterwards, the SiN capping layer is etched by immersion in a BOE bath.

7. Following, the ITO is sputtered on the front (n)poly-SiC_x layer with a thickness of 75 nm. Depending on the cell configuration, ITO can be also sputtered on the rear (p)poly-SiC_x layer and if ITO is also deposited on the rear its thickness is kept at 120 nm.

8. Finally, the front side metallization is performed by means of screen-printing (SP) using a low temperature silver paste. For the full-area rear side metallization, different schemes are investigated. Silver SP can be used or evaporation of aluminum or silver.

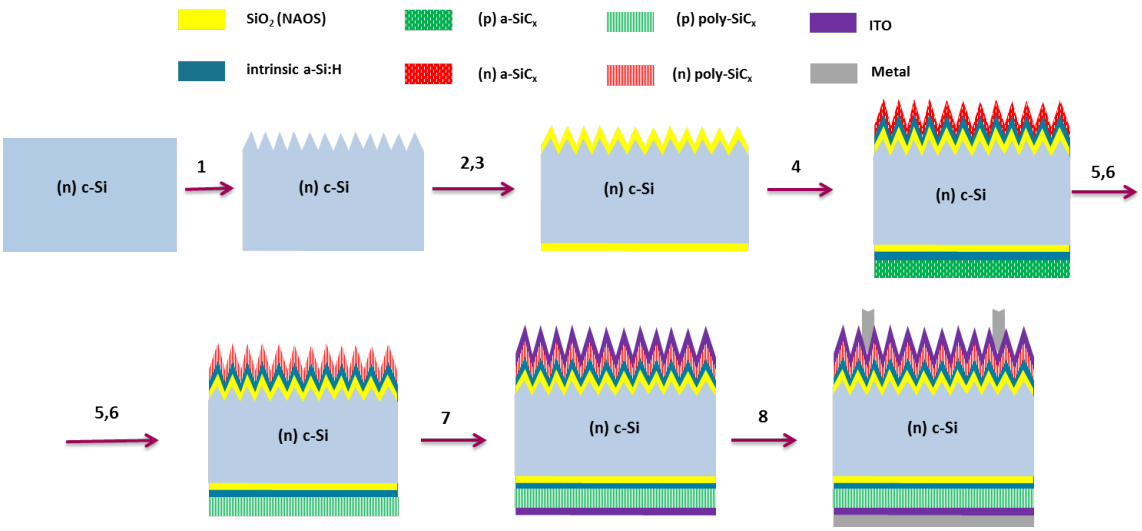

Figure 5.1: Schematic sketch of the fabrication process of the solar cell with poly-SiC_x passivating contacts at the rear and the front.

5.2 Influence of the a-Si:H Interlayer Thickness

In the first run of experiments on device level, a variation on the a-Si:H interlayer thickness, as also investigated on symmetrical samples in Chapter 4, was performed on the rear contact. For these DSP cells, the a-Si:H interlayer was deposited by PECVD, and was kept constant at 5 nm for the front side while thicknesses in the range of 0-10 nm were tested for the rear side.

After each fabrication step, the cell's precursors are evaluated in terms of passivation quality as shown in Figure 5.2a. The trend, as also seen in Section 4.2.4 for symmetrical samples, demonstrates that the sample with an interlayer of 5 nm achieves the highest passivation quality. The iV_{oc} after the annealing process, which lies in the range of 620-645 mV, indicates that the precursos is slightly passivated. Following, the hydrogenation treatment causes the iV_{oc} to increase in the range of 660-685 mV, implying that the c-Si/SiO_x interface is further passivated. Regarding the 5 and 10 nm rear interlayer, the values for the iV_{oc} are in the same range as observed in Chapter 4. For the 0 nm rear interlayer the iV_{oc} value is considerably higher, which can be attributed to the fact that the front contact incorporates a 5 nm interlayer benefiting the total passivation quality of the device. We confirm at this point our previous observation from Chapter 4 and as also demonstrated in study [59], that the presence of an (i)a-Si interlayer is required for a high passivation quality, since the sample without a rear interlayer demonstrates the lowest passivation quality. Following, the ITO deposition causes a slight drop in iV_{oc}, due to the sputtering damage as it has also been observed in other studies [60, 62, 94]. The final V_{oc} of the cells lies in the range of 635-665 mV and is lower than the $SunsV_{oc}$ measured. This can be attributed to the metal deposition technique, the formation of blisters and the metal diffusion paths and the series resistance which in turn can reduce the passivation quality of the solar cell [47].

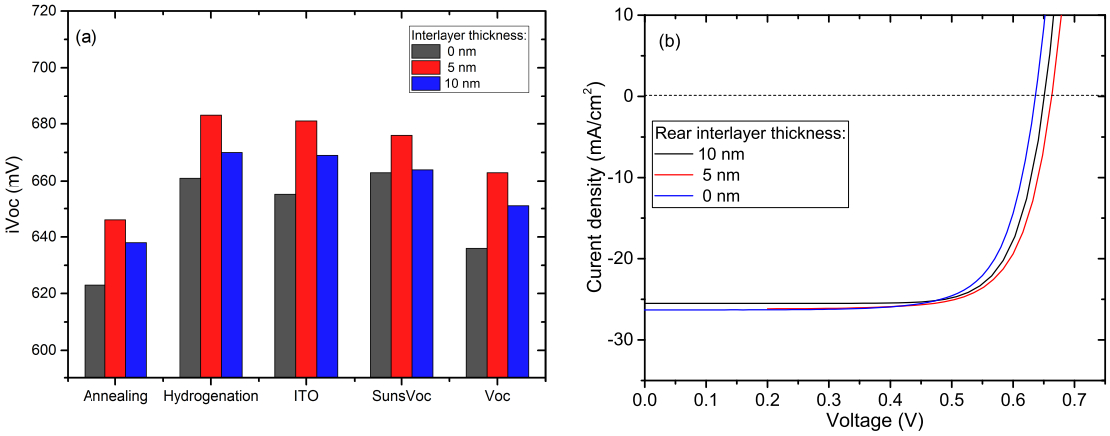

Figure 5.2: iV_{oc} of cells' precursors after each fabrication step (a) and J-V curves of final cells (b) with variable interlayer thickness for the rear contact.

The results regarding each cell's parameters are tabulated in Table 5.1. It has to be noted that J_{sc} refers to the value obtained through the illuminated J-V curve while $J_{sc,EQE}$ refers to the value obtained through the EQE measurement (without grid coverage). This distinction is made because during the illuminated J-V curve measurement the probe can cause shading on the cell reducing the total current. Thus, $J_{sc,EQE}$ is used to obtaining η_{act} which demonstrates the maximum potential efficiency in the absence of any shading.

As it can be seen from Table 5.1 a difference between the pFF and FF in the range of approximately 5% is observed for all cells, indicating that the series resistance is substantial after metallization. The FF for all cells lies in the range of 75% and is limited by the high series resistance. Nevertheless, no S-shape is observed in the illuminated J-V curve (Figure 5.2b).

Table 5.1: Summary of parameters for solar cells fabricated with various interlayer thicknesses.

Interlayer [**nm**]	$\mathbf{V_{oc}}$ [**mV**]	**pFF** [%]	**FF** [%]	$\mathbf{J_{sc}}$ [$\mathbf{mA\backslash cm^2}$]	$\mathbf{J_{sc,EQE}}$ [$\mathbf{mA\backslash cm^2}$]	η [%]	η_{act} [%]
0	637	78.7	74.4	26.9	31.02	12.75	14.70
5	662	80.3	75.3	25.6	30.88	12.76	15.39
10	651	81.8	76.8	25.5	30.82	12.75	15.51

Furthermore, an optical characterization is performed. For this characterization, the EQE of the cells alongside the reflection are depicted in Figure 5.3. It is visible, that the EQE and 1-R are almost identical for all fabricated cells, indicating that the range of 0-10 nm for the rear interlayer has little effect on the absorption of the cell. Nevertheless, the thicker the layer a small loss can be observed in $J_{sc,EQE}$ (seen in Table 5.1) which can be attributed to the higher absorption for a thicker layer. Furthermore, the difference between the 1-R and EQE represents the losses. We observe, as expected, that in the shorter wavelengths the losses are high, which can be related to the fact that the front (n)poly-SiC_x layer has not been textured and also it has not been optimized in terms of thickness, thus contributing to a high parasitic absorption. In addition, in the longer wavelengths high optical losses can be observed, which can be linked to the energy of the photons not being high enough to be absorbed, thus propagating through the material without contributing to $J_{sc,EQE}$.

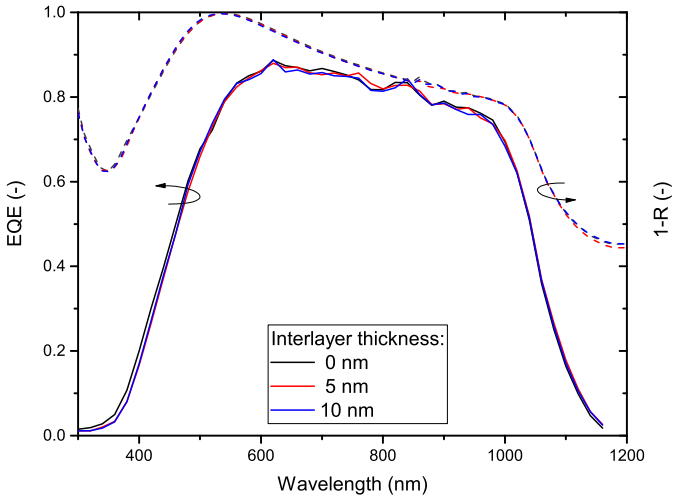

Figure 5.3: EQE (solid) and 1-R (dashed) curves of fabricated solar cells with variable interlayer thickness for the rear contact.

5.3 Influence of Different Metallization Schemes

For this series of experiments different metallization schemes are investigated for the rear contact on DSP solar cells. Depending on the metallization scheme, ITO can be sputtered or not at the rear contact. An overview of the metallization schemes investigated is provided in Table 5.2. It is noted that a hybrid cell (cell 1), featuring a (nc)-SiO_x front contact and the optimized (p)poly-SiC_x developed in this work as a rear contact. This cell was fabricated by other members of the PVMD group and is illustrated for a comparison.

Table 5.2: Metallization schemes investigated.

Cell	Rear ITO	Material	Method
1	-	Ag	SP
2	120 nm	Ag	SP
3	-	Ag (200 nm)+Ag	Evaporation + SP
4	-	Ag (800 nm)	Evaporation
5	-	Al (1000 nm)	Evaporation

The iV_{oc} for the cell precursors at each fabrication stage is illustrated in Figure 5.4a and as observed also for the previous cells, the hydrogenation substantially increases the iV_{oc} of all cells from the range of approximately 593-660 mV after the annealing step to approximately 630-709 mV after hydrogenation. Again, the ITO deposition seems to slightly undermine the passivation quality, which can be linked to sputtering damage. The final V_{oc} of the fabricated cells lies in the range of 648-675 mV, which is lower than the SunsVoc due to the series resistance.

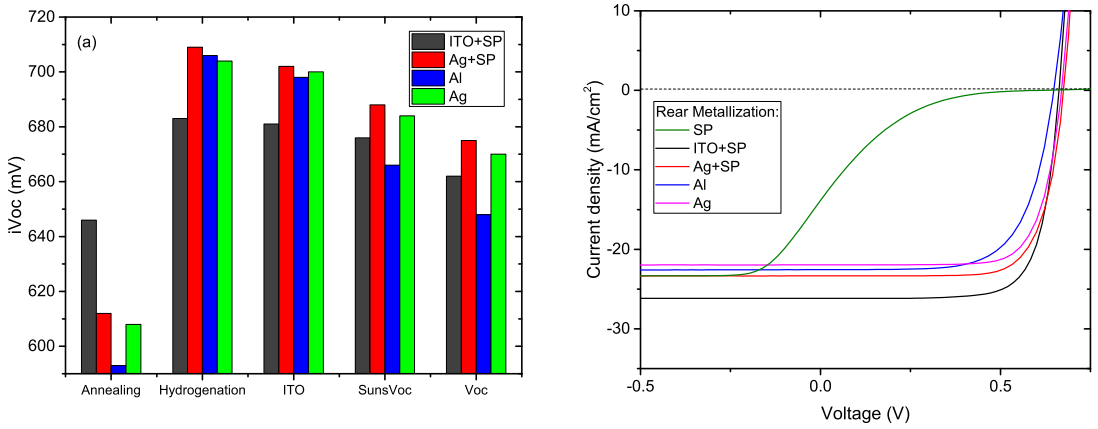

Figure 5.4: iV_{oc} of cells' precursors after each fabrication step (a) and J-V curves of final cells (b) with different metallization schemes for the rear contact.

Table 5.3 depicts the results of the fabricated solar cells. As it can be observed the worst performing cell is the hybrid cell. This cell demonstrates a very low FF of 10.8%, indicating that a direct SP can not facilitate effectively the minority carrier transport. Following, the deposition of the ITO before the SP can significantly boost the FF up to 75.3%. Additionally, a thin Ag evaporation before the SP can also create a working condition, replacing the ITO, and reaching a comparable FF of 74.1%. Furthermore, the evaporation of Ag can also offer a FF in the same range at 74.7%. The cell with the ITO+SP exhibits a lower V_{oc} of 662 mV compared to the cell with evaporated Ag+SP and to the cell with evaporated Ag, which achieve a V_{oc} of 670-675 mV. This can be attributed to the additional sputtering damage received by the cell incorporating the ITO. Finally, the cell with evaporated Al demonstrates a low V_{oc} and also a low FF, indicating a poor carrier collection. The difference of 10% in pFF and FF for this cell indicates the high series resistance for Al contacting. This could be attributed to a work function mismatch between the (p)poly-SiC_x and Al contact, leading to a poorer carrier selectivity. The illuminated J-V curve is illustrated in Figure 5.4b, where it is visible that the cell with Al contacts suffers from a lower FF compared to the other metallization schemes, while the cell with direct SP shows an S-shaped J-V curve.

Table 5.3: Summary of parameters of solar cells fabricated with different metallization schemes.

Rear Metallization	$\mathbf{V_{oc}}$ [mV]	**pFF** [%]	**FF** [%]	$\mathbf{J_{sc}}$ [mA\cm^2]	$\mathbf{J_{sc,EQE}}$ [mA\cm^2]	η [%]	η_{act} [%]
SP	606	-	10.8	13.86	-	0.91	-
ITO+SP	662	80.3	75.3	25.6	30.88	12.76	15.39
Ag evaporated + SP	675	79.3	74.1	23.3	28.78	11.65	14.40
Ag evaporated	670	79.7	74.7	21.9	29.23	11.01	14.63
Al evaporated	648	77.7	67.5	22.6	28.05	9.88	12.27

For the optical characterization, EQE and 1-R is plotted in Figure 5.5. It is obvious that depending on the metallization scheme the EQE can vary significantly. The cell with the ITO+SP metallization scheme, has a higher EQE, which can be linked to the additional ITO on the rear. Furthermore, the 1-R curve for this cell is considerably higher in the longer wavelength region, meaning that less reflection occurs. The additional rear ITO can boost the EQE by allowing a better light trapping and less reflection. Since the different metallization schemes are incorporated on the rear, the EQE in the longer wavelengths is of interest. It seems that Ag as the material can demonstrate an improved EQE. On the other hand, the cell with Al as the material for the rear contact demonstrates a lower EQE over the entire range, which can be attributed to its lower electrical performance (as seen in Table 5.3), thus the carrier collection is not optimal reducing the output current. Again, high parasitic absorption can be observed in the short wavelength range due to the non-optimized in thickness flat (n)poly-SiC_x contact.

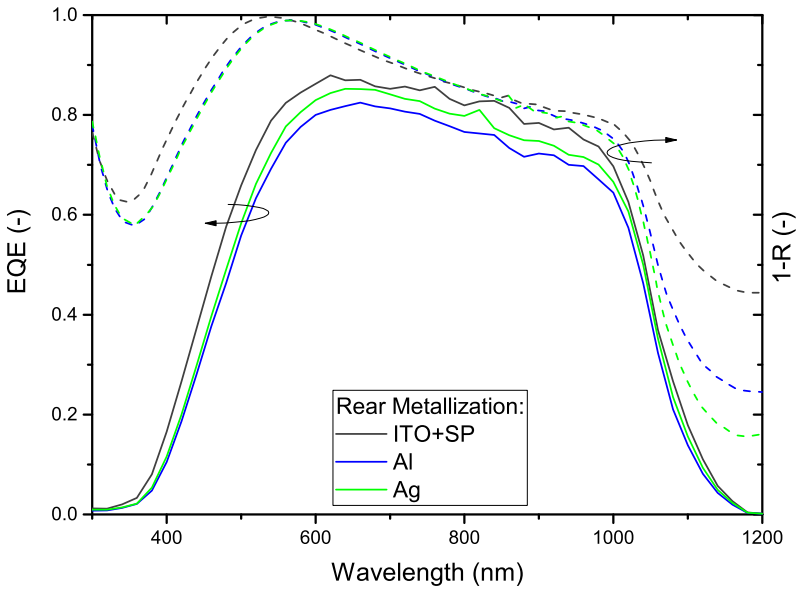

Figure 5.5: EQE (solid) and 1-R (dashed) curves of fabricated solar cells with different metallization schemes for the rear contact.

From this point on ITO+SP is used as the metallization scheme due to its higher overall perfrormance. It enables a slightly higher FF compared to other metallization schemes and a better optical response, obtaining a higher current. The drawback of this metallization scheme is the slightly lower final V_{oc} of the solar cell.

5.4 Influence of Doping Gas Flow

Following, an investigation on the doping gas flow is performed on DSP solar cells. For these cells, the a-Si interlayer is deposited by LPCVD and the thickness is kept at 12 nm, as it was found optimal on symmetrical samples in Chapter 4. The doping gas flow B_2H_6 is varied in the range of 1-5 sccm.

The iV_{oc} for the cell precursors at each fabrication stage is illustrated in Figure 5.6a , and as it was also observed from Chapter 4 depositing the a-Si interlayer by LPCVD can benefit the passivation quality. The iV_{oc} is almost identical for all cells during each fabrication step, while for the final V_{oc} the higher the doping flow a slightly higher V_{oc} can be realized. This can be attributed to the fact that the higher doping investigated can lead to a better carrier collection, leading to a higher V_{oc}. Again, there can be observed a slight degradation, due to sputtering damage, after the ITO deposition.

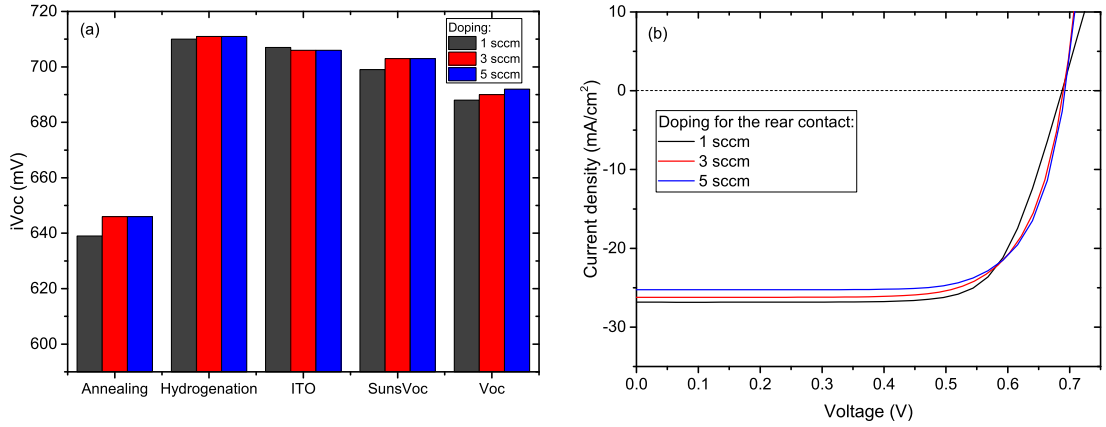

Figure 5.6: iV_{oc} of cells' precursors after each fabrication step (a) and J-V curves of final cells (b) with variable doping gas flow for the (p)poly-SiC_x layer.

Each cell's parameters are depicted in Table 5.4, where it can be seen that the cell with the highest doping of 5 sccm achieves the best performance. This cell demonstrates the highest FF and V_{oc}, but it has to be noted that the FF and V_{oc} is in the same range for all cells. The difference between the pFF and FF indicates the presence of series resistance following the metallization, but no S-shape is observed in the illuminated J-V curves for a doping gas flow of 3 and 5 sccm, while for the lowest doping gas flow of 1 sccm a slight S-shape is observed (Figure 5.6b). This can be attributed to a weaker band bending for the lower doping resulting in a lower accumulation of holes near the c-Si/SiO_2 interface, compared to the cells with higher doping levels [95]. The V_{oc} of these cells is higher of the cells fabricated in the previous sections, which is due to the LPCVD deposited interlayer. Using LPCVD instead of PECVD for the interlayer deposition was shown to yield a better passivation quality in Chapter 4.

Table 5.4: Summary of parameters for solar cells fabricated with variable doping gas flow for the (p)poly-SiC_x layer.

Doping [sccm]	**V_{oc} [mV]**	**pFF [%]**	**FF [%]**	**J_{sc} [mA\cm^2]**	**$J_{sc,EQE}$ [mA\cm^2]**	η [%]	η_{act} [%]
1	688	82.7	73.9	26.6	30.43	13.52	15.47
3	690	78.1	73.0	26.2	30.38	13.20	15.30
5	692	79.1	74.7	24.7	30.35	12.77	15.68

The EQE and 1-R curves are illustrated in Figure 5.7, where for all cells the EQE and 1-R are almost identical. It is known that a higher doping can lead to a higher FCA [42, 44, 60], but not significant effect on FCA is observed on the EQE when the doping flow fluctuates by only 2-4 sccm. Also for these DSP solar cells, significant losses due to parasitic absorption occur at the short wavelength region, as seen from the large difference between 1-R and EQE curves, due to the non-optimized (n)poly-SiC_x layer and the poor light trapping of the front flat surface.

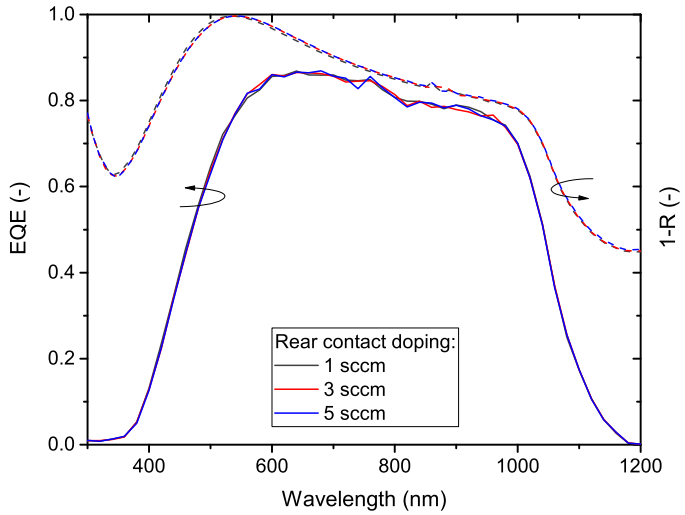

Figure 5.7: EQE (solid lines) and 1-R (dashed lines) of fabricated solar cells with variable doping gas flow for the (p)poly-SiC_x layer.

5.5 Influence of Gas Flow Ratio

For the final experiment on DSP solar cells a variation in the gas flow ratio of the rear contact is performed. The R investigated are 53.8%, 69.2% and 84.6%.

The iV_{oc} for the cell precursors at each fabrication stage is illustrated in Figure 5.8a. As it was also observed in Chapter 4, the sample with a gas flow ratio equal to 84.6% demonstrates a worse passivation quality. Furthermore, a more pronounced drop in the SunsVoc and final V_{oc} of this cell, indicates the poor passivation quality and high series resistance.

On the other hand, the cells with a gas flow ratio equal to 53.8% and 69.2%, demonstrate a similar passivation quality as observed also in Chapter 4 for symmetrical samples.

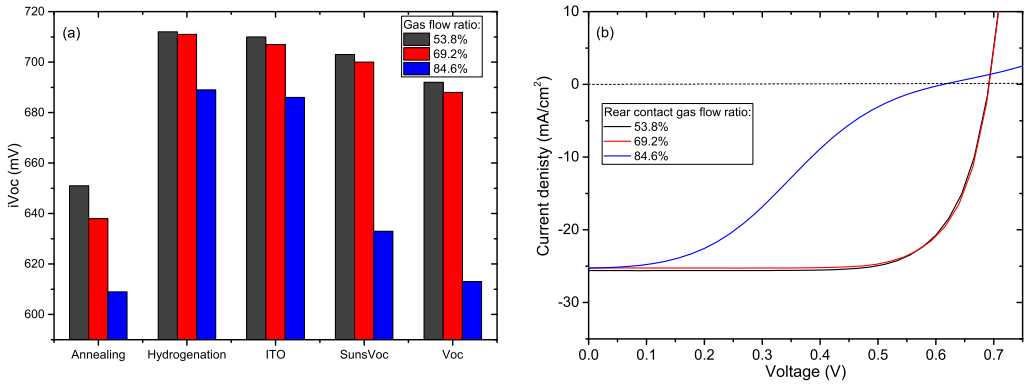

Figure 5.8: iV_{oc} of cells' precursors after each fabrication step (a) and J-V curves of final cells (b) with variable gas flow ratio for the (p)poly-SiC_x layer.

Each cell's parameters are depicted in Table 5.5. For the cells with R equal to 53.8% and 69.2% a difference in the range of 5%, as also observed for the previously fabricated solar cells, exists between pFF and FF indicating the presence of series resistance. Interestingly, for the cell with R equal to 84.6% a difference of approximately 55% between the pFF and FF, as well as the very low FF of 33% indicates a very high series resistance, which hinders the carrier transport significantly. The effect of the carbon content on the layer crystallinity and conductivity was demonstrated in Chapter 3. It was shown, that the sample with R equal to 84.6% remains highly amorphous following the thermal treatment and exhibits a very low conductivity ($1.17 \cdot 10^{-6}$ S/cm). The combination of the two aforementioned effects leads to so low values of FF. As a result, this cell achieves a very low η_{act} of only 5.97%. Furthermore, the effect of the aforementioned high series resistance is visible in Figure 5.8b, where S-shape can be observed in the illuminated J-V curve for the cell with R equal to 84.6%.

Table 5.5: Summary of parameters for solar cells fabricated with variable gas flow ratio for the (p)poly-SiC_x layer.

Gas Flow Ratio [%]	$\mathbf{V_{oc}}$ [mV]	**pFF** [%]	**FF** [%]	$\mathbf{J_{sc}}$ [mA/cm²]	$\mathbf{J_{sc,EQE}}$ [mA/cm²]	η [%]	η_{act} [%]
53.8	692	79.3	73.6	25.6	29.58	13.04	15.06
69.2	688	79.7	74.7	24.9	29.53	12.79	15.18
84.6	613	87.8	33.0	25.3	29.53	5.12	5.97

Finally, the EQE and 1-R curves are illustrated in Figure 5.9. As it can be seen the EQE is almost identical for all cells. It was observed in Chapter 3, that a lower gas flow ratio leads to a higher absorption coefficient, but apparently for such a thin rear contact this effect is almost negligible.

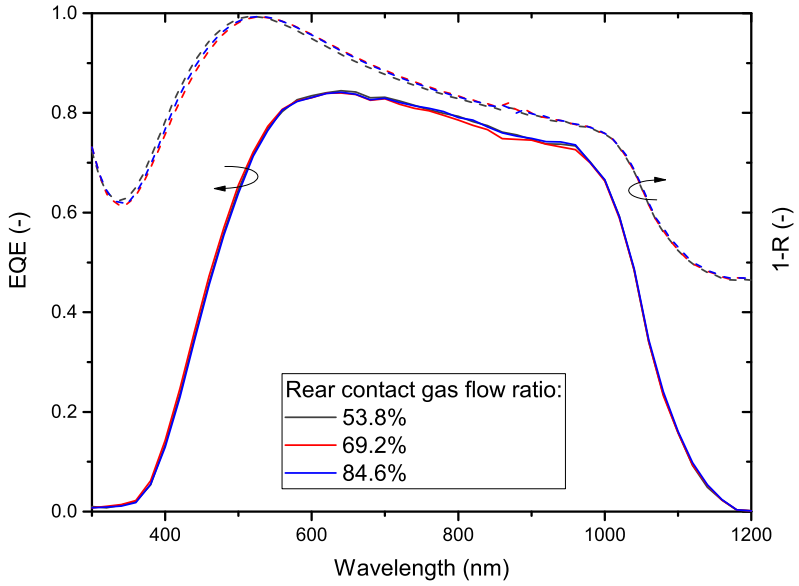

Figure 5.9: EQE (solid) and 1-R (dashed) curves of fabricated solar cells with with variable gas flow ratio for the (p)poly-SiC_x layer.

5.6 Influence of the (p)poly-SiC_x thickness

Finally, FST solar cells are examined. The gas flow ratio is kept at 69.2% while the a-Si interlayer is deposited by LPCVD. Furthermore, a variation on the thickness of the rear (p)poly-SiC_x layer is performed.

In Figure 5.10a, the iV_{oc} for the cell precursors at each fabrication stage is cell is depicted. As it can be seen following the metallization the SunsVoc and the final V_{oc} of the device suffer a significant drop. This indicates the high series resistance following the metallization, as well as the fact the metallization process can cause a higher damage on a textured surface.

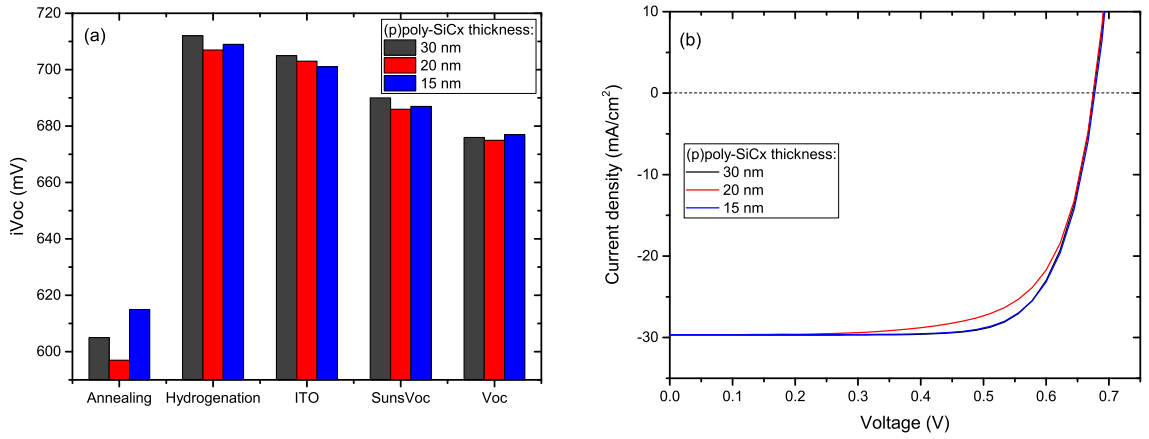

Figure 5.10: iV_{oc} of cells' precursors after each fabrication step (a) and J-V curves of final cells (b) with variable (p)poly-SiC_x thickness.

As it can be seen on Table 5.6, after texturing the front surface the FF of the cell remains essentially the same, while the V_{oc} is decreased. The reduction of the V_{oc} can be attributed to the textured front surface of the cell, which had not been fully optimized at this stage.

Looking at Table 5.6, a variation in the (p)poly-SiC_x thickness is investigated. As it can be observed, the thickness of the (p)poly-SiC_x does not significantly affect the V_{oc}. The difference of approximately 5% between pFF and FF consists as also observed for the DSP cells, indicating the presence of series resistance. The lower FF for the cell with the 20 nm thick (p)poly-SiC_x layer can be attributed to the fact that this particular cell depicted a crack on its surface and some of the metal fingers were damaged. As a consequence, the metallization area was less compared to the other cells, hindering the FF. Additionally, the illuminated J-V curves are depicted in Figure 5.10b, where no S-shape is observed for any of the fabricated cells. The J-V curves for the cell with 30 nm and 15 nm (p)poly-SiC_x overlap.

Table 5.6: Summary of parameters for solar cells fabricated with variable (p)poly-SiC_x thickness.

(p)poly-SiCx thickness [nm]	**V_{oc} [mV]**	**pFF [%]**	**FF [%]**	**J_{sc} [mA/cm²]**	**$J_{sc,EQE}$ [mA/cm²]**	η [%]	η_{act} [%]
30	676	78.9	74.9	29.7	31.06	15.04	15.73
20	675	77.2	70.3	29.6	32.82	14.04	15.57
15	677	79.0	74.7	29.7	33.22	15.02	16.80

Finally, the optical characterization is performed and the results are illustrated in Figure 5.11 for the cells with a variable (p)poly-SiC_x thickness. As it can be observed the thinner the (p)poly-SiC_x layer the higher the EQE. As it was observed in Chpater 3, the (p)poly-SiC_x layer suffers from a high absorption coefficient even after the high-thermal treatment. Thus, minimizing the layer's thickness can lead to lower parasitic absorption benefiting the EQE. As mentioned for the previous solar cells, the non-optimized in terms of thickness

front (n)poly-SiC_x leads to high loses in the shorter wavelength region reducing the total current.

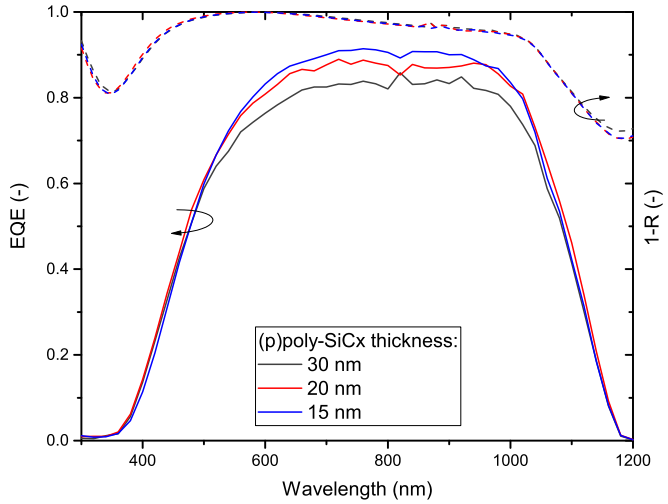

Figure 5.11: EQE (solid) and 1-R (dashed) curves of fabricated solar cells with with variable rear (p)poly-SiC_x layer thickness.

Chapter 6

Conclusions and Outlook

6.1 Conclusions

The aim of this thesis work is the optimization of the (p)poly-SiC_x passivating contacts in order to fabricate solar cells with the aforementioned contacts at the rear side of the device. Through various experiments performed the main findings of this thesis work are summarized in this chapter.

In the first part, experiments were carried out in order to characterize poly-SiC_x layers with different carbon contents (Chapter 3) . It was found that higher amounts of carbon in the material hinder crystallization during the high-temperature annealing step. Gas flow ratio and crystallization are inversely related, meaning that the lower gas flow ratio (53.8%, 61.5%, 69.2%) leads to a higher crystallization. Interestingly, for the highest gas flow ratios examined (84.6% and 76.4%) the material remains completely amorphous even after the thermal treatment (850 °C/5 mins). Additionally, the absence of a distinct peak for SiC in Raman measurements, might indicate the formation of nanocrystalline silicon grains surrounded by an a-SiC_x tissue [72]. Furthermore, it was found that a higher gas flow ratio leads to less hydrogen incorporated in the as-deposited layer. Independently of the hydrogen content in the layer, it was observed, as expected, that the subsequent annealing step causes the hydrogen to effuse out of poly-SiC_x.

Regarding the opto-electrical properties of the layer, alloying with carbon leads to a more transparent layer in the as deposited state. On the other hand, following the thermal treatment of the layer, a lower carbon content leads to a more transparent layer. This phenomenon is not fully understood yet but could be linked to the higher amorphous fraction of the layer for higher carbon contents, leading to a higher absorption. In addition, we observe that the hydrogenation step has no effect on the absorption coefficient of the layer. Going into the electrical characterization of the layer, higher gas flow ratios during the deposition can hinder the conductivity of the final poly-SiC_x layer by several orders of magnitude, which can be linked to the higher amorphous fraction for the layers with high carbon contents (as demonstrated by Raman measurements). Similarly, the activation energy increases for higher carbon contents in the layer. We also observe, that the thermal treatment of the layer can significantly benefit the electrical performance, leading to

a much higher conductivity for the poly-SiC_x layer compared to the a-SiC_x:H layer. The dark conductivity for the optimum gas flow ratio (69.2%) is equal to 0.006 S/cm and the activation energy equal to 171 meV.

In order to optimize the (p)poly-SiC_x passivating contact, the layer deposition parameters alongside various annealing combinations were investigated on symmetrical samples (Chapter 4). It was demonstrated that the deposition of an (i)a-Si interlayer is crucial for achieving a high passivation quality, while a hydrogenation step is needed in order to further increase the surface passivation quality of the c-Si/SiO_x interface. Additionally, it was found that the deposition of the (i)a-Si interlayer by LPCVD yields a higher performance compared to the PECVD deposited interlayer. We ascribe that to the lower porosity and hydrogen content of the LPCVD film compared to the PECVD one [42]. In more details, the best passivation achieved by PECVD was realized for an 8 nm thick interlayer demonstrating an iV_{oc} of 684 mV and J_o of 34.7 fA/cm^2, while a significantly higher passivation with an iV_{oc} of 706 mV and J_o of 12.7 fA/cm^2 was obtained for a 12 nm thick LPCVD deposited interlayer.

Furthermore, different hydrogenation schemes were investigated using different capping layers (AlO_x, SiN_x and AlO_x/SiN_x) and FGA temperatures/durations in order to further increase the passivation quality. Consequently, a further increase in passivation with an iV_{oc} at 709 mV and J_o of 10.5 fA/cm^2 was realized for a 120 nm thick SiN_x capping layer and a subsequent FGA at 400°C for 30 minutes for (p)poly-SiC_x. For the hydrogenation optimization, also (n)poly-SiC_x developed by other members of the PVMD group were investigated where again the 120 nm SiN_x followed by a FGA at 400°C for 30 minutes demonstrated the best iV_{oc} of 728 mV and J_o of 2.9 fA/cm^2.

In the last part, the optimized (p)poly-SiC_x passivating contact is implemented in solar cells (Chapter 5). It was observed also on a device level that the (i)a-Si interlayer is required in order to achieve a sufficient passivation quality. Furthermore, different metallization schemes were investigated. It was observed that direct screen-printing can lead to a low FF (10.8%), but the deposition of an ITO or a thin evaporate Ag (200 nm) before the SP can greatly increase the FF up to 75%. Alternatively, evaporated Ag (800 nm) can also provide a sufficient carrier transport achieving a FF of 74.7%. Finally, we investigated Al evaporation (1000 nm), which was found to demonstrate a lower FF in the range of 67%. We also examined the doping level on a device level, where we found that 5 sccm of B_2H_6 provides the best performance. For the last experiment of DSP cells, we performed a variation on R where we observed that the high R of 84.6% suffers from a low FF, due to the higher amorphous layer and lower conductivity. Finally, we fabricated FST where a gain of 3 mA/cm^2 was obtained for the best performing cell with a textured surface, maintaining the FF at the same level, while a lower V_{oc} is expected due to the texturing. It has to be noted that for all cells examined the front (n)poly-SiC_x layer had not been optimized in terms of thickness, reducing considerably the output current due to parasitic absorption.

6.2 Outlook

The final cells fabricated still have a room for improvement according to the theoretical limit. Further investigation on the poly-SiC_x layers can lead to a higher efficiency solar cell, through various ways. Some of the possible solutions for further enhancing the performance of the solar cell incorporating poly-SiC_x passivating contacts are discussed in this section.

To enhance the solar cell J_{sc}:

As it was mentioned, the thickness of the front (n)poly-SiC_x passivating contact was kept at 35 nm for all solar cells fabricated in this work. An optimization on the thickness of the aforementioned layer could lead to a thinner layer, subsequently decreasing the parasitic absorption in the short wavelength region and enhancing the current of the solar cell.

Furthermore, as it was shown in Chapter 3, the incorporation of carbon leads to a more absorptive poly-SiC_x layer. When this layer is deposited on the front of the solar cell, the parasitic absorption can increase leading to a lower current. In order to tackle this, inter-digitated back contact solar cells can be fabricated. In such cells, both the p-doped and n-doped layer is deposited at the rear, thus the parasitic absorption can be minimized.

To enhance the passivation quality:

Different fabrication processes can be realized in order to further increase the passivation quality of the poly-SiC_x layer. One example, is the growth of the SiO_2. In this work, the SiO_2 was grown wet-chemically but a thermal oxide could be also investigated. It has been observed in other studies that a thermally grown oxide can enhance the passivation quality due to its higher density and thermal stability during the subsequent annealing step [42, 96].

To improve the fabrication process:

In this work it was shown that the deposition of an a-Si interlayer is crucial for a high passivation quality. It was demonstrated that the deposition of the interlayer by LPCVD can lead to a better passivation compared to a PECVD deposited interlayer. In order to simplify the fabrication process an optimization on the PECVD deposition parameters (pressure, power, H content etc) for the interlayer can be performed in order to achieve a passivation quality similar to the LPCVD deposited interlayer, thus realizing a solar cell fabricated entirely by PECVD depositions[59].

Acknowledgement

In the beginning of this academic year I chose a thesis topic related to the fabrication of solar cells, with the aim of getting cleanroom experience. This thesis work was carried out in the Photovoltaic Materials and Device (PVMD) group, whose all members I would like to thank.

I would also like to thank my supervisors Olindo and Luana. They provided me with great advice and guidance during those past months in order to better plan my experiments and understand the theoretical background behind this work. Additionally, I would like to express my gratitude to Martijn, who was always helping with any problems encountered in Amor, and Stefaan who always fixed the measurement setups.

Furthermore, I would like to thank my family back in Greece. They have been supporting me not only during the period of my thesis project but during these whole past two years of my Master degree while I was in the Netherlands.

Finally, I would like to thank my Sofia for all the support during this period. Thank you for listening to all my complaints about how things did not work out sometimes and for waiting patiently all this time. Even though you were far away, you were always there for me when I needed you the most. I will always treasure those long conversations.

It was all thanks to
"Love in a trashcan"

Antonis
TU Delft, 2019

Bibliography

[1] U.S. Energy Information Administration. *International Enegy Outlook 2017*.

[2] BBC. *The biggest energy challenges facing humanity*. URL: http://www.bbc.com/future/story/20170313-the-biggest-energy-challenges-facing-humanity.

[3] International Energy Agency. *CO_2 emissions from fuel combustion(2017)*.

[4] UNFCCC. *The Paris Agreement*. URL: https://unfccc.int/process-and-meetings/the-paris-agreement/the-paris-agreement.

[5] International Energy Agency. *Renewables 2018 (Market analysis and forecast from 2018 to 2023*.

[6] R. Perez and M. J. R. Perez. *A fundamental look at energy reserves for the planet*.

[7] D. R. Williams (NASA). *Sun Fact Sheet*. URL: https://web.archive.org/web/20100715200549/http://nssdc.gsfc.nasa.gov/planetary/factsheet/sunfact.html.

[8] Purcel and Morin. *Electricity and Magnetism*. Cambridge University Press, 2013.

[9] S.C Bhatia. *Advanced Renewable Energy Systems*, pp. 32–67.

[10] A. Smets et al. *Solar Energy - The physics and engineering of photovoltaic conversion, technologies and systems*. UIT Cambridge.

[11] International Renewable Energy (IEA). *Solar Energy*. URL: https://www.iea.org/topics/renewables/solar/.

[12] ISE Fraunhofer Institute for Solar Energy Systems. *Photovoltaics Report*. Fraunhofer ISE.

[13] R.M. Swanson. "Approaching the 29% limit efficiency of silicon solar cells". *Conference record of the IEEE Photovoltaics Specialist Conference* (2005), pp. 889–894.

[14] A. Richter, M. Hermle, and S.W. Glunz. "Reassessment of the limiting Efficiency for Crystalline Silicon Solar Cells". *IEEE Journal of Photovoltaics* 3 (2013), pp. 1184–1191.

[15] M. A. Green et al. "Solar cell efficiency tables (version 51)". *WILEY Progress in Photovoltaics* (2017).

[16] Power Electronic Tips. *Solar cells and power,Part 1 - basic operation*. URL: https://www.powerelectronictips.com/solar-cells-power-part-1-basic-operation/.

[17] M. Zeeman. *PV Basics Course*. TU Delft.

[18] B. Van Zeghbroeck. *Principles of Semiconductor Devices*. University of Colorado at Boulder, 2011.

[19] Electronics Tutorials. *PN Junction Theory*. URL: `https://www.electronics-tutorials.ws/diode/diode_2.html`.

[20] D. Mette. *New Concepts for Front Side Metallizaton of Industrial Silicon Solar Cells (PhD thesis)*. Fraunhofer Institute for Solar Energy Systems, 2007.

[21] S. Glunz, R. Preu, and D. Biro. "Crystalline Silicon Solar Cells- State of the Art and Future Developments". *Comprehensive Renewable Energy* 1 (2012), pp. 353–387.

[22] L. Tous. *Nickel/Copper Plated Contacts as an Alternative to Silver Screen Printing for the Front Side Metallization of Industrial high Efficiency Silicon Solar Cells (PhD thesis)*. KU Leuven, 2014.

[23] C. Battaglia, A. Cuevas, and S.D. Wolf. "High-efficiency crystalline silicon solar cells: status and perspectives". *Energy and Environmental Science* (2016).

[24] R. Peibst et al. "Recombination Behaviour and Contact Resistance of n+ and p+ poly -Crystalline Si/Mono-Crystalline Si Junctions". *Solar Energy Materials and Solar Cells* (2014), pp. 85–91.

[25] F. Feldman et al. "Passivated rear contacts for high-efficiency n-type Si solar cells providing high interface passivation quality and excellent transport characteristics". *Solar Energy Materials and Solar Cells* 120 (2014), pp. 270–274.

[26] U. Würfel, A. Cuevas, and P.Würfel. "Charge Carrier Separation in Solar Cells". *Solar Energy Materials and Solar Cells* (2014), pp. 85–91.

[27] K. Yoshikawa et al. "Silicon heretojunction solar cell with interdigitaded back contacts for a photoconversion efficiency over 26%". *Nature Energy* 2 (2017).

[28] D. Adachi, J. Luis Hernandez, and K. Yamamoto. "Impact of carrier recombination on fill factor for large area heterojunction crystalline silicon solar cell with 25.1% efficiency". *Applied Physics Letters* 107 (2015).

[29] J. Haschke et al. "Silicon heterojunction solar cells: Recent technological development and practical aspects - from lab to industry". *Solar Energy Materials and Solar Cells* 187 (2018), pp. 140–153.

[30] T. Sawada et al. "High-efficiency a-Si/c-Si heterojunction solar cell". *Proceedings of 1994 IEEE 1st World Conference on Photovoltaic Energy Conversion - WCPEC (A Joint Conference of PVSC, PVSEC and PSEC* (1994).

[31] M. Mews et al. "Hydrogen plasma treatments for passivation of amorphous-crystalline silicon-heterojunctions on surfaces promoting epitaxy". *Applied Physics Letters* 102 (2013).

[32] A. Descoeudres et al. ">21% Efficient Silicon Heterojunction Solar Cells on n- and p-Type Wafers Compared". *IEEE Journal of Photovoltaics* 3 (2013), pp. 83–89.

[33] Z.C. Holman et al. "Current Losses at the Front of Silicon Heterojunction Solar Cells". *IEEE Journal of Photovoltaics* 2 (2012), pp. 7–15.

[34] Y.K.E Yablonovitch, T. Gmitter, and RM. Swanson. "A 720 mV open circuit voltage SiOx-c-Si-SiOx double heterostructure solar cell". *Applied Physics Letters* 11 (1985).

[35] A. Richter et al. "n-Type Si solar cells wth passivating electron contact: Identifying sources for efficiency limitations by wafer thickness and resistivity variation". *Solar Energy Materials and Solar Cells* 173 (2017), pp. 96–105.

[36] F. Feldmann, C. Reichel, and R. Müller. "Poly-Si based passivating contacts". *Workshop on Passivating Contacts* (2018), pp. 1–26.

[37] S.W Glunz et al. "The irresistible charm of a simple current flow pattern - 25% with a solar cell featuring a full-area back contact". *31st European Photovoltaic Solar Energy Conference and Exhibition* (2015).

[38] F. Feldmann et al. "The application of poly-Si/SiO_x contacts as passivated top/rear contacts in Si solar cells". *Solar Energy Materials and Solar Cells* 159 (2017), pp. 265–271.

[39] Y. Tao et al. "Carrier Selective Tunnel Oxide Passivated Contact Enabling 21.4% Efficient Large-area N-type Silicon Solar Cells". *2016 IEEE 43rd Photovoltaic Specialists Conference (PVSC* (2016).

[40] F. Feldman et al. "A passivated rear contact for high-efficiency n-type silicon solar cells enabling high $V_{OC}s$ and $FF > 82\%$". *28th European PV Solar Energy Conference and Exhibition* (2013).

[41] J. Stuckelberger et al. "Passivating electron contact based on higly crystalline nanostructured silicon oxide layers for silicon solar cells". *Solar Energy Materials and Solar Cells* 158 (2016), pp. 2–10.

[42] M.K. Stodolny et al. "n-Type polysilicon passivating contact for industrial bifacial n-type solar cells". *Solar Energy Materials and Solar Cells* 158 (2016), pp. 24–28.

[43] C.K. Fink et al. "Silicon oxidation by ozone". *Journal of Physics: Condensed Matter* 21 (2009).

[44] F. Feldman et al. "Optical and electrical characterization of poly-Si/SiO_x contacts and their implications on solar cell design". *Energy Procedia* 124 (2017), pp. 31–37.

[45] S. Reiter et al. "Parasitic absorption in polycrystalline Si-layers for carrier-selective front junctions". *Energy Procedia* 92 (2016), pp. 199–204.

[46] R. Peibst et al. "Recombination Behavior and Contact Resistance of n+ and p+ Poly-Crystalline Si/Mono-Crystalline Si Junctions". *Solar Energy Materials and Solar Cells* 131 (2014), pp. 85–91.

[47] B. Nemeth et al. "Polycrystalline silicon passicated tunneling contacts for high efficiency solar cells". *Journal of Materials Research* 31 (2016), pp. 671–681.

[48] B.G. Lee et al. "Tunnel oxide passivated contacts formed by ion implantation for applications in silicon solar cells". *journal of Applied Physics* 118 (2015).

[49] Melskens et al. "Passivating contacts for crystalline silicon solar cells". *IEEE Journal of Photovoltaics* 8 (2018), pp. 373–378.

[50] A. Moldovan et al. "Tunnel Oxide Passivated Carrier-Selective Contacts based on ultra-thin SiO_2 Layers grown by Photo-Oxidation or Wet-Chemical Oxidation in ozonized Water". *2015 IEEE 42nd Photovoltaic Specialist Conference (PVSC)* (2015).

[51] Y. Tao et al. "Tunnel oxide passivated rear contact for large are n-type front junction solar cells providing excellent carrier selectivity". *3* (2016), pp. 180–189.

[52] Choi et al. "Structural evolution of tunneling oxide passivating contact upon thermal annealing". *Scientific Reports* (2017).

[53] P. Peibst et al. "Working principle of carrier selective poly-Si/c-Si junctions: Is tunnelling the whole story?" *Solar Energy Materials and Solar Cells* 158 (2016), pp. 60–67.

[54] M. Bivour et al. "Molybdenum and tungsten oxide: High work function wide bandgap contacts materials for hole selective contacts of silicon solar cells". *Solar Energy Materials and Solar Cells* 104 (2014).

[55] Bullock et al. "MOlybdenum oxide MoO_x: A versatile hole contact for silicon solar cells". *Applied Physics Letters* 105 (2014).

[56] Battaglia et al. "Silicon heterojunction solar cell with passivated hole selective MoO_x contact". *Applied Physics Letters* (2014).

[57] M.A. Green and A.W. Blakers. "Advantages of metal-insulator-semiconductor structures for silicon solar cells". *Solar Cells* 8 (1983), pp. 3–16.

[58] M. Boccard Z.C Holman. "Amorphous silicon carbide passivating layers for crystalline-silicon-based heterojunction solar cells". *Journal of Applied Physics* 118 (2015), pp. 240–247.

[59] G. Nogay et al. "Silicon-Rich Silicon Carbide hole-Selective Rear Contacts for Crystalline-Silicon-based Solar Cells". *Applied Materials & Interfaces* 8 (2016), pp. 35660–35667.

[60] G. Nogay et al. "Interplay of annealing temperature and doping in hole selective rear contacts based on silicon-rich silicon-carbide thin films". *Solar Energy Materials and Solar Cells* 173 (2017), pp. 18–24.

[61] Stefan Janz. "Amorphous Silicon Carbide for Photovoltaic Applications (PhD Thesis)". *Frauhnhofer Institute for Solar Energy Systems (ISE)* (2006).

[62] G. Nogay et al. "Crystalline Silicon Solar Cells With coannealed Electron- and Hole-Selective SiCx Passivating Contacts". *IEEE Journal of Photovoltaics* 8 (2018), pp. 1478–1485.

[63] B. Hallam et al. "The role of hydrogenation and gettering in enchancing the efficiency of next-generation Si solar cells: An industrial perspective". *Physica Status Solidi A* (2017).

[64] D. Deligiannis et al. "Wet-chemical Treatment for Improved Surface Passivation of Textured Silicon Heterojunction Solar Cells". *Energy Procedia* 55 (2014), pp. 197–202.

[65] G. Yang et al. "Design and application of ion-implanted polySI passivating contacts for interdigitated back contact c-Si solar cells". *Applied Physics Letters* 108.3 (2016), p. 033903.

[66] H. Kobayashi, K. Imamura, and W.B. Kim. "Nitric acid oxidation of Si (NAOS) method for low temperature fabrication of SiO2/Si and SiO2/SiC structures". *Applied Surface Science* (2010).

[67] G. Yang et al. "Poly-Si(O)x passivating contacts for high-efficiency c-Si IBC solar cells". *Energy Procedia* 124 (2017), pp. 392–399.

[68] R. Curley, T. McCormack, and M. Phipps. "Low-pressure CVD and Plasma-enchanced CVD" ().

[69] N. Sharma, M. Hooda, and S.K. Sharma. "Synthesis and Characterization of LPCVD Polysilicon and Silicon Nitride Thin Films for MEMS Applications". *Journal of Materials* 2014 (2014), pp. 1–8.

[70] J. Long et al. "Doped Microcrystalline Silicon Layers for Solar Cells by 13.56 MHz Plasma-enchanced Chemical Vapour Deposition". *Energy Procedia* 15 (2012), pp. 240–247.

[71] Y. Guangtao et al. "Poly-crystalline silicon-oxide films as carrier-selective passivating contacts for c-Si solar cells". *Applied Physics Letters* 112 (2018), p. 193904.

[72] A. Ingenito et al. "Phosphorous-Doped Silicon Carbide as Front-Side Full-Area Passivating Contact for Double-Side Contacted c-Si Solar cells". *IEEE Journal of Photovoltaics* (2018), pp. 1–9.

[73] M. Schnabel et al. "Hydrogen passivation of poly-Si/SiOx contacts fr Si solar cells using Al_2O_3 studied with deuterium". *Applied Physics Letters* 112 (2018), p. 203901.

[74] Renishaw PLC. *Raman spectroscopy in more detail*. URL: `https://www.renishaw.com/en/raman-spectroscopy-in-more-detail--25806`.

[75] E. Smith and G. Dent. "Modern Raman Spectroscopy A Practical Approach". *John Wiley & Sons Inc.* (2005).

[76] M. de Grunt. "IRFR Manual". *PVMD group (Technische Universiteit Delft)* (2013).

[77] D. Deligiannis. *Surface Passivation for Silicon Heterojuntion Solar Cells*. Technische Universiteit Delft, Nederland, 2017.

[78] PerkinElmer. *Lamda 650/850/950 - Hardware Guide*. 2004.

[79] PerkinElmer Inc. *Applications and use of integrating spheres with the LAMBDA 650 and 850 UV/Vis and LAMDA 950 UV/Vis/NIR Spectrophotometers*.

[80] Sinton Instruments. *WCT-120 - User Manual*. 2013.

[81] R.A. Sinton, A. Cuevas, and M. Stuckings. "Quasi-Steady-State Photoconductance, A New Method for Solar Cell Material and Device Characterization". *Conference Record of the Twenty Fifth IEEE Photovoltaic Specialists Conference* (1996).

[82] Sinton Instruments. *WTC-120- Offline Wafer Lefitime Measurement*. 2011.

[83] H. Fritzche. "Amorphous silicon and related materials". *World Scientific Publishing Co.Pte.Ltd.,Singapore* (1989).

[84] J. Bullot and M.P. Schmidt. "Physics of Amorphous Silicon-Carbon Alloys". *Physica Status Solidi(b)* 143 (1987), pp. 345–418.

[85] J. Wasyluk et al. "Raman investigation of different polytypes in SiC thin films grown by solid-gas phase epitaxy (111) and 6H-SiC substrates". *Materials Science Forum* 645-648 (2010), pp. 359–362.

[86] T.N. Truong et al. "Hydrogenation of Phosphorus-Doped Polycrystaline Silicon Films for Passivating Contact Solar Cells". *Applied Materials & Interfaces* 11 (2019), pp. 5554–5560.

[87] R. Gradmann et al. "Si and SiC nanocrystals in an amorphous SiC matrix: Formation and electrical properties". *Physica Status Solidi C* 3 (2011), pp. 831–834.

[88] H. Wieder, M. Cardona, and C.R Guarnieri. "Vibrational Spectrum of Hydrogenated Amorphous Si-C Films". *Physica Status Solidi (b)* 92 (1979), pp. 99–112.

[89] M. Künle et al. "Si-rich a-SiC:H thin films: Structural and optical transformations during thermal annealing". *Thin Solid Films* 519 (2010), pp. 151–157.

[90] D. Zhang et al. "Optical Enchancement of Silicon Heterojunction Solar Cells with Hydrogenated Amorphous Silicon Carbide Emitter". *IEEE Journal of Photovoltaics* 4 (2014), pp. 1326–1330.

[91] R.S. Bonilla et al. "Dielectric surface passivation for silicon solar cells: A review". *Physica Status Solidi A 214* 7 (2017), p. 1700293.

[92] L. Mazzarella et al. "Insights into Charge Carrier Transport Mechanisms of SiO_2/Poly-SiC_x/TCO Contact Structures for Si Solar Cells". *SiliconPV Conference* (2019).

[93] J.B. Heng et al. "> 23% High-Efficiency Tunel Oxide Junction Bifacial Solar Cell With Electroplated Cu Gridlines". *IEEE Journal of Photovoltaics* 5 (2015), pp. 82–86.

[94] F. Feldmann et al. "High and low work function materials for passivated contacts". *Energy Procedia* 77 (2015), pp. 263–270.

[95] P. Procel et al. "Numerical simulations of hole carrier selective contacts in p-type c-Si solar cells". *Solar Energy Materials and Solar Cells* 200 (2019), p. 109937.

[96] R. van der Vossen. "Optimization of passivating contacts for high-efficiency p-type silicon solar cells (MSc thesis)". *TU Delft* (2017).